University of Tennessee, Knoxville
TRACE: Tennessee Research and Creative Exchange

Doctoral Dissertations | Graduate School

8-2009

Laser Induced Hierarchical Coatings on Titanium Alloy

Anil Kumar Kurella
University of Tennessee - Knoxville

Follow this and additional works at: https://trace.tennessee.edu/utk_graddiss

 Part of the Engineering Commons

Recommended Citation

Kurella, Anil Kumar, "Laser Induced Hierarchical Coatings on Titanium Alloy. " PhD diss., University of Tennessee, 2009.
https://trace.tennessee.edu/utk_graddiss/60

This Dissertation is brought to you for free and open access by the Graduate School at TRACE: Tennessee Research and Creative Exchange. It has been accepted for inclusion in Doctoral Dissertations by an authorized administrator of TRACE: Tennessee Research and Creative Exchange. For more information, please contact trace@utk.edu.

To the Graduate Council:

I am submitting herewith a dissertation written by Anil Kumar Kurella entitled "Laser Induced Hierarchical Coatings on Titanium Alloy." I have examined the final electronic copy of this dissertation for form and content and recommend that it be accepted in partial fulfillment of the requirements for the degree of Doctor of Philosophy, with a major in Materials Science and Engineering.

Narendra B. Dahotre, Major Professor

We have read this dissertation and recommend its acceptance:

David C. Joy, Claudia J. Rawn, Hahn Choo

Accepted for the Council:

Carolyn R. Hodges

Vice Provost and Dean of the Graduate School

(Original signatures are on file with official student records.)

To the Graduate Council:

I am submitting herewith a dissertation written by Anil Kumar Kurella entitled "Laser Induced Hierarchical Coatings on Titanium Alloy" I have examined the final electronic copy of this dissertation for form and content and recommend that it be accepted in partial fulfillment of the requirements for the degree of Doctor of Philosophy, with a major in Materials Science and Engineering.

Narendra B. Dahotre, Major Professor

We have read this dissertation
and recommend its acceptance:

David C. Joy

Claudia J. Rawn

Hahn Choo

Accepted for the Council:

Carolyn R. Hodges, Vice Provost and
Dean of the Graduate School

(Original signatures are on file with official student records.)

Laser Induced Hierarchical Coatings on Titanium Alloy

A Dissertation

Presented for the

Doctor of Philosophy

Degree

The University of Tennessee, Knoxville

Anil Kumar Kurella

August 2009

Copyright © 2009 by Anil Kumar Kurella

All rights reserved.

Acknowledgements

I would like to take this opportunity to thank all of those people who have helped me in this research and in compiling this dissertation. First of all, I would like to thank my advisor Dr Narendra Dahotre for giving me an opportunity to explore the area of laser surface engineering. Apart from providing valuable technical inputs for the project Dr Dahotre was extremely helpful and patient when I had to make my personal and career choices. I would also like to thank my doctoral committee members Dr David Joy, Dr Hahn Choo and Dr Claudia Rawn for taking time to provide me inputs whenever approached in spite of their busy schedules. Special thanks to my lab mates and friends Sameer Paital, Anoop Samant, Abhijit Khangar, Anshul Singh, Subhadarshi Nayak, Sandip Harimkar, Greg Engleman for helping me with experimentation and fruitful technical discussions. I would also like to thank my parents for encouraging me to pursue higher education and my colleagues at Intel Corporation for their co-operation and help in completing my dissertation. Last but not the least I would like to thank my wife Sweta for her enormous patience and her excellent support in successful completion of my dissertation.

Abstract

Biomaterials research is an exciting and challenging area. It is exciting because of its potential applications and need for improving the quality of life. It is challenging because of the complexity with which natural biomaterials function in their environments. The gap that exists in terms of maturity and sophistication of the currently used synthetic materials from natural biomaterials is huge. It is only in the last few decades with the evolution of advanced material analytical techniques that researchers are starting to understand the complexity of nature. One such particular feature that has attracted our interest is the hierarchical nature of the bioimplant surfaces.

The present work is one small step in that direction where we tried to engineer a surface that is multi-scale in nature and biocompatible at these length scales. During a discovery phase a multi-scale textured zirconia coating was done on titanium alloy using a pulsed laser. Following proof of concept a bioactive calcium phosphate based coating was deposited on titanium alloy surface using a continuous wave laser. Based on detailed morphological and chemical analysis it was evident that the multi-phase coating had a multi-scale arrangement. Owing to the complexity of the coating a fractal based approach was used to interpret the morphology of the coatings. It appeared that at higher laser processing speeds star shaped calcium titanate features exist inside calcium phosphate and titania ring like structures. By tailoring a thermal model with current material system temperature calculations were made for various laser processing speeds. Using temperature predictions and knowledge of the phase constituents the series of self assembling steps that led to the formation of star and ring shaped arrangement are discussed. The biocompatibility of the coatings was evaluated by immersing in simulated body fluids. The

morphological and chemical evolution of hydroxyapatite precipitation along the calcium phosphate rich ring like structures coupled with the porous structure supports the possibility of enhanced osteointegration. The presence of calcium titanate ensured an interaction between the substrate and the precursor coating material. Wear measurements indicated that the laser processed samples possessed better mechanical properties than unprocessed surfaces.

Table of Contents

List of Tables

List of Figures

Chapter 1

Surface Engineering for Bioimplant Applications

This chapter discusses the role of surface engineering for bioimplant applications, the current trends in the research being done and need for surface engineering inspired by nature. Some content of this chapter had already been published in Journal of Biomaterials Applications (2005) by Anil Kurella and Narendra Dahotre under the title: Surface modification for bioimplants: the role of laser surface engineering [1]. My contribution to this paper includes but is not limited to selection of topic, literature survey, most of the writing, all of the figure drawings and compilation.

1.1 Introduction

It is rare to find a material that fits all the needs of a given application and biomaterials are no exception to this trend. For example a material considered for implant application may have excellent mechanical properties but poor corrosion resistance and hence may be incompatible with the biological environment and vice-versa. Therefore while performing material selection one has to strike a balance in arriving at an optimum solution. This balancing act is usually done between surface and bulk properties. Usually modifying the bulk severely contracts our options in materials selections and typically is not technologically or economically viable. Therefore among the choices available for enhancing the performance of a biomaterial the improvement of the surface phenomenon holds the key. As surfaces of materials are subjected to various external elements they are expected to provide corrosion resistance from environmental elements and at the same time provide wear resistance when in contact with other surfaces. On an average

500,000 hips and knee prosthesis operations are done per year in USA alone and quite a few of them are revision operations to replace or restore the original bioimplant material[2,3]. More significantly, as the population ages these revision operations are likely to go up. These are traumatic and costly. Loosening of the implants over a period of time happens due to poor adhesion, leakage of ions and corrosion in biological environment [3]. Therefore it is a constant endeavor of scientists and engineers to enhance the surface-related properties of biomaterials to enhance their longevity.

1.2 Review of Current Biomaterials

Gold was the first identified biomaterial. Over the ages it was used as an dental implant material. Over the last century quite a few materials have been identified for bioapplication. These can be classified generally into metallic, polymeric, ceramic and composite systems. Metallic biomaterials made from steel during early twentieth century turned out to be failures because of detrimental tissue reactions [4]. With the availability of 316 stainless steel post 1920 materials scientists found a material that was compatible with a biological environment [4]. Presently most of the artificial joints consist of a metallic component made from either alloys of titanium or CoCr. These are typically articulating against a polymer material like ultrahigh molecular weight polyethylene (UHMWPE). CrCo alloys have good wear resistance and due to the formation of stable chromium oxide, they are passive and corrosion resistant. They find application in metal-on metal bearing surfaces for hip joints [4]. Titanium and its alloys due to their low density and a low strength to weight ratio are ideal for load bearing applications [4]. As a result of passive TiO_2 that forms on the surface it provides a good solution for both orthopedic and dental applications [4,5]. Table 1.1 presents the mechanical properties of commonly used metallic

materials [2,6,7,8]. Ceramic biomaterials are typically oxides, carbides or inorganic silicates. Ceramics usually have good refractory properties and high compressive strength. There are multiple classes of bioceramics: bioinert, bioactive and biodegradable materials [2]. Ceramics like alumina and zirconia maintain their mechanical, chemical, and physical properties even in biological environments and are termed bioinert. Owing to its high wear resistant and toughness under stress, zirconia ceramics find application in the total hip replacement (THR) ball heads [9,10,11,12]. Ceramics that degrade upon implantation in bio-environments are considered as bioresorable-bioactives. Examples of this kind are calcium phosphates. Another material, hydroxyapatite (HA) can be crystallized from calcium phosphate and falls in this category. In fact, human bones and teeth are comprise of hydroxyapatite mineral [13].The problem with HA is its poor fracture toughness (K_{IC}.) Its K_{IC} is around 1.2 MPa $m^{1/2}$. The human bone has a fracture toughness ranging from 2 to 12 MPa $m^{1/2}$. Hence, for load bearing applications direct usage of HA is not applicable. Calcium phosphate materials (commonly referred as Ca-P) are interesting for coating applications.

Table 1.1 Mechanical properties of three main metallic systems [1].

Mechanical Property	**Cold worked 316L SS**	**Ti6Al4V**	**CoCrMo (F75)**
Specific Gravity (g/cc)	7.9	4.5	8.3
Tensile Strength (MPa)	860	860	655
Yield Strength (MPa)	690	795	450
Elongation (%)	12	10	8
Reduction of Area (%)	50	25	8

Table 1.2 presents the key mechanical properties of the commonly known bioceramics materials [2,8,13]. Recent advances in materials processing have resulted in materials that are bioactive in nature. They induce biological bonding between the biomaterial and the tissue in due course of time when placed in physiological liquid. Bioglass® and Cervital® are examples of these classes of materials available commercially for coatings of metal prostheses [2,14]. The final class of biomaterials is the polymers. These materials are easy to manufacture and are low cost. Polymers are the long-chain molecules that consist of multiple small repeating units. Polymers are currently used in dental, orthopedic, cardiovascular, and soft tissue applications. Specifically, ultra high molecular weight polyethylene (UHMWPE) is used in the acetabular cup of hip replacements and the patellar surfaces and tibia plateau of knee joints. The major issue thought with polymeric materials when compared to ceramic or metallic systems is their poor wear resistance and lower mechanical strength. A general classification of biomaterials is presented in Table 1.3.

Table 1.2 Mechanical properties of commonly used ceramic materials [1].

Property	**Alumina**	**Hydroxyapatite**	**PZT**
Density (g/cm^3)	> 3.93	3.156	6.1
Hardness (VHN)	2300	500-800	1300
Fracture Toughness (MPa $m^{1/2}$)	5-6	~ 1.0	9.0
Compressive Strength (MPa)	4500	100-900	2000
Young Modulus (GPa)	380	70-120	290

Table 1.3 Broad classifications of commonly used implant biomaterials [1].

Biomaterial Type	**Examples**	**Major Application**	**Features and Issues**
Metallic	Steel- 316	Structural	Bioinert but high strength to weight ratio compared to Titanium
	CoCr alloys: Co-Cr-Mo, Co- Cr-W-Ni, Co-Ni-Cr-Mo-Ti	Structural	Bioinert, good wear resistance but lower fatigue performance.
	Ti alloys:CP Titanium, Ti-6Al-4V,Ti-3Al-2.5V, Ti- 6Al-7Nb	Structural	Bioinert, low strength-to-weight compared to other metallic systems but lower wear resistance compared to CoCr alloys.
Ceramics	Alumina, Zirconia	Structural & Coatings	Bioinert and lower fatigue resistance compared to metallic systems
	Hydroxyapatite, Calcium phosphate	Coatings	Bioresorable and lower fracture toughness compared to metallic systems
	Bioactive: Bioglass®, Cervital®	Structural and coatings	Bioactive and lower fracture toughness compared to metallic systems
Polymers	Polyethylene, Silicone UHMWPE, PVC	Structural	Bioinet, easy to manufacture, Low cost but lower wear resistance compared to other metallic and ceramic systems.

1.3 Tissue-Bioimplant Interface

The nature of interaction between bioimplant surface and the surrounding tissue is dynamic. During the initial seconds of implantation water and free biomolecules along with dissolved ions surround the implant surface. The healing process starts with modification of the composition of biofluid surrounding the implant along with adsorption of a layer of biomolecules as depicted in Figure 1.1. After this stage, the cells gradually reach the surface and the adsorbed layer dictates the way the cells respond. As time progresses, the nature of the cells and their activities on the surface change leading to a tissue integration or fibrous encapsulation [2,15]. The term 'Osteointegration' represents direct contact between bone and implant without the intervention of soft tissue. For effective osteointegration the surface chemistry and microtexture play a significant role [2]. The physical texture at atomic, molecular, and higher scales act as points of contact for biological entities like proteins, cells, and tissues, respectively [16,17]. Each of these focal points influences the biological interactions at that scale resulting in a hierarchical integration. All these morphological integrations are being done when the chemical activity of the implant elicits specific response from biomolecules at each scale. In essence, at each length scale there are specific biological responses that need to happen during osteointegration-a facet of the complex natural arrangement found in natural systems [2,17,18].

1.4 Surface Engineering

Having briefly explored the complexity associated with the interfaces and natural biomaterials it is interesting to explore the current status of surface modification techniques used to engineer biomaterials.

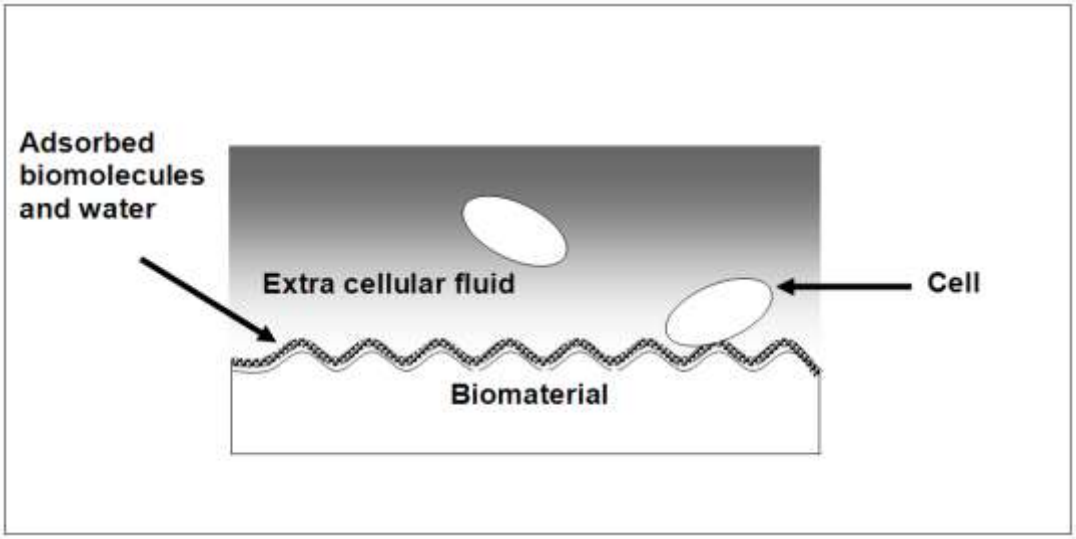

Figure 1.1 Interaction near an implant surface [1].

For biomaterials there are multiple objectives for surface engineering: to improve tribological, mechanical, and chemical properties or influence the biocompatibility and functionality of the implants. All these are to be achieved while retaining the key bulk properties of the material. Usually this is done by either coating the existing surface with a different material or changing the atoms, compounds, or molecules on the existing surface chemically or physically. The following sections present some of the commonly adapted surface engineering strategies with clear emphasis on coating and texturing operations. They are broadly classified as texturing and coating operations. In each category, the key surface engineering techniques are covered by briefly discussing their pros and cons.

1.4.1 Physical Texturing

Multiple techniques have been explored to texture the surface of biomaterials because the physical structure determines the cellular responses and hence the range of biomaterial

applications. Integration occurs at multiple length scales from nanoscale to macroscale [17]. At nanoscale, the cell signaling with protein molecule interactions occur contributing and enabling the cell adhesion, proliferation and differentiation. The self-organization of protein molecules and cell attachment is driven by the combined effects of configurational hydrophobic/hydrophilic or capillary forces. At a higher length scale, specifically in the micron range, the cell alignment takes priority. Eventually, at macroscale the interaction of the tissue with the porosity completes the integration. Based on these findings researchers are currently engineering surfaces with micrometer and nanometer scale features to enhance osteointegration. However, the ideal surface incorporating micro and nanoscale features with bioactivity at all lengths is not currently realized.

From the osteoconduction perspective there are two features that are important: Contact guidance and cell signaling. The term ‘contact guidance’ refers to the phenomena by which cells adapt, orient, and attach along the substrate topography [19,20]. Cell signaling on the other hand refers to the way cell surface receptors respond to the chemical nature of the surface. Following the establishment of this cell signaling with the surface, cells try to achieve biomechanical equilibrium with the topography via contact guidance orientation [20]. Various topographical features like ridges, grooves, cliffs, dots, and spikes were evaluated for contact guidance [21,22,23]. Although the studies involved using different cell systems like fibroblasts, epithelial cells, neurons, and neutrophils it was clear that fine features less than 10μm have significant orientation effects on both cytoskeleton elements and cell body. Karacs et al., have conducted in vivo testing on rabbits with Ti alloy surfaces [24]. From their torque removal force studies they observed higher forces for implant surfaces that were either sand blasted or laser treated compared to smoothly machined surfaces. The in-growth of the bone into the microscale features

created by processes like sand blasting and laser processing created micromechanical retention and hence higher torque removal forces were needed [24]. They also commented that purity of the surfaces is also beneficial for better osteointegration [24].

In general, there is existing literature showing random surface topographies influencing osteointegration, however, the exact nature of the interaction at micron scale is always confounded [25,26]. As a result, multiple patterning methodologies have tried to come up with ideal performance, however, the level of understanding about the interaction is still nascent. The prominent techniques for surface modification are laser processing, photolithography, electron beam processing, ion beam processing, etc. [21,27,28]. Ion beam and electron beam processes typically need vacuum chambers and best for silicon and are polymeric materials and have not been optimized for Ti based alloys and these processes are costly. Photolithography based processes are typically multi-stage and best for polymeric materials. Comparatively, laser processing is easily adaptable for various materials with high degree of precision and can be done under non vacuum conditions [29].

1.4.2 Chemical Modifications

The surfaces of the biomaterials are chemically modified for enhanced osteointegration by various techniques. Some of the techniques include acid etching, ion beam implantation, silanization and Langmuir-Blodgett deposition, self assembled monolayer deposition, micro contact printing, and finally coatings [5, 30]. Each of these processes has their own advantages and disadvantages. Specifically for hard tissue and load bearing applications chemical coatings are perceived as likely solutions owing to their ability to form a bond with the substrate underneath and provide the wear and retention properties needed to effectively integrate. Various

coating techniques like sol-gel, plasma spray, thermal spray, and electropheretic process have been tried [31,32,33]. Calcium phosphate based coatings are attractive given their ability to boost biocompatibility and improved osteointegration due to the presence of chemical species like Ca and P ions [30].

The major concern with most of these techniques is the chemical inhomgenity due to multiple phase formation, lack of crystallinity in the coatings, and absence of good bonding between the substrate and coating [34,35]. In this area, experiments conducted with high energy density lasers are starting to show some promise. Hydroxyapatite coatings obtained by using KrF and ArF lasers have shown good crystallinity and adhesion properties [36,37,38]. The following section briefly reviews the status of laser surface engineering for biomaterial applications.

1.5 Review of Laser Surface Engineering for Biomaterials

LASER stands for Light Amplification by Stimulated Emission of Radiation (LASER). In the field of materials processing lasers find a wide range of applications from cutting and drilling operations of bulky heavy industry steel structures to the delicate surface fabrication of electronic materials [39,40]. The field of laser surface engineering utilizes the power from a laser source focused on a localized area to melt, heat, or modify the material properties near the surface [39]. Some of the common examples of laser surface engineering involve alloying and mixing of materials, texturing, grain refinement, and microstructure modifications- all these without greatly changing the bulk material properties. The short duration and highly localized energy input from the laser creates steep thermal gradients between the hot spot and the relatively cold substrate underneath. Such steep thermal gradients coupled with conduction of

heat transfer results in cooling rates as high as 10^{11} K/s. Typically such a high cooling rate results in metastable microstructural features [41,42,43].

By modulating the laser parameters like power, pulse duration, and spot size it is possible to tailor the needs of surfaces. Excimer lasers like KrF (248 nm) and ArF (193 nm) are being used to produce submicron features on polymeric surfaces [44].Patterning of nanoscale features can be carried out typically by using Vacuum and Extreme Ultraviolet laser sources [44]. Laser surface nanopatterning involves a simple setup; high speed and easy processing compared to electron beam or focused ion beam techniques. Based on these factors research in the field of Laser Surface Engineering (LSE) of biomaterials is progressing rapidly. One such area is the laser-assisted coatings on bioimplant surfaces. During laser processing, the interest is to induce the formation of chemical species and structural features, which enhance the interactions between the surface and its biological medium. Usually materials like HA or other bioglasses are ablated and then deposited on substrates like Ti alloys in a controlled fashion [30,45]. The ability to choose the kind of laser based on the absorptivity of the material along with the capability to control the thermal gradients by modulating the power, pulses, distances from substrate make lasers ideal for experimenting. Another objective could be to micromachine the texture of surfaces to create three dimensional features that improve osteointegration. Lasers provide flexibility of use when the substrate material is difficult to remove or when the surface geometry is complex to machine. For example microtexturing of grooves on wide variety of materials was achieved via laser processing with relative ease [39,46,47]. Moreover, laser texturing in addition to being a fast process is typically clean and does not require organic solvents or any photorestist developments unlike photolithography. To engineer micron and submicron features, there is no need to resort to clean rooms, spin coaters, and photoresists [29].

From a manufacturing perspective this is a great asset because purity of biomedical implants is the critical factor and contamination with any kind of non biocompatible material during the surface processing would result in detrimental reactions when implanted. In addition, the common drawback of conventional techniques like chemical etching, anodizing, and mechanical scratching is that they lack good control and provide limited opportunity for localized texturing [39]. Lasers by their inherent ability to modulate pulsing and power characteristics provide scientists with multiple choices of creating unique texturing capabilities by ablating predictable amounts of material. This ability to create textured surfaces with specific length scale features in a non-contact fashion is being experimented for bioimplant applications and will be discussed in detail in the following section.

1.5.1 Laser Assisted Coatings

Based on their wavelengths there exist multiple classes of lasers: CO_2, YAG, excimer, dye, argon-ion, diode, etc. The wavelength at which they operate and the energies they impart to materials gives way for their unique applications [39]. The critical factors that influence the nature of interaction are the wavelength of the laser, energy, and frequency along with properties of material under consideration like its optical reflectivity, melting point, and thermal diffusivity [39]. Specifically, focusing on hard tissue replacement applications Zeng et al. have reported that controlling the pressure and composition of the ambient gas a laser coating was deposited with Ca/P ratios close to initial HA target [48]. Using a pulsed laser setup that typically contains a substrate, target, and laser source they have reported that the presence of water vapor in the chamber enhanced the crystallinity of the coating. Each laser pulse ablates some amount of target material that is then condensed on to the substrate. Cleries et al., have reported pulsed laser

deposition of HA using both Nd:YAG and excimer lasers [49,50]. Fernandez-Pradas et al., have reported the coating obtained via Nd: YAG laser and excimer laser are granular in nature [50]. They have observed that Nd:YAG laser processing resulted in granular morphology while excimer lasers resulted in columnar. Lusquinos et al., have tried to laser process a hydroxyapatite (HA) powder spray jet over a Ti alloy surface [51] by melting the hydroxyapatite powder particles in air and condensing them on to the Ti alloy substrate. However, not much was explored on the morphological evolution of these coatings.

1.5.2 Laser Assisted Texturing

Depending on the type of material to be processed and the nature of feature to be fabricated there are various options using lasers. This present section discusses these options based on the type of laser. CO_2 lasers typically used for processing metallic and ceramic materials are operated in the 1.5 – 3 kW power range with maximum beam intensities reaching 10 MW/cm^2. Such high energies are ideal for cutting and welding purposes. However, by changing the optics it is possible to focus a beam spot of 100 µm and texture surfaces using pulsing operation with frequencies of 25-45 kHz [39]. Hao et al. have tried to change the roughness and surface energy of zirocnia bioceramics by using a CO_2 laser [52]. At various laser powers they measured oxygen content, roughness, and contact angle of liquids on the final laser processed surfaces. They attribute wettability was influenced more by the microstructural changes on the surface along with the oxygen content and had less dependence on roughness. At low laser powers there was reorientation of the crystal structure which changed to a hexagonal arrangement and cellular structures as laser power increased. Greater fibroblast cell attachment was observed on samples processed at higher laser powers [52].

Nd:YAG lasers are used for a wide range of texturing operations and can be operated in both pulsed and continuous wave modes. Nd:YAG lasers are used in texturing hard disk surfaces has been well documented [39]. A predetermined pattern can be accurately produced by controlling the pulse repetition rate of the Nd:YAG laser. Compared to CO_2, laser Nd:YAG lasers operate at lower wavelengths resulting in much smaller spot size and features that can be fabricated. With the ever increasing need for high precision cutting and complexity of marking features on medical components Nd: YAG lasers are finding great usage. For both CO_2 and Nd:YAG lasers the nature of processing is usually thermally driven: by directing an energy beam onto a focused spot the area is melted by increasing temperature. As this continues the rising temperature eventually can lead to vaporization of the material. As the laser spot moves the temperatures drops and the molten material re-solidifies. Thus during typical laser processing the various sequence of events like melting, melt motion, evaporation, and solidification that take place resulting in a new surface topography. Melt ejection and evaporation are the two competing processes that determine the extent of material removal and final crater formation. Nd:YAG laser pulsed ablation was successfully reported on various metallic systems materials like aluminum, copper, titanium and molybdenum [53,54]. Specifically looking into Ti alloys György et al. have studied the role of Nd:YAG (λ = 1064 nm) laser on resulting surface morphologies [55]. Based on their morphological analysis via scanning electron microscopic and profilometric measurements they interpreted that at around 1×10^8 W/cm^2 intensity melting of the surface layer takes place without vaporization and displacements of the liquid occurs along the edges. For higher laser intensities the roughness increases owing to the increased liquid displacements due to air break down and increased vaporized plasma recoil pressure. Hallgren et al. have reported an interesting method to texture Ti implants. Screw shaped implants were

patterned using a frequency double Nd:YAG laser operating at 523nm and splitting it through a kinoform. In vivo testing of these textured implant surfaces showed higher torque removal forces compared to non textured surface [56].

Excimer Laser, operating in the sub 400nm range are useful in micromachining non metallic systems like polymers. The thermal effects associated with Nd:YAG lasers in the infrared range render them less effective on polymeric systems. Because of their low thermal effects the excimer lasers operating in the ultraviolet range can help fabricate submicron features by breaking the molecular bonds of the polymeric material at the surface [57]. Complex three dimensional features can be fabricated when excimer lasers are coupled with mask projection techniques [58,59]. With energy intensities around 10^8- 10^9 W/cm^2 excimer lasers enable texturing of complex geometries. By combing excimer lithography with microlithography Duncan et al. have photoablated polymeric surfaces [29]. Cell culture studies using oestroprogenitor cells on these microgrooved surfaces showed promising results after 7 days of incubation.

1.6 Inspiration from Natural Biomaterials

Having explored the nature of interaction in natural biological systems it appears that the current surface engineered solutions for bioimplant applications are far from matching their complexity. Natural biological systems are bioactive and at the same time hierarchically evolved across multiple length scales. This complexity, although challenging to realize, formed the basis for the research presented in this dissertation. Engineering such complex surfaces is only part of the challenge because there is no standard methodology to compare such multi-scaled surfaces. This is where we drew inspiration from nature and explored the applicability of fractals for

characterization of surfaces that are hierarchically integrated. Typically monitored surface parameters like average roughness, R_a, or the root mean square average, R_q (rms), do not convey information on the range of length scales over which different topographic features exist. They lack the spatial correlation and are length scale dependent [60,61]. Fractals are interesting because of their extreme fragmentation based on non-euclidean geometry instead of regular topological dimensions. Fractals are typically quantified by fractal dimension, F_d, which help in distinguishing fractals at any scale. In general fractal can be classified into natural and ideal fractals [60].

Natural systems like coastal lines, mountain ranges, roots of trees, neurons, bronchi in lungs etc are characterized by a growing structuring element based on a random mode of construction. On the other hand, mathematically generated fractals are ideal fractals. For example consider Von Koch snowflakes, the fractal dimension when calculate for this is unique at any particular length scale [60,61]. Typically, calculation of fractal dimensions for surfaces is a complicated process since it involves not only adopting mathematical models but also handling surface topography image processing [61]. These are dealt with detail in the experimental section of this dissertation. Characterizing the engineered multi-scaled surfaces by using fractal dimensions helps correlate the ability of these surfaces to undergo effective osteointegration. The present work is inspired from nature and attempts to mimic nature by creating biomaterial surfaces that are hierarchical and fractal at the same time.

Chapter 2

Scope and Objectives

Natural biomaterials are complex hierarchically evolved structures that have interactions with their environments at different length scales. Current processing technologies do not have that level of sophistication both in physical structure and resulting chemistry. The ideal synthetic biomaterial is expected to integrate with its bio-environments and is envisioned to be multi-scale and biologically active at the same time. The aim of the present work is to introduce such complexity both from physical structure and chemical perspective into the coatings. This would create a surface that would mimic natural biomaterials and therefore enhance the biocompatibility. This is envisioned via an integrated coating and texturing laser processing operation. This novel surface engineering approach would result in a multi-scale textured surface mimicking natural biomaterials. The experimental work discusses a precursor deposition followed by laser processing to create a multi-scale textured biocompatible coating. To our knowledge prior to this work, there is no published literature reporting such a kind of laser processing resulting in simultaneously textured coating on titanium alloys. Most of the earlier researchers have tried to ablate calcium phosphate based materials from a target and deposit on polymeric or Ti alloy surfaces. Not much of the prior emphasis was given to create a multi-scale morphology [36, 37]. The laser surface engineering methodology proposed here involves precoating followed by laser surface engineering. Figure 2.1 schematically represents the concept of simultaneous texturing and coating for enhanced bioapplication. As a result of this processing, there will be melting of precursor and substrate followed by re-solidification of these materials.

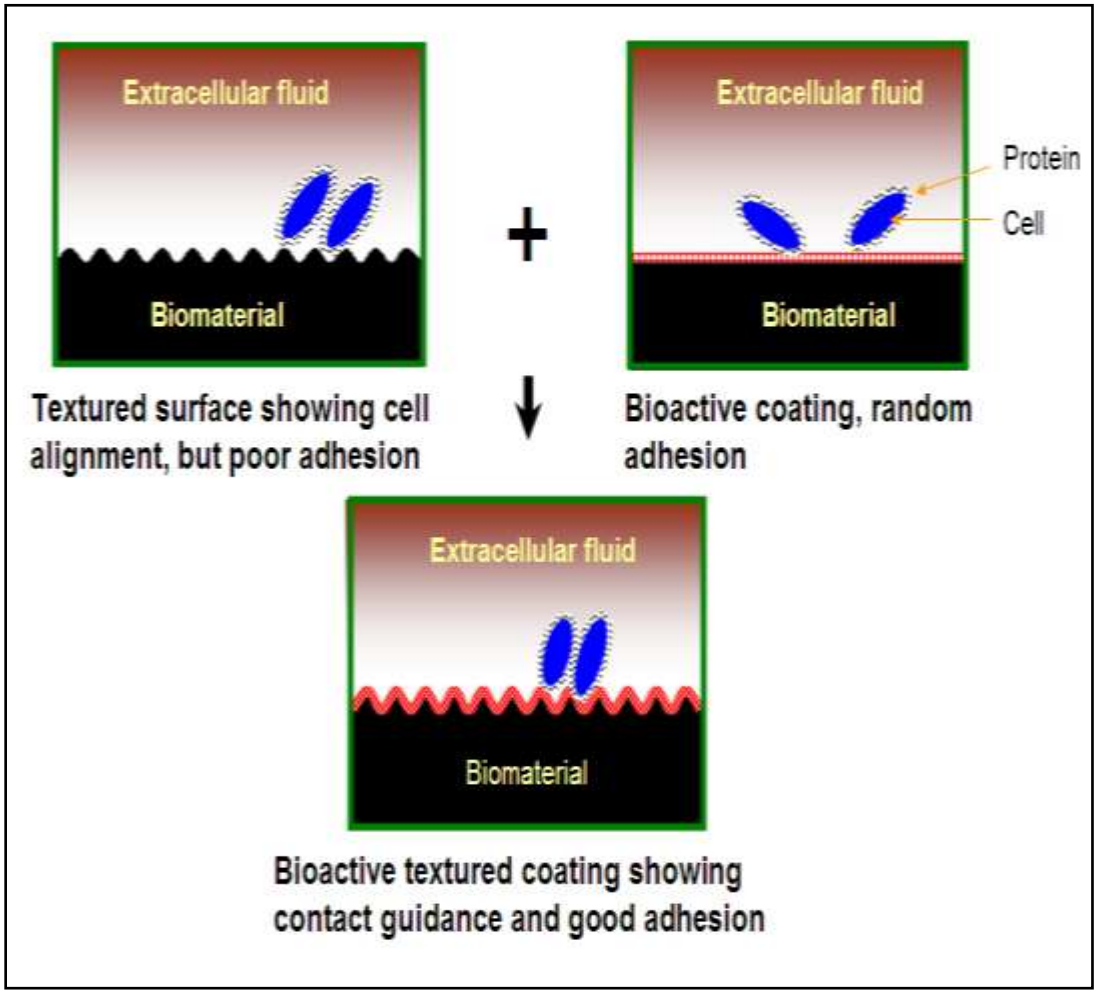

Figure 2.1 Schematic showing the concept of integrated textured coating and its benefit for biocompatibility.

It is also expected that there will be chemical interaction of the substrate with the precoating material introducing a texturing element, a feature that was not explored by earlier researchers. While texturing provides contact guidance, coating would provide the protein signaling and cell adhesion. An integrated coating that is textured will provide both the benefits. As the experiments and process adopted were one of its kind and there was no published data we chose to experiment with zirconia prior to calcium phosphate as precursor for evaluating the feasibility of this simultaneous coating and texturing methodology. There are multiple reasons for experimenting with zirconia during this discovery phase and the details are to be presented in the experimental section. Following the successful retention of zirconia the coating and evidence of multi-scaled features in the final morphology focus was then is shifted to Ca-P (Calcium phosphate) based coatings obtained from Calcium Phosphate Tribasic (CPT) as the precursor material on the Ti alloy substrates. As calcium phosphate compounds are bioactive and far more significant for bioimplant applications they represent the crux of the experimental work. The results and discussions will be centered around Ca-P rich coatings on Ti alloy substrates. Characterizations of these coatings will be done from chemical and morphological perspectives. Based on laser processing parameters used, thermodynamic and phase transformation principles, the formation of multiphase multi-structural coating will be explained. As discussed earlier since natural systems are fractal in nature the multi-scale features resulting from laser processing will be subjected to image processing and fractal analysis. Surfaces that have consistent fractal dimension over multiple length scales are closer to natural systems and thus stand a better chance for enhanced biocompatibility. To evaluate this, Ca-P rich coatings on Ti alloy substrates were immersed in simulated body fluid and monitoring of biomimetic growth of hydroxyapatite was carried out.

Chapter 3

Experimental Work

3.1 Introduction

This chapter discusses the experimental methodologies adopted in generating laser assisted textured coating. Some content in this chapter has already been published in Journal of Minerals, Metals and Materials Society in 2005 [62], Journal of Materials Science: Materials in Medicine in 2006 [63], Actabiomaterialia in 2006 [64], Material Science and Engineering C in 2008 [65], Journal of Applied Physics in 2009 [66] with Anil Kurella being the primary author. The references listed above provide complete information about the publications. The primary author's contribution to these papers includes but is not limited to selection of topic, literature survey, experimentation, analysis, technical writing, all of the figure drawings and compilation.

3.2 Material Selection and Sample Preparation

Synthetic materials expected to integrate into biological environments should have excellent biocompatibility. In addition, if used in load bearing applications they should have mechanical integrity with adequate strength and wear resistance properties. Often it is difficult to find a material that meets all the above requirements. Hence in the current work the materials selection is based on integrating a substrate material having good mechanical properties with a coating material capable of exhibiting superior biocompatibility. The Ti alloy Ti-6Al-4V was chosen as a substrate material. Titanium and its alloys offer excellent corrosion resistance in biological environments because of a passive TiO_2 layer formation on the surface and have excellent

strength to weight ratios. However they have poor wear resistance, Therefore they are typically coated with bioceramics. In the present study two different precursor coating materials were used: Zirconia was used for discovery phase study as the coating material. The success of the discovery phase paved way for applying of this Calcium phosphate Tribasic (CPT) as the precursor on the Ti alloy for subsequent laser processing. Although zirconia is not bioactive it is an excellent bioinert ceramic [67]. Moreover zirconia is fairly stable with high melting (2700^0C) and boiling points (4500^oC). Thus there is a greater chance of retention of the coating post laser processing. Also there was interest to see if by using pulsed laser significant melting of Ti substrate underneath could be induced (to dictate a morphological evolution during solidification) while at the same time ensuring limited loss of zirconia on the surface. Results from the zirconia provided learning's that were carried forward to CaP processing. These details will be provided at the end of the Results and Discussion section from zirconia coatings in Chapter 4.

Zirconia (ZrO_2) (stabilized with 5.4 wt% Y_2O_3) the starting powders were obtained from Goodfellow Cambridge Limited, England. The mean particle size of zirconia powder used in this process was less than 1μm. Calcium Phosphate Tribasic $Ca_5(OH)(PO_4)_3$ obtained from Fisher Scientific. The Ca:P molar ratio of 1.68 corresponds to the stoichiometric composition of the Hydroxyapatite (HA). Post material selection, the chosen materials were then prepared for processing and materials analysis as discussed in the following paragraphs. The first step in sample preparation was to cut the Ti alloy (Ti-6Al-4V) plates into small coupons using Techcut10 ™ Allied High Tech Products Inc. These coupons were then ground and polished to achieve a roughness of 0.5μm. They were then rinsed in water and cleaned with acetone. The precursor coating material, either Zirconia or Calcium Phosphate Tribasic (CPT), was mixed

with a proprietary water based organic solvent (LISI WI5853, Warren Paint and Color Company, Nashville,TN, USA). Using an electrically operated stirrer the precursor particles were mixed with this organic solvent. This liquid was then sprayed onto preheated Ti alloy coupons (50^{o}C) using a spray gun. The pre-coated coupons were then dried at 100^{o}C for few minutes. The dried coupons were now ready for laser processing. The thickness of the pre-coat was typically around 40μm as measured by the difference between the micrometer readings on the optical microscope focused on the surface of sprayed pre-coating and the substrate surface at the bottom of a scratch in the sprayed pre-coating.

3.3 Laser Processing

Laser processing of the precoated coupons was done schematically illustrated in Figure 3.1. If the output from a laser is continuous with constant-amplitude it is called continuous wave (CW) laser operation. On the other hand, if the output of the laser varies with time taking the form of alternating on/off cycles it is called pulsed laser operation. Typically, higher peak powers are achieved in pulsed laser operation.

3.3.1 Pulsed Laser Processing

Ti-6Al-4V alloy coupons 25mm x 25mm x 3 mm in size precoated with Zirconia were laser processed using a pulsed Nd:YAG laser (Trumpf Laser and VectorMark workstation). This laser emits infrared radiation of wavelength 1064 nm. With a focus diameter of 40 μm on the sample surface it is capable of delivering a fundamental-mode beam quality with pulse frequencies ranging from 1-60 kHz. The samples were processed with 25W power at frequency of 10 kHz for three different traverse speeds: 40 cm/min, 160 cm/min, and 290 cm/min.

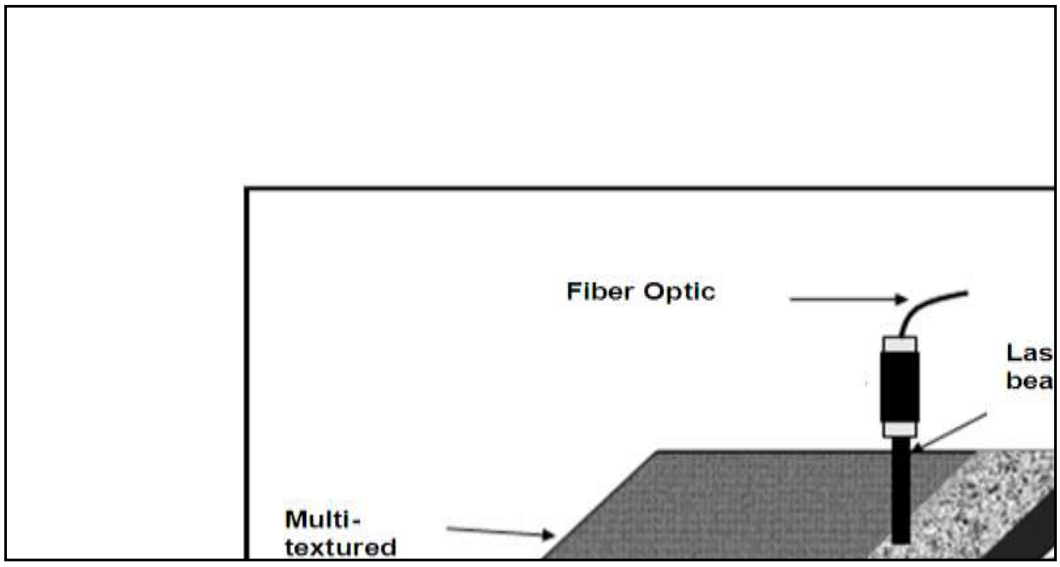

Figure 3.1 Schematic of laser surface engineering process [1].

Gyrorgy et al., have commented that intensities of 10^8 W/cm^2 are needed for induce appreciable melting on Ti surfaces [55]. Therefore in the present work intensities in the range of 10^6 W/cm^2 are chosen because of the multi-pulse nature of the experiment.

3.3.2 Continuous Wave Laser Processing

Successful coating deposition of Zirconia on Ti-6Al-4V was achieved via pulsed laser processing. Similar efforts with the CPT precursor had limited success owing to rapid vaporization of material under pulsed laser exposure. In pulsed laser operation the pulsing action results in higher energy dissipation in a concentrated area in shorter time frame resulting in possibility of higher vaporization compared to continuous wave laser. Zirconia (MP = 2700^{o}C, BP = 4500^{o}C) vaporizes at higher temperatures compared to CPT (MP = 1570^{o}C, BP = 3227^{o}C) and thus was retained significantly post pulsed laser processing. Therefore a continuous wave laser operation was used. This is a 4KW HASS Laser with 600µm diameter 15m fiber optic

coupled with an output coupler for beam shaping. Ti-6Al-4V coupons (50 mm x 100 mm x 3 mm) were precoated with CPT and processed under 1064 nm Nd:YAG laser in continuous wave mode.

3.3.2.1 Experiment A

The laser scanning was conducted using a rectangular beam (5.0 mm × 1.5 mm) with uniform intensity at speeds varying from 100 cm/min to 225 cm/min at 850W power. This experiment is referred to Experiment A. The entire surface of the coating was processed by multiple tracks with 15% overlap between subsequent passes. Considering this overlap, roughly 11 tracks were required to coat the entire width of the coating of 50 mm. For a laser moving at 125 cm/min and operating at a power of 850W the energy imparted to a beam area (5.0mm x 1.5mm) is approximately 200J as per the equation shown below. Detailed temperature model calculations were actually done for comprehending the chemical and morphological evolutions and are presented at later stage. The calculation presented here was used for identifying the processing conditions prior to experimentation. The laser intensities chosen were in the range of 10^4 W/cm^2. This is two orders of magnitude lesser than the intensities used for zirconia processing. This is due to the realization that in spite of the retention of zirconia at various speeds there was appreciable evaporative loss of zirconia. Therefore to limit the evaporative loss of CPT from the precoating lower power intensities from a continuous wave processing were chosen.

$$Q_L = \frac{Power X dis\tan ce}{Speed} \qquad (3.1)$$

Taking the absorptivity of 0.1 for calcium phosphate in this infrared range the net energy transferred into this area is approximately 20J. Theoretically the thermal energy needed in this

area to raise the temperature of precursor alone to melting point and melt is approximately 2J. This is calculated by using the following equation.

$$Q_t = mC_p(dT) + mL \quad (3.2)$$

In the above equation Q_t refers to the total thermal energy needed, m is the mass of the area of the precursor under the beam, C_p is the thermal heat capacity (1000 J/Kg.K), dT is the temperature rise (1500K), and L is the latent heat of melting (15kJ/mol) [68] . The order of magnitude difference could be incorporate into the dissipative losses during thermal conduction into substrate Ti alloy and for laser parameters modulation from 100 cm/min to 225 cm/min.

3.3.2.2 Experiment B

Experiment A was repeated a second time with speeds ranging from 100 cm/min to 225 cm/min and is referred to as Experiment B. Additional speeds corresponding to 250 cm/min and 275cm/min were also conducted. The laser beam at the focus was elliptical in cross section, being 5 mm x 1.5 mm in size. The processing was conducted by operating the laser beam in continuous mode such that with the given processing speed and beam size, it provided the beam residence (interaction) time of 45 ms at any given location on the sample.

3.4 Chemical Analysis

Analysis of the coating surfaces is critical to understanding the extent of interaction that resulted from laser processing of the precursor materials on the substrate. Methodology adopted for elemental and phase analysis of the chemical constituents in the coating is to be presented in the following sections.

3.4.1 Multi-phase Characterization

Philips Norelco X-ray diffractometer was used for structural and phase analysis. The final coatings along with starting precursor powders were characterized with Cu Kα radiation operated at 30 kV and 20 mA. The diffraction range of X-ray scans were typically from 20^0 to 100^0 with a step increment of 0.02^0 and a stepping time of 1 second. Elemental chemical analysis of specific microstructural features was carried out using the Energy Dispersive X-Ray analysis setup attached to Leo 1525 scanning electron microscope (SEM).

3.5 Morphological Analysis

Chemical analysis alone does not provide a complete picture about the nature of interaction happening between the precursor and substrate. Morphological analysis provides valuable information about the role of laser processing. In addition morphological analysis also provides insights into the multi-scale nature of coating surface from a biocompatibility perspective. The following paragraphs present the morphological analysis captured from scanning electron microscopic imaging and profilometric scanning followed by fractal analysis.

3.5.1 Multi-scale Evolved Surfaces (Scanning Electron Microscopy)

A detailed surface morphological analysis of the laser processed samples was carried out using a Scanning Electron Microscope (SEM). Two different microscopes Leo 1525 and Hitachi S 3500 were used at different stages. The Leo1525 microscope was equipped with an Energy Dispersive X-Ray Spectrometer for elemental microanalysis. The microscope had a standard secondary

electron detector for topographic imaging. The microscope ran at accelerating voltages from 0.5kV to 20kV. The Hitachi S 3500 ran at accelerating voltages ranging from 0.3 to 30kV.

3.5.2 Surface Characterization via Stylus Profilometry

A Mahr Federal profilometer was used to capture the surface roughness of the laser coated samples. This is equipped with a stylus based tip which traverses the surface features. A photoelectric cell records the motion of the stylus tip which is further amplified. The radius of the stylus tip is 2μm. During each measurement the tip traces a length of 5.6mm on the surface and various roughness parameters like Ra (arithmetic mean deviation of the roughness profile), Rz (mean peak to valley height), Rmax (maximum roughness depth) were recorded. Six different profiles were analyzed for each sample and the average and standard deviation values are reported.

3.5.3 Fractal Nature of the Surfaces

SEM micrographs provided images of the laser processed samples. In order to appreciate the multi-scale level of the features observed in these images a fractal based approach was used. Images were recorded at different magnification and were then subjected to different image processing techniques prior to fractal determination. Using a fourier transformation the images were converted from spatial domain of brightness to a frequency domain, a noises filtering was performed the image was then converted to a binary digital image by thresholding. Thresholding was determined by converting images from gray scale of 0 to 256 into binary 8 bit images. Great care was taken while deciding the threshold value to ensure the minute details or features in the images are not neglected by directly comparing with the original figure. Automatic Thresholding

at 128 on the gray scale was not preferred. Implementing a box counting technique the fractal dimension was calculated from the image processed data. The macros available in the public domain software ImageJ was used for these image processing calculations. Image J software developed on a Java platform was provided by National Institutes of Health (NIH). It is freely available at their website http://rsb.info.nih.gov/ij/. The series of operations carried out to determine the fractal dimension is schematically shown in Figure. 3.2.

The box counting method is one of the common methods for calculating the fractal dimension of a self-similar fractal image. In this process the image is covered with square boxes of side length 'l' and the number of boxes needed to cover the image is counted and referred to as 'N(l)'. The process is repeated with different box sizes. The fractal dimension 'F_d' is calculated by equation below:

$$F_d = -\lim [\log_{10} N(l)]/ \log_{10}(l)] \text{ as } l \rightarrow 0 \qquad (3.3)$$

F_d is the slope of the plot $\log_{10} N(l)$ versus $\log_{10} (l)$.

3.6 Temperature Signatures

The chemical and morphological evolutions of the Ca-P coatings on Ti-6Al-4V alloy substrates depend on the temperature distribution during the heating and cooling cycle of laser processing, the derived cooling rates as well as peak temperatures attained. These calculations were done only for Ca-P coatings on Ti-6Al-4V and not for zirconia coatings. The major motivation for this work is based on the nature of complex chemical phases observed in CPT processing when compared with zirconia. Common knowledge of laser processing suggests faster laser processing results in higher cooling rates and lower peak temperatures.

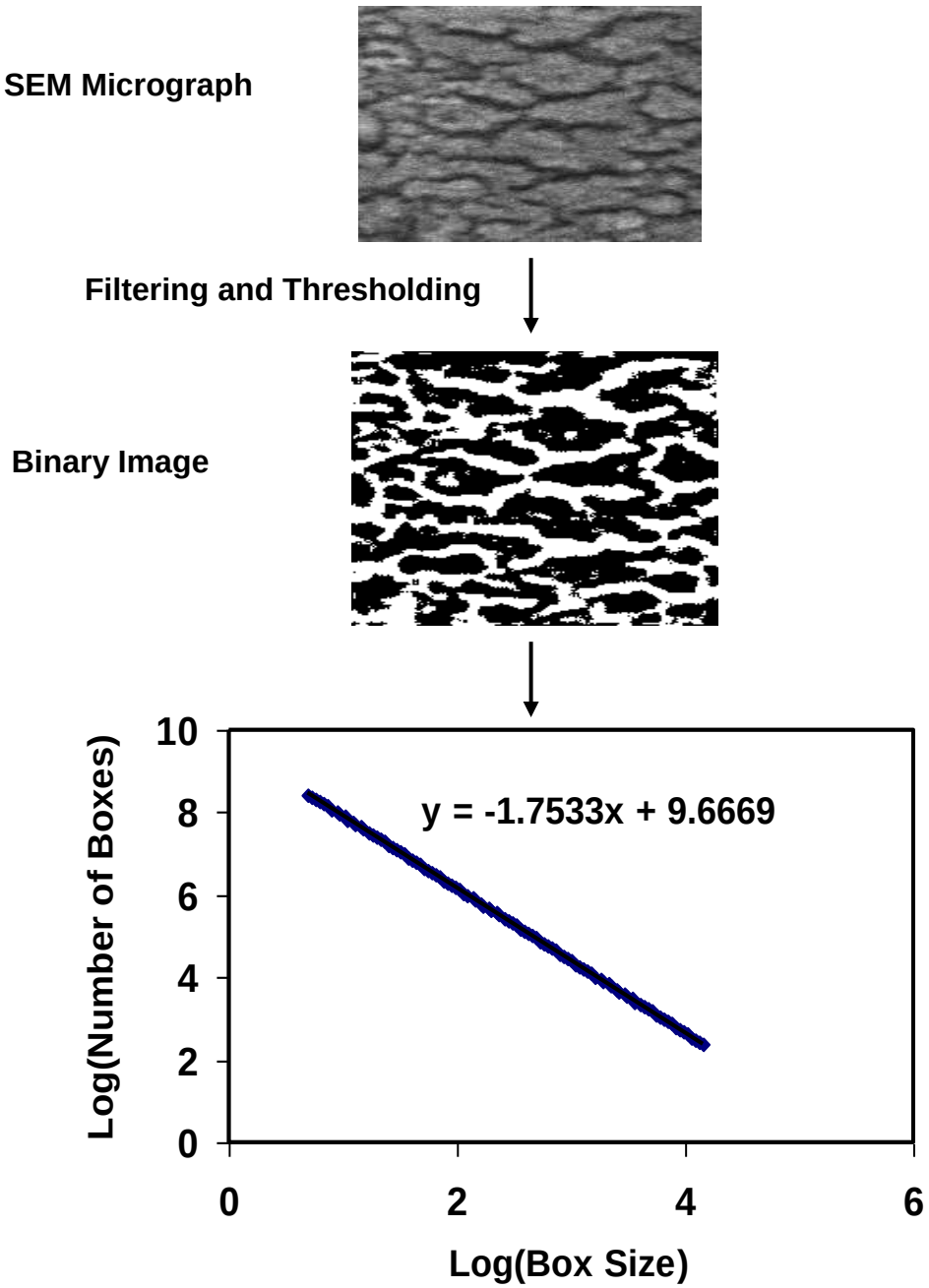

Figure 3.2 Steps involved in calculating fractal dimension starting with SEM micrograph. The slope in the Log(box size) Vs Log(Number of boxes) plot is the fractal dimension(Fd). In the present example Fd is 1.7533 [63].

For the zirconia system due to inertness and limited interaction with the Ti alloy phases there were no multiple reaction products. On the contrary poor absorptivity of CPT results in passage of laser energy into the substrate leading to significant melting of the substrate Ti phases and the consequent role played by it during re-solidification in the final morphology. In addition from chemical evolution perspective CPT decomposes at different temperature regimes, and undergoes reaction with Ti phases also at specific temperature regimes. As laser processing speed changed so did the temperature regimes and resulting chemical and morphological outcomes. Hence thermal modeling was critical for the present work.

Thermal calculations were done on a composite consisting of substrate Ti-6Al-4V and precursor Calcium Phosphate Tribasic (CPT) using COMSOL's ™ heat transfer transient mode. It is to be noted that the author was not involved in the development of software code for this model. His role in this effort is restricted to defining the boundary conditions, researching and providing input values and identifying the element for modeling purposes. The model used for temperature calculations incorporated various features like composite nature of material system, temperature dependent thermo physical properties, preheating due to multiple laser tracks and conduction, convection and radiation dependent heat transfer during laser processing under the formulations. Detailed information about assumptions and related references can be found from works of Samant et al. [69,70,71,72,73]. In the present model the CPT precursor represented in the form of a cuboid (50 mm × 100 mm × 40 μm) and coupled with another cuboid representing the Ti-6Al-4V substrate (50 mm × 100 mm × 3 mm) was simulated to create scenario similar to the real sample prior to laser processing. Figure 3.3 provides a schematic description of the substrate and precursor. The input energy and the time for which the energy was incident on the material surface (residence time, t_p) influence the temperature evolution and cooling rates. For

each processing speed the residence time was calculated by dividing the shorter axis of the laser beam (1.5 mm) by the laser processing speed along the axis. Based on this calculation the residence times of 72, 45 and 33 ms were determined for processing speeds of 125 cm/min, 200 cm/min and 275 cm/min respectively. The three speeds represent low, medium and faster laser processing By dividing the input power (850 W) with cross sectional area of the beam (7.5×10^{-6} m^2) the laser energy density I (1.13×10^8 W / m^2) was used for calculations in the model. For simplicity the computations were concentrated to high medium and low laser processing speeds of 275 cm/min, 200 cm/min, and 125 cm/min respectively For other speeds the computations are expected to remain in the same general trend for peak temperature and cooling rate evolutions that are provided by these three speeds.

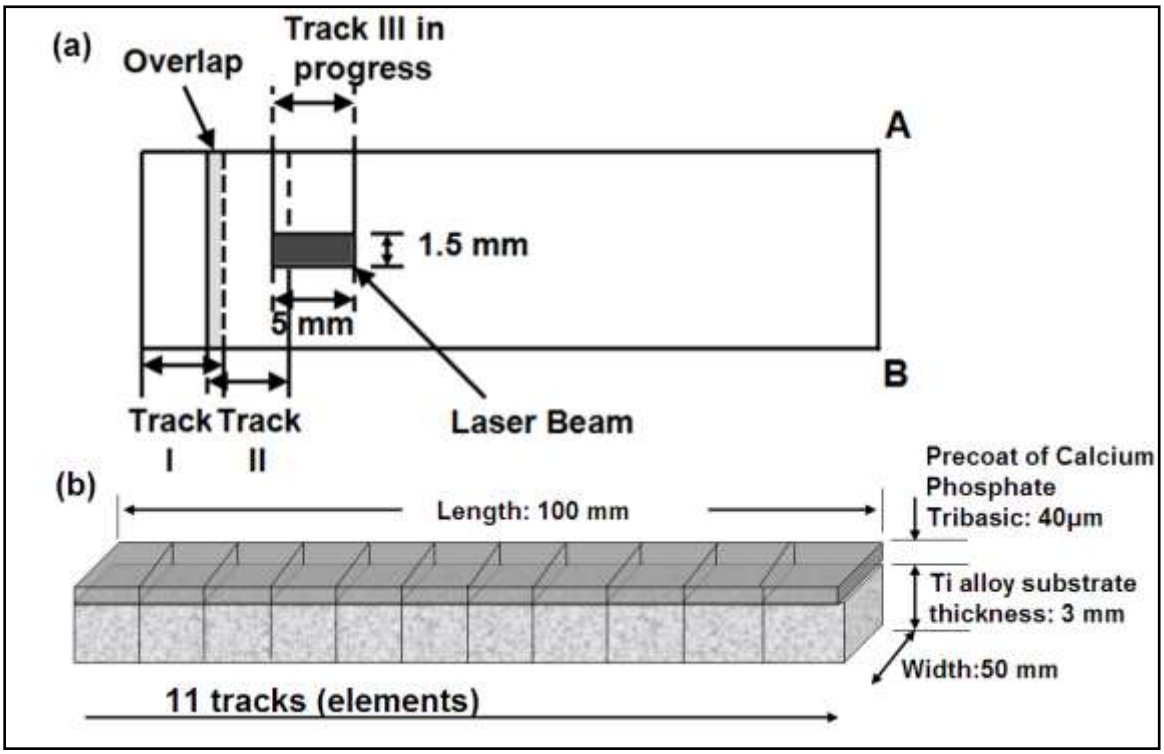

Figure 3.3 Schematic of the laser tracks and overlap patterns [66].

3.6.1 Preheating

The thermal profile of a track in not entirely dependent on temperature rise and fall in a particular track during laser processing but is also dependent on the laser processing in the adjacent tracks. This is called preheating. For each coating surface a total of 11 tracks were required to cover the area with a coating overlap of 15% (represented by the grey region) as shown in Figure 3.3. A three dimensional view of the coating precursor deposit and substrate elements is also presented in Figure 3.3. Going from A to B the motion of laser in a track was perpendicular to the longer axis of the beam (5 mm). The rise in the temperature as a result of laying down a laser track and the preheating caused by subsequent laser tracks was considered for the model. This was done by incorporating the input energy and residence time corresponding to a single track as the input parameters to the model. Using equations (3.4)-(3.6) the temperature distribution at the centre of each track was computed. At the same time the peak temperature at the location where the centre of the next track would lie was computed and was used as an input initial temperature parameter for the next track. This process was repeated till the computations for all the 11 tracks were completed, thus incorporating the effect of multiple tracks and associated pre-heating. Theoretically a particular track would have the pre-heating effect not just from the track preceding it but also from the several tracks prior to that track. However, it was realized from our computations that under the current laser processing conditions and with given material parameters employed the rise in temperature at a distance beyond next neighboring track was marginal (<150 °C). Therefore only pre-heating by the preceding track was considered in the present computations.

3.6.2 Conduction

As the laser imparts energy to the surface the transfer of thermal energy between neighboring molecules due to thermal gradient is facilitated by the process of thermal conduction. This process takes place from a region of higher temperature to a region of lower temperature and results in equalizing the temperature differences. Conduction takes place in solid, liquid, gases and plasma forms during laser processing. Fourier's second law was used for modeling the heat transfer process during the laser processing of the CPT precursor on the Ti-6Al-4V substrate is given by:

$$\frac{\partial T(x,y,z,t)}{\partial t} = \frac{k(T)}{\rho\, C_p(T)}\left[\frac{\partial^2 T(x,y,z,t)}{\partial x^2} + \frac{\partial^2 T(x,y,z,t)}{\partial y^2} + \frac{\partial^2 T(x,y,z,t)}{\partial z^2}\right] \qquad (3.4)$$

In the above equation $C_p(T)$*and* $k(T)$ are the variation in specific heat and thermal conductivity as a function of temperature, T is the temperature field, ρ is the density, t is time and x, y and z are the spatial directions. Incorporating the variation of thermal conductivity and specific heat as a function of temperature for the coating and the substrate were done for improved accuracy of calculations in the model [68,74]. The latent heat of solidification was accounted from the variation of specific heat as a function of temperature. For the first track at time t =0, the initial temperature of $T = T_0$ = 300 K was taken. However for subsequent tracks as explained earlier in order to incorporate the pre-heating effect, the maximum temperature resulted at the centre of the track under consideration by an previous track was taken as the initial temperature.

3.6.3 Radiation and Absorptivity

The electromagnetic radiation emitted from the surface of a material owing to its temperature is termed as thermal radiation. Thermal radiation loss from a material including all the frequencies

goes up with temperature and is governed by Stefan-Boltzman law. The difference between the energy absorbed during laser processing at the surface and the radiation losses is given by:

$$-k(T)\left(\frac{\partial T(x,y,0,t)}{\partial x}+\frac{\partial T(x,y,0,t)}{\partial y}+\frac{\partial T(x,y,0,t)}{\partial z}\right)=\delta aI-\varepsilon\sigma\left(T(x,y,0,t)^4-T_0^4\right)$$

$$\delta = 1 \qquad when\ 0 \le t \le t_p$$

$$\delta = 0 \qquad when\ t > t_p, \tag{3.5}$$

In the above equation I refers to the laser energy density, $k(T)$ refers to the temperature dependent thermal conductivity of the material in W/mK unit, ε stands for emissivity for thermal radiation, t_p refers to the residence time, σ is the Stefan-Boltzman constant (5.67×10^{-8} W/m^{2}K^4) and finally a refers to the absorptivity of the material. When the time (t) is less than the residence time, t_p the term δ takes a value of 1 and it is 0 when the time, t exceeds the residence time t_p. δ which depends on the time (t) ensures that the energy is input to the system only during the residence time and cuts off the energy supply after that. Experimental determination via in-situ absorptivity measurements in short duration high energy density laser process is extremely difficult. Hence based on exhaustive literature research the value of absorptivity of 0.1 (in the spectral range of 250 to 450 nm) for the coating material (Calcium Phosphate Tribasic) was considered [75]. There is not much of a data available for absorptivity / emissivity values of Calcium Phosphate Tribasic in the infrared region of 1064 nm wavelength. Since the laser energy is directly incident on the coating and is partially transferred to the substrate by heat transfer phenomena only the absorptivity aspect of the coating was considered for calculations.

3.6.4 Convection

Convection refers to heat transfer by movement of already heated particles in a fluidic system. Warmer particles owing to lower density rise while cooler particles move down. At the bottom surface of the sample the convection is given by :

$$-k(T)\left(\frac{\partial T(x,y,D,t)}{\partial x}+\frac{\partial T(x,y,D,t)}{\partial y}+\frac{\partial T(x,y,D,t)}{\partial z}\right)=h\,T(x,y,D,t)-T_0 \qquad (3.6)$$

In the above equation D refers to the thickness of the sample. This involves 40 µm thickness for the coating and 3 mm for the substrate. The heat transfer coefficient is represented by h in W/m^{2}K. The variation in heat transfer coefficient was adjusted for function of temperature [76].

Based on these computations the temperature profiles and their corresponding cooling rates were calculated. These are then analyzed for their effects on the microstructure and kinetics of phase transformation are discussed at various stages in the results and section of this study. So far we have covered phase and morphological analytical methods along with thermal model used for their prediction. Going forward the following sections will discuss experiments done to determine the efficacy of these engineered surfaces for biocompatibility.

3.7 Biocompatibility Studies

Understanding the biocompatibility of the laser processed coatings is essential for speculating the osteointegration behavior of the surfaces. Few simple experiments discussed below are performed to comprehend this behavior. These invitro testing involved wettability studies,

biomimetic precipitation in simulated body fluids and wear in simulated body fluid environment. The following sections will discuss the experimental procedures adopted for these evaluations

3.7.1 Wettability studies (Contact Angle Measurements)

Wettability evaluations via contact angle studies are useful for evaluation of solid surfaces for adhesion, determining the hydrophilic and hydrophobic nature of the surfaces. Contact angle measurements were made using Tantec half angle^{TM} technique. In this technique a 5 μL droplet of water was dropped via an over head syringe onto the surface if interest. Light was shined on to the droplet projecting a shadow onto a white plane. Using a magnifier attachment the shadow is brought into focus by changing the optics and the dimensions of the shadow were measured. Parameters like: flow rate, height of dropping, base line determination, optics adjustment and time of measurements were optimized prior to experimentation. Typically the liquid droplets took 4-5 seconds to stabilize and usually the sample was raised until the surface of the specimen was touching the droplet of liquid emanating out of the needle nozzle.

3.7.2 Hydroxyapatite Precipitation (Simulated Body Fluid immersion study)

In order to examine the precipitation of HA as an indirect indication of biocompatibility of modified surface, the laser surface modified samples were immersed in conventional Simulated Body Fluid (SBF). SBF was prepared as per standard procedures reported in literature [77]. The concentrations represent the conventional SBF concentrations as per Oyane et al. The concentrations of the ions present in this conventional SBF represent blood plasma except for HCO^- and Cl^- ionic concentration. Although there are other modified SBF concentrations

proposed the objective in using conventional SBF was to compare the results with wealth of published literature. The apparatus used for preparing SBF were cleaned with HCl, detergent and distilled water. 700ml of water was taken into a Pyrex glass flask and the chemicals listed in Table 3.1 were sequentially added. At 37^0C the pH of the liquid was measured and brought to 7.4 by titrating with 1.0M HCl. Ultra pure water was added to this liquid to make it 1000 mL. This liquid was then transferred into small propylene bottles that contained the laser processed samples. The sample was immersed for 14 days in SBF maintained at a constant ph of 7.4 at 37^0C and refreshed after every 24 hours. In addition a 5 day experiment was conducted where after every 24 hours of immersion in SBF the samples were taken out, dried and characterized using SEM and x-ray diffraction (XRD) analyses for morphological and chemical evolution of precipitates during SBF immersion.

3.8 Mechanical Evaluation of Coatings

The mechanical performance of the coating and substrate are critical from a reliability perspective. Bioimplants undergo wear during usage and finally loosen. Therefore understanding of the wear performance of the engineered synthetic surfaces when immersed in bio-environments is critical. To simulate this condition a unique modified pin-on-disc arrangement was designed with a SBF solution as the medium inside a cylindrical rotating. The schematic in Figure 3.4 describes this setup. The pin made of zirconia was 50 mm long and 3 mm diameter. Zirconia is a biocompatible material frequently used as a mating material for metallic stems in hip replacement applications. The base of the zirconia pin was flattened by grinding and polishing with silicon carbide grit papers. The surface of interest (in this case laser coated surface) was fixed to the bottom of the cylindrical wear cell and this is filled with SBF liquid.

Table 3.1 Chemicals and amounts used to prepare SBF. [77]

Reagent	**Purity/%**	**Amount**
NaCl	>99.5	8.036g
$NaHCO_3$	>99.5	0.352g
KCl	>99.5	0.225g
$K_2HPO_4.3H_20$	>99.0	0.23g
$MgCl_2$.$6H_20$	>98.0	0.311g
1.0-HCl	-	40mL
$CaCl_2$	>95.0	0.293g
Na_2SO_4	>99.0	0.072g
Tris (Hydroxlymethyl) aminomethane	>99.9	6.063g
1.0M-HCl		~0.2mL

While the pin was held static the cylinder was rotated at 0.042 m/s under a load of 0.9 Kg for a traverse distance of 450 m (a total of 12000 rotations). After each cycle the weight of the test coupon was measured. The wear rate was determined by weight-loss per unit surface area of the wear track. The surface area of the wear track is the difference between the outer and inner areas calculated from outer and inner diameters of the wear track respectively.

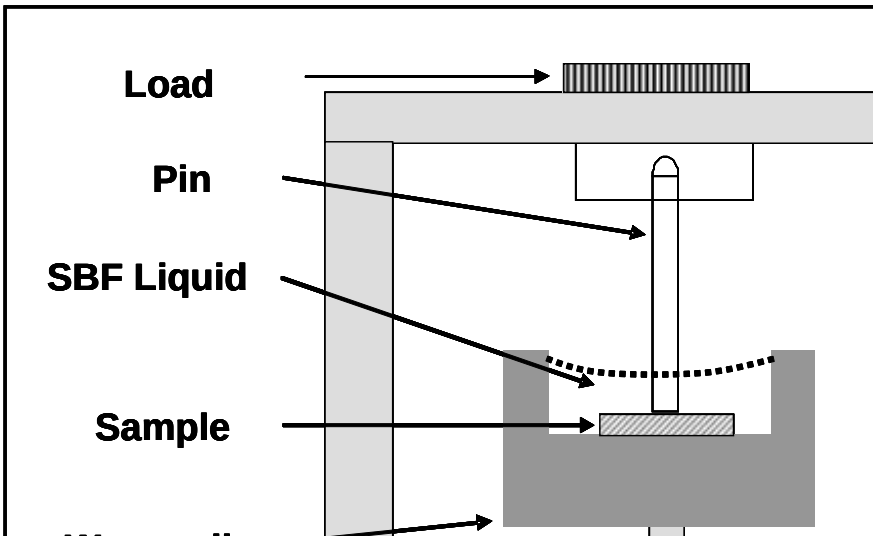

Figure 3.4 Schematic of the wear cell with modified pin on disc arrangement.

Chapter 4

Laser Induced Zirconia coating on Ti-6Al-4V

4.1 Introduction

A novel simultaneous coating and texturing laser processing operation has been proposed for bioimplant application. To evaluate the feasibility of the concept a discovery phase was planned. During the discovery phase zirconia precursor deposit was laser processed on Ti alloy surfaces. The objective of this discovery phase was to see the feasibility of simultaneous coating of the zirconia on the surface while simultaneously introducing the texturing aspect in the final morphology primary dictated by melting and re-solidification of underlying Ti alloy. Since zirconia is inert, does not decompose and has higher boiling point ($4500^{o}C$) it would be a good candidate for evaluating the feasibility of this concept. The end goal was to see if the final coating did retain zirconia and if there were any multi-scale features that would promote biocompatibility. The preset chapter discusses results and discussions from this discovery phase. Some content presented in this chapter has already been published in Journal of Materials Science: Materials in Medicine in 2006 by Anil Kurella as the primary author [63]. The primary author's contribution to these papers includes but not limited to selection of topic, literature survey, experimentation, analysis, technical writing, all of the figure drawings and compilation. The coupons were processed at 3 different speeds 40 cm/min, 160 cm/min, 290 cm/min at a constant power of 25W under a 10kHz pulse frequency. Knowing that zirconia has good absorptivity in the infrared region (0.6) and to induce melting from underneath Ti alloy substrate to influence the final morphology during solidification power intensities close to $2x10^{6}$ W/cm^{2}

per pulse was chosen. It has to be recollected that Gyorgy et al. have reported 10^8 W/cm^2 is needed for melting of Ti per pulse [55]. The intensities used here are few orders of magnitude lower because of the multi-pulse mode adopted here. The three speeds were chosen from the high, medium and low speeds ranges of the motorized workstation attached to the laser. The chemical and morphological analysis of the coatings produced in this discovery phase is presented in the following sections in this chapter.

4.2 Phase Evolution of Substrate and Coating

Laser surface engineering is an energy intensive operation with changes in laser processing speeds influencing the total heat input and subsequently the phases evolution in the final coating and substrate material. X-Ray diffraction analysis of the laser processed surfaces is presented in Figure 4.1a. In the figure the XRD patterns from laser processed coatings are overlaid with that of precursor zirconia powder and Ti alloy base substrate. From the XRD patterns it appears that the zirconia powder consisted of tetragonal phases. The two small peaks at 28.1^0 and 30.6^0 corresponded to the monoclinic phase in the precursor powder. The laser processed coatings on Ti-6Al-4V substrate showed the existence of zirconia peaks along with the substrate peaks. As the speed of the laser processing increased the intensity of {111} peak corresponding to retained zirconia on the surface decreased (Figure. 4.1). The change in the intensity of {111} peak can be semi-quantitatively correlated to the variation in amount of retained zirconia in the coatings.

The maximum temperature attained during a process is dependent on the total heat input and the laser processing speed. [78,79]. As the processing speed decreases, the interaction time of laser beam with the material and subsequently the maximum temperature attained by material increases.

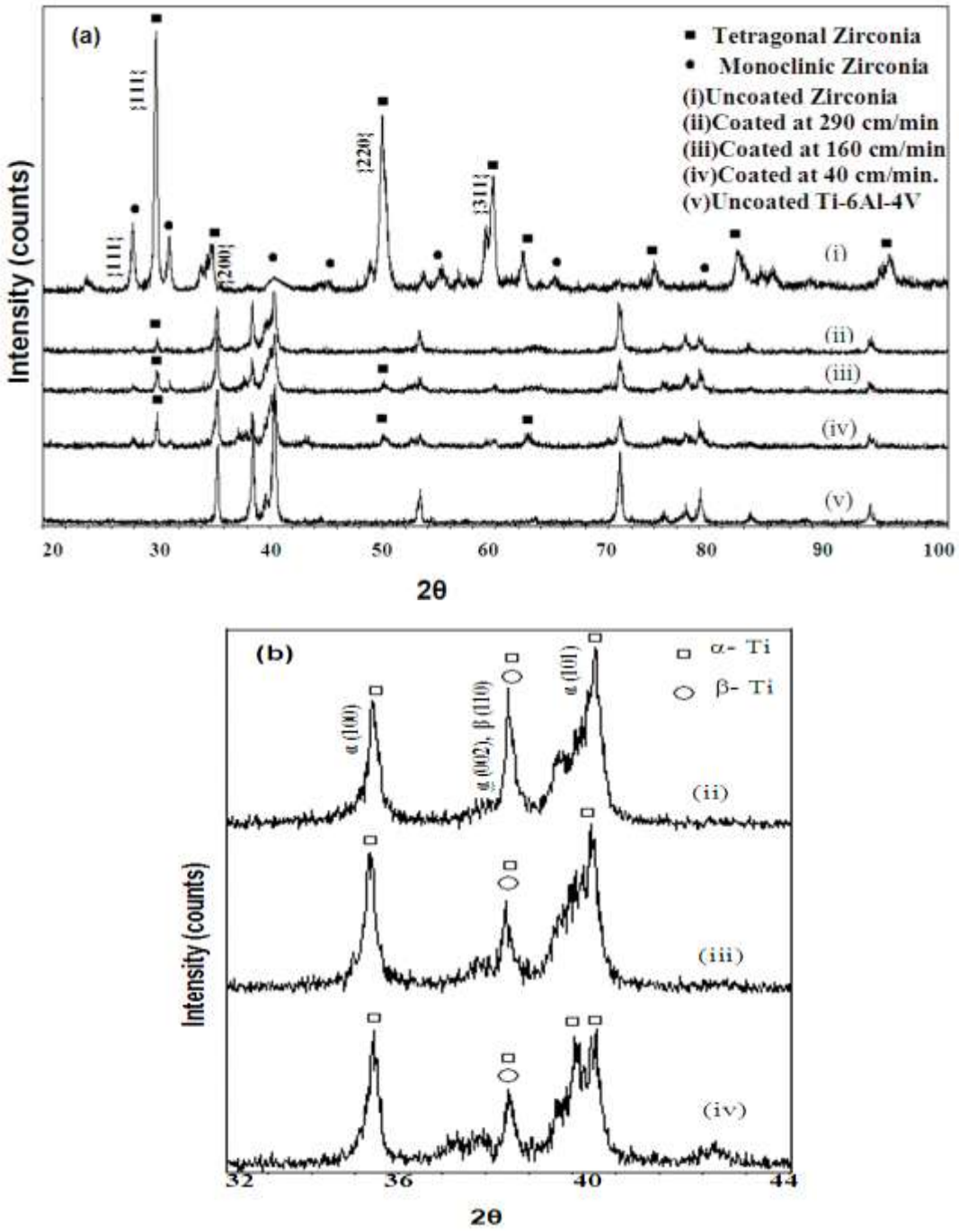

Figure 4.1 XRD spectra for (a) Uncoated Ti-6Al-4V, precursor zirconia powder along with laser processed coatings produced at various speeds and (b) Detailed XRD patterns between 32^{o}-44^{o} for further phase identification [63].

The level of maximum temperature is expected to influence the nature and extent of interaction between the coating precursor and the melted portion of substrate material [79,80]. Therefore in the present work the amount of retained zirconia in the laser modified region is expected to increase as the processing speed decreased which may be the major cause for high intensities of zirconia peaks at lower processing speeds. In the same window of processing conditions the modulation in laser speed offered different possibilities for Ti-alloy phase transformations. Figure 4.1b shows a detailed X-ray scan of the laser processed samples between $32^{o} - 44^{o}$ where major intense peaks of Ti exist. The rate of cooling is influenced by the speed of laser processing [78]. In the present case it was observed that processing at 290 cm/min would set up extremely high thermal gradients compared to 40 cm/min. Under such high thermal gradients the kinetics of the phase transformation is greatly influenced by events like incomplete phase transformation, formation of unconventional phases, etc. [81,82,83].

The XRD data shown in Figure 4.1 tend to show this pattern. Typically, heat treatment of α+β Ti phases or only β-Ti phase alloys is expected to convert all β-Ti phase into α-phase [84]. In the present case thought there seems to be the presence of some amount of residual β –Ti at all processing speeds (Figure. 4.1) Using a semi-quantitative analysis a direct comparison between a ratio of the X-ray diffraction intensities of the retained β-Ti to α-Ti was determined and plotted in Figure. 4.2 [85]. From the XRD patterns (Figure 4.1b) it can be seen that for samples processed at 40 cm/min there appeared multiple sub peaks corresponding to {101} class of reflections. This could be attributed to the cyclic thermal heating and cooling cycles during successive laser passes setting up varying thermal gradients in previously melted tracks. The transformation from β-Ti to α-Ti is monovariant in nature and hence the phases precipitated at different cooling rates are expected to have different morphologies. This may result in formation

of α-Ti phases with various ‘c’ and similar ‘a’ lattice parameter [84]. With the increase in the speed of laser processing sufficient time is not available to form different α-Ti phases. This results in fewer multiple peaks in XRD spectra (Figure. 4.1b). The alpha phase resulting from such rapid quenching process is commonly referred to martensitic α [86]. This martensitic α is typically associated with distortion of the lattice structure resulting in a strained material. Martensitic α is usually tough, hard and typically possesses better fatigue properties than α-Ti [86]. This observation is in line with the observations recorded by the author and with his fellow researchers reporting on the enhanced physical (tribological) and chemical (corrosion) properties of Ti alloys [87,88].Such modification for the amount and type of phase within the coating and the region of substrate near the interface with the coating is extremely important for tailoring the properties for biological applications as discussed in the following chapters in the present work.

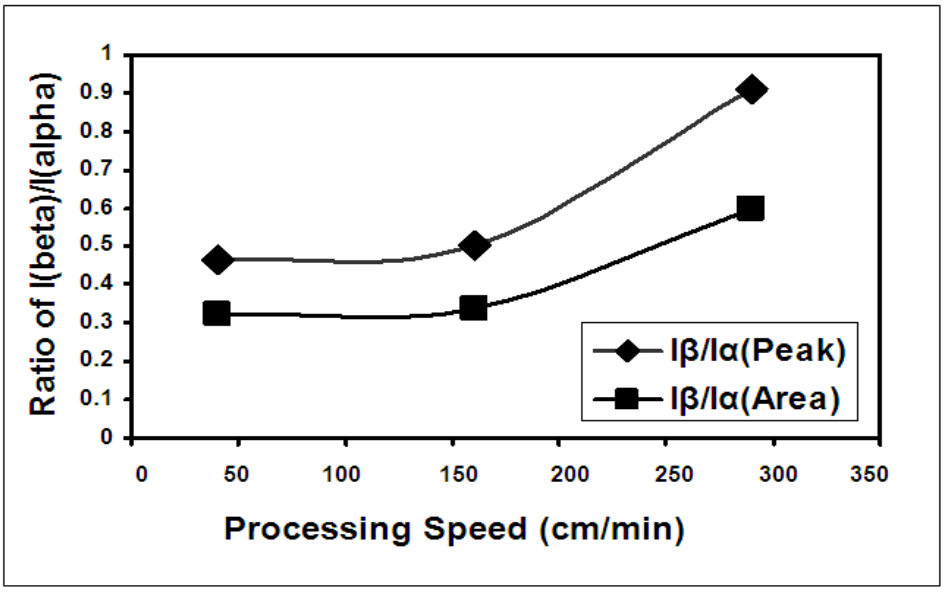

Figure 4.2 Ratio’s of retained Iβ/Iα plotted for various laser processing speeds [63].

4.3 Morphological Evaluation of the Textured Coatings

The surface topography is influenced by the chemical phase transformations and solidification fronts induced during laser processing [89]. The following section deals with characterizing the complex surface morphology and attempts to correlate it with laser processing conditions. Figure 4.3 presents the scanning electron microscopy images of the surface morphologies produced at various laser processing speeds. Three dimensional surface plots based on gray scale intensities of the micrographs were generated using the macros available in the Image J software. As can be visualized from the images the extent of overlap the depth of the depth of features is seem to vary with processing speed.

The laser processing speed influences the extent of laser beam interaction (in terms of time and total heat input to material. The laser speeds also dictates the distance between the subsequent laser pulses and the extent of overlap. These two parameters together in turn influence the final surface morphology. As can be seen in Figure 4.3, each laser pulse produces a crater of solidified material with trough around the periphery and relatively flat region at the center of the crater. Increase in the processing speed decreases the overlap between subsequent pulses (craters), which further decrease the trough region (Figure. 4.3a) and thus affecting the roughness of the processed surface region. This coupled with the fact that multiple pulsing in a linear track followed by laying down multiple linear tracks in overlapped manner during the coverage of the entire coating surface changes the thermodynamics of the molten material which in turn can affect the nature and extent of trough and flat regions. Such a processing would result in complex relationship between roughness and laser processing parameters of the surface as experienced in the following study.

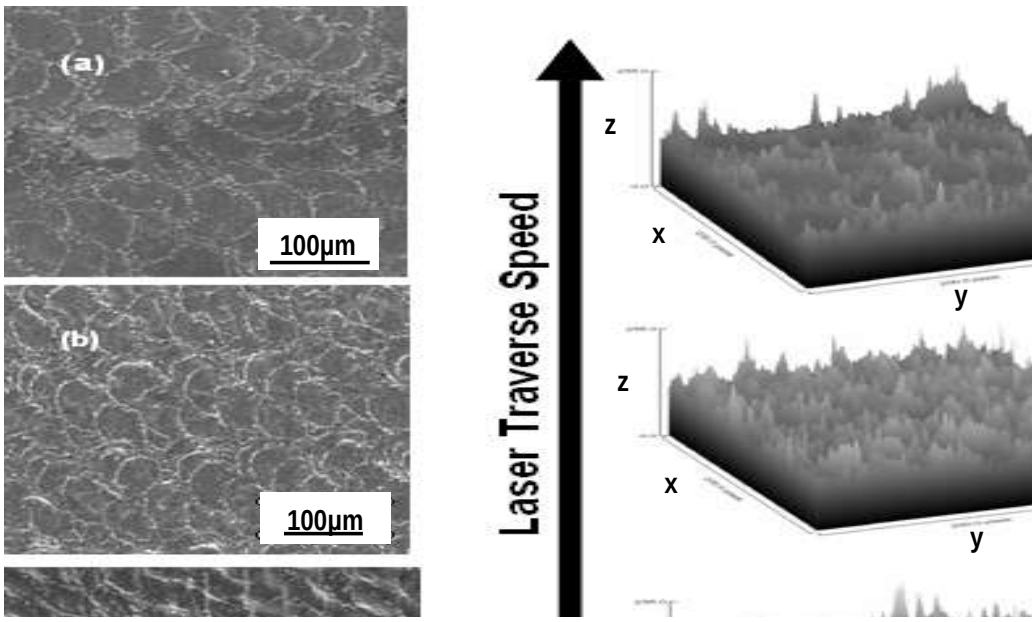

Figure 4.3 Low magnification images of textured coatings at (a) 290 cm/min (b) 160 cm/min(c) 40cm/min. Corresponding simulated 3D surface profiles are also presented [63].

Observing the textures closely at higher magnifications showed multi-scaled features. Figure 4.4 shows the micrograph of a coating surface processed at 40 cm/min. At higher magnification a multi-scale texture was observed. Laser processing at other speeds (160 cm/min and 290cm/min) showed similar multi-scale features. The laser processing speed of coupled with number of pulses per unit area seems to have influenced the nature of the surfaces. Profilometer based roughness characterization was carried out to interpret these features quantitatively. However it has to be realized that roughness values determined by profilometer measurements are limited when explaining multi-scale nature of morphological features on the surface however they are representative of roughness (in terms of crests and troughs) at a particular length scale corresponding to the size of the stylus tip.

The change in various roughness values determined for the three different speeds of operation is presented in Figure 4.5. It can be seen that laser processing at 160 cm/min produces higher roughness values for Ra (arithmetic mean deviation of the roughness profile), Rz (mean peak to valley height), Rmax (maximum roughness depth) when compared to the other conditions. As explained earlier the number of pulses per unit area and the effect of repeated passes during the laser processing operation influence the nature of the surface produced at a particular processing speed. Looking into the roughness profiles seems to provide further information.

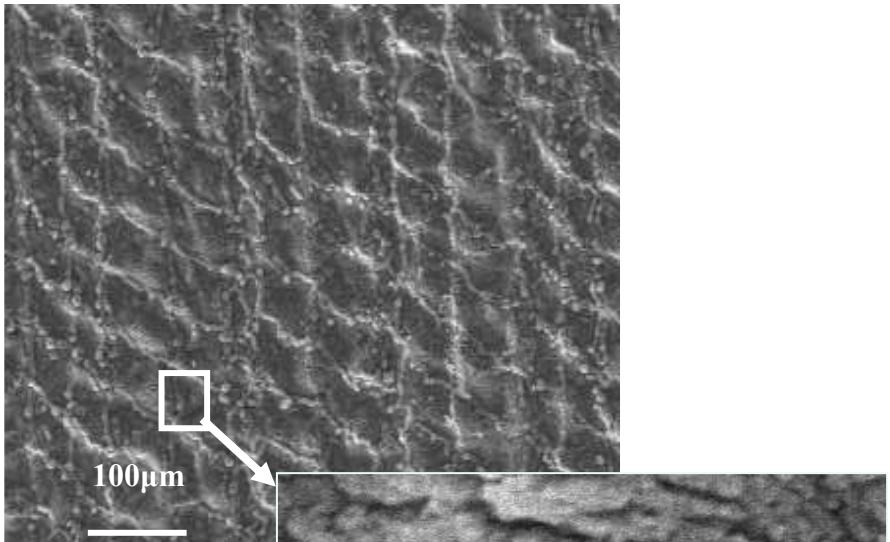

Figure 4.4 Multi-scale features shown in the micrographs imaged on a sample laser processed at 40 cm/min [63].

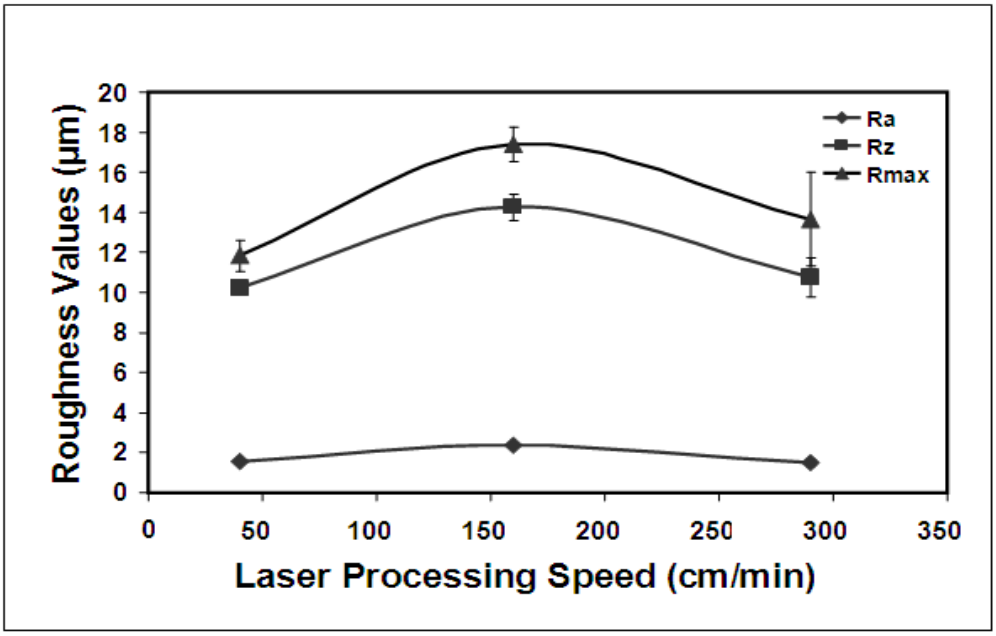

Figure 4.5 Variation in roughness with laser processing speeds [63].

The lowering in roughness values for the sample processed at 40 cm/min can be attributed to the softening of the surface peaks (crests) due to the repeated passing of the laser source as shown in Figure 4.6a. Apart from this, the number of pulses per unit area decreases as the speed of processing increases due to which the temperature of the peaks is repeatedly maintained at lower level resulting in limited or no re-melting of the solidified peaks leading to a roughening effect on the surface. The smoothening effect increases and roughness decreases as the processing speed decreases. That's why roughness is higher for 160 cm/min than 40 cm/min. On further increase in laser speeds however the roughness drops too. Considering the high processing speeds of 290 cm/min the lowering in surface roughness can be attributed to the fact that the numbers of pulses per unit area are few and the degree of overlap is largely limited due to which the topography consists of alternate rough and smooth areas as represented in Figure. 4.6b. Hence intermediate speeds correspond to higher roughness values than low or high speed processing conditions. As previously observed the laser surface processing resulted in multi-

scale structures (Figure. 4.4) and thus conventional surface characterization parameters like Ra, Rz and Rmax limit our range of explanations to just one length scale corresponding to that of the stylus tip. A fractal based approach is needed to appreciate the multi-scale level of the features on the laser processed surface. A parameter called fractal dimension (F_d) was calculated based on a sequence of image processing techniques implemented on the SEM images collected. The sequence of image processing techniques and the sources for Image J software are described in detail in the experimental section of this work. The macro called box counting technique was implemented to predict the fractal dimension. This process was repeated for multiple SEM images collected at different magnifications. All the imaging was done under similar operating conditions and all the TIFF images had the same digital resolution.

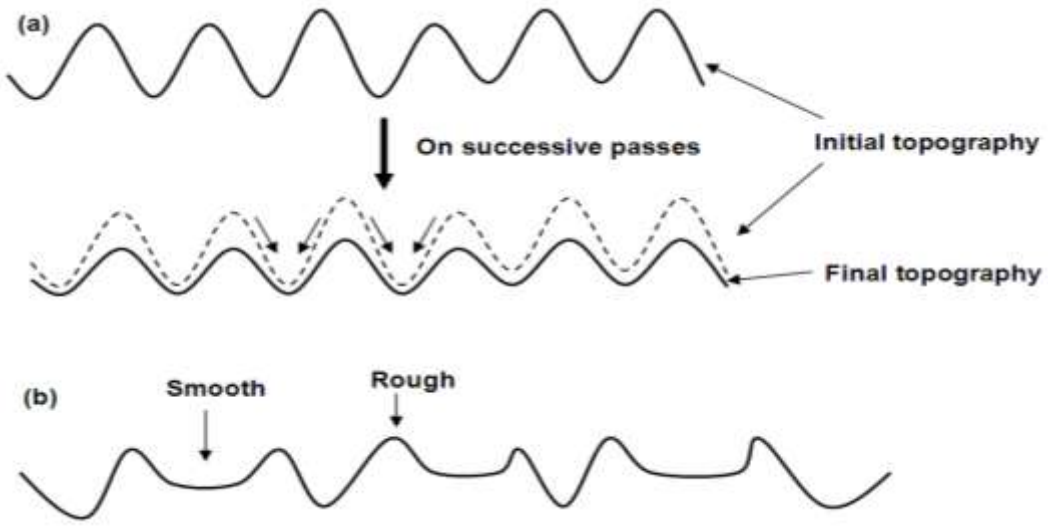

Figure 4.6(a) Schematic drawing showing a possible smoothening effect at lower processing speeds like 40 cm/min. (b) Alternate rough and smooth surface is produced due to past laser processing at 290 cm/min [63].

At each magnification the length per pixel was calculated for and this forms the basis for comparing the fractal dimensions at different magnifications as shown in Figure 4.7. From the graph in Figure 4.7 it can interpreted that all the three processing conditions exhibited consistency in fractal dimension values at certain length scales. Clearly, the laser surface processing at 40 cm/min resulted in surface features that are fractal across a large number of length scales. Faster laser processing conditions seems to have resulted in fractal nature over limited length scales. At this point of time it is important to correlate fractal dimension variation for various laser processing speeds with corresponding roughness values at comparable length scales. For fractal dimension values obtained at length scales of 2μm (comparable to the length scale of profilometer stylus tip sued for roughness measurements) are captured in Table 1. As can be noted, the changes in fractal dimensions is comparable to the corresponding roughness variation establishing the fact that fractal dimensions can be correlated with general nature of roughness measurements and fractal based predictions are reliable parameters for evaluating features that span multiple length scales. In this present work a novel simultaneous laser coating and texturing of zirconia was carried out on Ti-alloy surfaces. Zirconia with its high melting point, boiling points and no dissociation products was the ideal candidate for the feasibility of this concept. The objective to retain zirconia while inducing a morphology primarily dictated by melting of underneath Ti alloy substrate was achieved. The surfaces have features that are hierarchically integrated at multiple length scales. The number of pulses and successive laser passes seem to have influenced the roughness of the final surface. A fractal based approach was used to interpret the multi-scaled surfaces and has been successfully correlated with the surface roughness values. That said it has to be commented that there was some evaporative loss of zirconia which more than what was anticipated

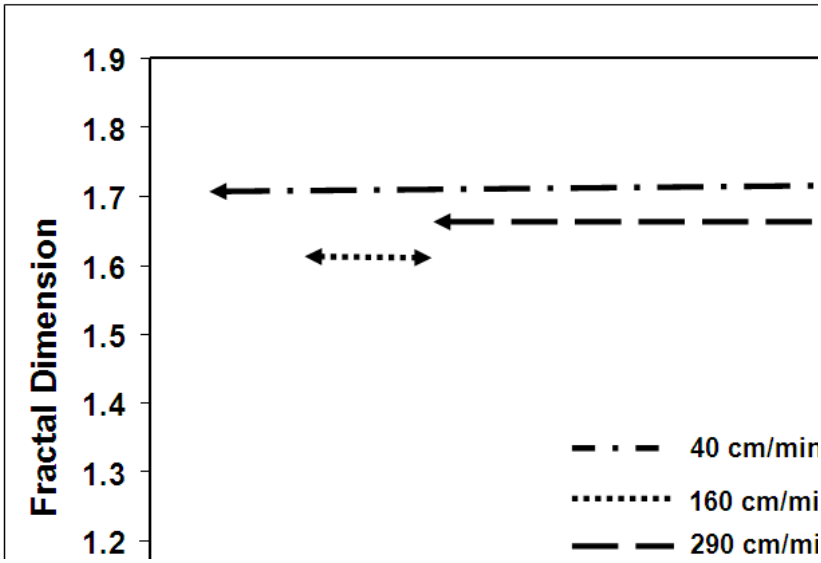

Figure 4.7 Plot showing length scales across which consistent fractal dimensions were observed for various laser processing speeds[63].

Table 4.1 Fractal dimension at different laser processing speeds [63].

Speed of Laser Processing	Fractal Dimension at length scale of 2µm per pixel
40 cm/min	1.7427
160 cm/min	1.8566
290 cm/min	1.6831

.

.There was also significant melting of the substrate Ti alloy leading to high degree of crater/trough formation and its subsequent influence on eventual morphologies. This suggests that the input intensities should be much lower than 10^6 W/cm$^{2.}$. The starting point for this work were the observations from Gyorgy et al., where they commented intensities in the range of 10^8 W/cm^2 were needed for surface melting of Titanium [55]. Clearly multi-pulsing action of the laser could have resulted in higher energy transfer leading to the effects discussed above.

Also the role played by absorptivity of zirconia in the infrared laser range need to be considered. In-fact Lawrence reported that there is limited variation in the absorptivity values of zirconia with wavelengths from infrared to ultraviolet range [67]. Typical values of absorptivity for Zirconia are around 0.6 in the infrared range. This suggests greater absorption of incident laser energy and subsequent thermal effects could have led to vaporization of the precoated zirconia. In general, however these learning's paved way for experimenting with more challenging materials like CPT. Calcium phosphate material as discussed in earlier chapters are highly biocompatible and at the same time challenging to coat. The boiling point of CPT is 3227^{o}C and it dissociates at lower temperatures when compared to zirconia. So lower laser energy intensities are to be experimented with going forward. On the other hand with lower absorption coefficients (0.1) there is also a greater influence of Ti alloy substrate melting

resulting in conductive and convective heat transfer resulting in enhanced interaction between the decomposition phases of calcium phosphate with Ti alloy [50].

Chapter 5

Laser Induced Ca-P coating on Ti-6Al-4V

5.1 Introduction

The successful coating of zirconia on Ti alloy during the discovery phase paved way for experimenting with laser assisted Ca-P based coating on Ti alloy surfaces. A coating containing Ca-P constituents is desired because it is bioactive in nature and is expected to have enhanced osteointegration. In addition, if these coatings are hierarchically evolved at multiple scales, they will present an organization that will mimic natural biomaterials like bones in human systems. However, the challenge with Ca-P based materials is its higher degree of dissociation and vaporization due to its low melting and boiling points. One of the learning's from pulsed laser processing on zirconia involved the understanding the role of melting and re-solidification patterns of underlying Ti alloy substrate for the given processing conditions. Hence instead of a pulsed laser a continuous wave Nd:YAG laser operation was sought for CaP coatings so that the energy is spread over a broader beam area of 5mm x 1.5 mm and reduce the extent of vaporization of precursor. This chapter discusses the results and discussions from these experiments. Some content in this chapter has already been published in Journal of Minerals, Metals and Materials Society in 2005 [62], Actabiomaterialia in 2006 [64], Materials Science and Engineering-C in 2008 [65], Journal of Applied Physics in 2009 [66] with Anil Kumar Kurella being the primary author. The references listed provide complete information about these publications. The primary author's contribution to these papers includes but not limited to

selection of topic, literature survey, experimentation, analysis, technical writing, all of the figure drawings and compilation.

As discussed earlier (in experimental section 3.3.2) the laser processing was carried out at a constant power of 850W while the laser scanning speed was varied from 100 cm/min to 225 cm/min (Experiment A). A second set of experiments using the same parameters at laser scanning speeds varying from 100 cm/min to 275 cm/min was done to determine the repeatability of the process as well as to study the thermal effects (on phase and morphological evolution) at extended thermal conditions of temperature and cooling rates (Experiment B). The chemical and morphological observations from these two experiments were essentially similar, comparable, and followed the expected trend. Hence for most part the discussion of experimental results is intertwined and is representative of laser processing in those regimes.

5.2 Phase Evolution

X-ray diffraction (XRD) patterns of coatings processed by varying laser scanning speeds from 100 cm/min to 225 cm/min (Experiment A) are presented in Figure 5.1. The major phases that are identified from XRD patterns are Calcium Titanate ($CaTiO_3$), Titanium Dioxide (TiO_2), Tri-calcium Phosphate (TCP), Calcium Oxide (CaO) along with Ti phases from the substrate. The XRD results from Experiment B where the laser processing speeds were carried out from 100 cm/min to 275 cm/min and is presented in Figure 5.2. Similar phases as identified in Experiment A were observed in this case too. Using the JADE software available on the Norelco XRD machine the peak intensity values for various phases was measured. These intensity values were then normalized with respect to the Ti peak intensity. In general, the nature of the phases present in both the experiments was same.

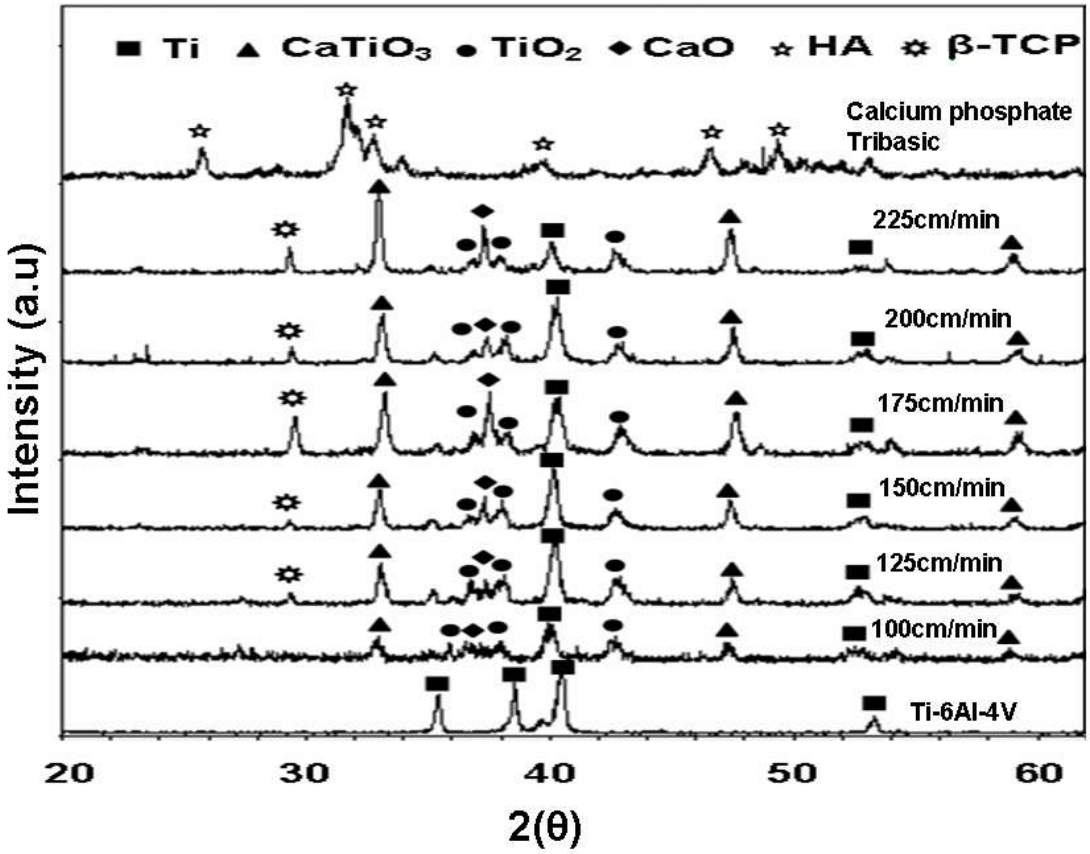

Figure 5.1 XRD patterns from various laser processing speeds overlaid with Ti-6Al-4V and Calcium phosphate tribasic patterns [64].

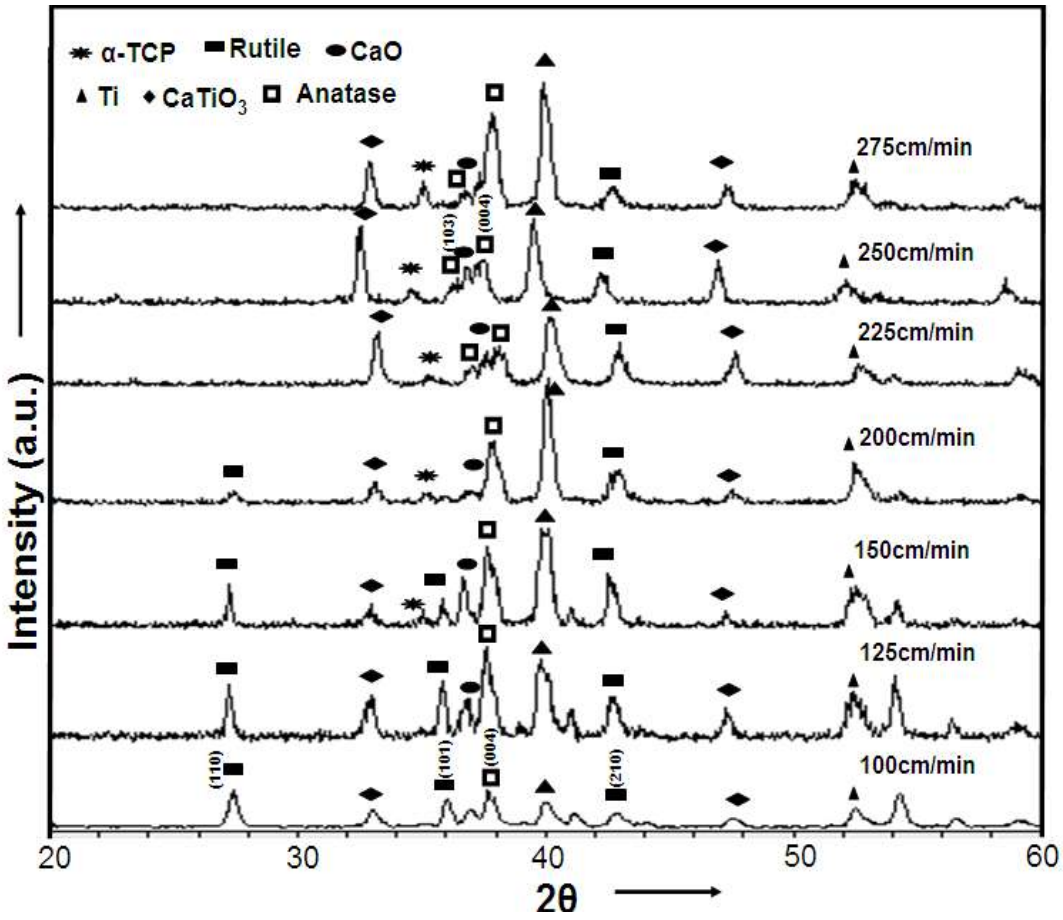

Figure 5.2 XRD patterns overlay for coatings laser processed with speeds varying from 100 cm/min to 275 cm/min [66].

Figure 5.3 presents the variation of the key phases for various speeds in Experiment A using this semi quantitative analysis. Similar observations were recorded for Experiment B and are presented in Table 5.1 In addition the multiple TiO_2 phases information is also provided in the table (In Figure 5.3 TiO_2 corresponds to rutile (101) only). From the XRD patterns and the semi-quantitative analysis it can be clearly seen that there is a trend in phase evolution with the variation in the laser processing speed. It is to be noted that the there seems to be higher presence of $CaTiO_3$ at faster laser processing speeds.

Table 5.1 shows that at lower speeds there is higher presence of TiO_2 (anatase and rutile) constituents. This could be attributed to greater vaporization of precursor material at lower processing speeds due to higher temperatures reached during processing. Thermal computations performed using model mentioned earlier in the experimental section and presented later indicate the development of temperature high enough for melting/decomposition and vaporization of precursor leading to greater exposure of substrate Ti alloy during slower laser processing speeds. When exposed to elevated temperatures substrate Ti readily oxidizes into TiO_2. Different levels of TCP and CaO peaks are present at all processing conditions.

Similarly due to high temperatures attained during laser processing the precursor Calcium Phosphate Tribasic (CPT) undergoes chemical and physical changes through one of the following possible steps: (i) breakdown into Tricalcium Phosphate (TCP), Tetracalcium Phosphate (TTCP), Calcium Oxide (CaO) and Phosphorus Pentoxide (P_2O_5) (ii) complete melting and re-solidification into Amorphous Calcium Phosphate (ACP), and (iii) partial dehydroxylation into Oxyhydroxyapaptite (OHA) and partial amorphization [90,91].The higher the temperature reached the more melting and decomposition of the CPT takes place.

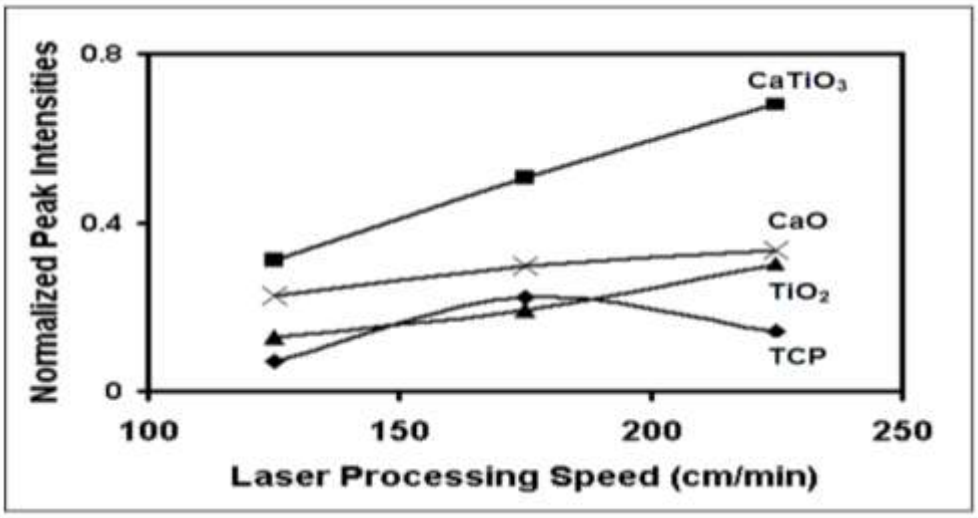

Figure 5.3 Normalized XRD peak intensity variations for various phases with laser processing speeds in Experiment A [64].

Table 5.1 Normalized peak intensities for various phases for low (150 cm/min) and high (250cm/min) laser processing speeds. [66]

.Speed (cm/min)	**TiO_2 rutile (110)**	**$CaTiO_3$**	**TCP**	**TiO_2 rutile (101)**	**CaO**	**TiO_2 anatase (004)**
250	0.07	0.91	0.2	0.23	0.47	0.52
150	0.42	0.17	0.11	0.25	0.48	0.83

Table 5.2 lists the melting points of these key materials considered for discussion in this research [90, 91]. The set of reactions given below explain the existence of chemical phases in the coating.

$$Ca_5(PO_4)_3(OH) \longrightarrow Ca_4P_2O_7 + Ca_3(PO_4)_2 \quad (5.1)$$

$$Ca_4P_2O_7 \longrightarrow Ca_3(PO_4)_2 + P_2O_5 \quad (5.2)$$

$$Ca_3(PO_4)_2 \longrightarrow CaO + P_2O_5 \quad (5.3)$$

$$Ti + O_2 \longrightarrow TiO_2 \quad (5.4)$$

$$CaO + TiO_2 \longrightarrow CaTiO_3 \quad (5.5)$$

.

In the above equations:

$Ca_5(PO_4)_3(OH)$: Calcium Phosphate Tribasic (CPT)

$Ca_3(PO_4)_2$: Tri Calcium Phosphate(TCP)

$Ca_4P_2O_7$: Tetra Calcium Phosphate (TTCP)

CaO : Calcium oxide

$CaTiO_3$: Calcium Titanate.

It has to be mentioned that there was no Oxyhydroxyapaptite (OHA) phase detected in the final coating from XRD analysis. It is interesting to note the presence of three phases P_2O_5, CaO,TiO_2 that have a tendency to form glass as reaction products from the above mentioned equations. These details are discussed at a later stage in this report.

Table 5.2 Melting temperatures of the key phases observed in the coatings. [66]

Phase	**Melting Temperature**
CaO	2570°C (2843K)
$CaTiO_3$	1970°C (2243K)
TiO_2	1830°C (2103K)
Ti6Al4V	1630°C (1903K)
CPT	1570°C (1843K)
TCP	1391°C (1664K)
TTCP	1230°C (1503K)

5.3 Morphological Analysis

Having explored the chemical nature of coatings it is important to understand the way they are distributed on the surface. This is critical because biocompatibility depends not only on the chemical nature but also at what length scale they are distributed. Therefore extensive morphological analysis was done on the laser processed surface in the present study. Scanning electron imaging (SEM) of the laser processed samples was carried out. For simplicity selective images from 3 different speeds are presented in Figure 5.4. Figure 5.4(a) shows the morphology for 150 cm/min where the surface was highly porous and no complex multi-scale arrangement.

Figure 5.4 Different surface morphologies observed for various laser processing speeds [65].

However as the speed of laser processing increased (beyond 175 cm/min) a unique circular cellular ring patterns were detected on the surface as seen in Figures 5.4(b) and 5.4(c). These cellular features filled most of the laser processed area.

Detailed SEM analysis of the coatings processed at speeds 200 cm/min and above indicated the existence of cellular arrangement of cuboidal particles with star shaped particles dispersed inside the cellular patterns (Figures. 5.5). Typically these cellular rings shaped structures had diameters ranging from 2.5µm to 10µm.(Figure 5.5a). The star shaped particles had diameter around 1µm. The arms of these star shaped particles were around 200nm with arm spacing ranging from 50nm to 100nm (Figure 5.5b). The cuboids forming these cellular rings had dimensions of ~200nm x 1µm (Figure 5.5c). The porosity resulting from the distribution of these star shaped particles was around 1µm. The pores resulting from dispersion of these star shaped features, their arm spacing and cellular patterns resulted in a multi-scale variation ranging from nanoscale to microscale. At lower laser processing speeds these morphologies were observed on a limited scale. As discussed earlier such complex hierarchical morphologies are interesting from an osteointegration perspective.

Going forward the following sections will concentrate on detailed chemical, morphological analysis followed by exploration of the events leading to evolution of cuboids, star shaped features and possible dynamics behind their assembly. Elemental analysis (Figure 5.5d) of the star shaped particles showed that they were rich in Ti, O concentrations followed by Ca and limited or no P concentration. On the other hand, the ring of cellular feature was made of collection of cuboid particles which when analyzed showed higher presence of P in addition to Ca, Ti, O peaks (Figure 5.5e).

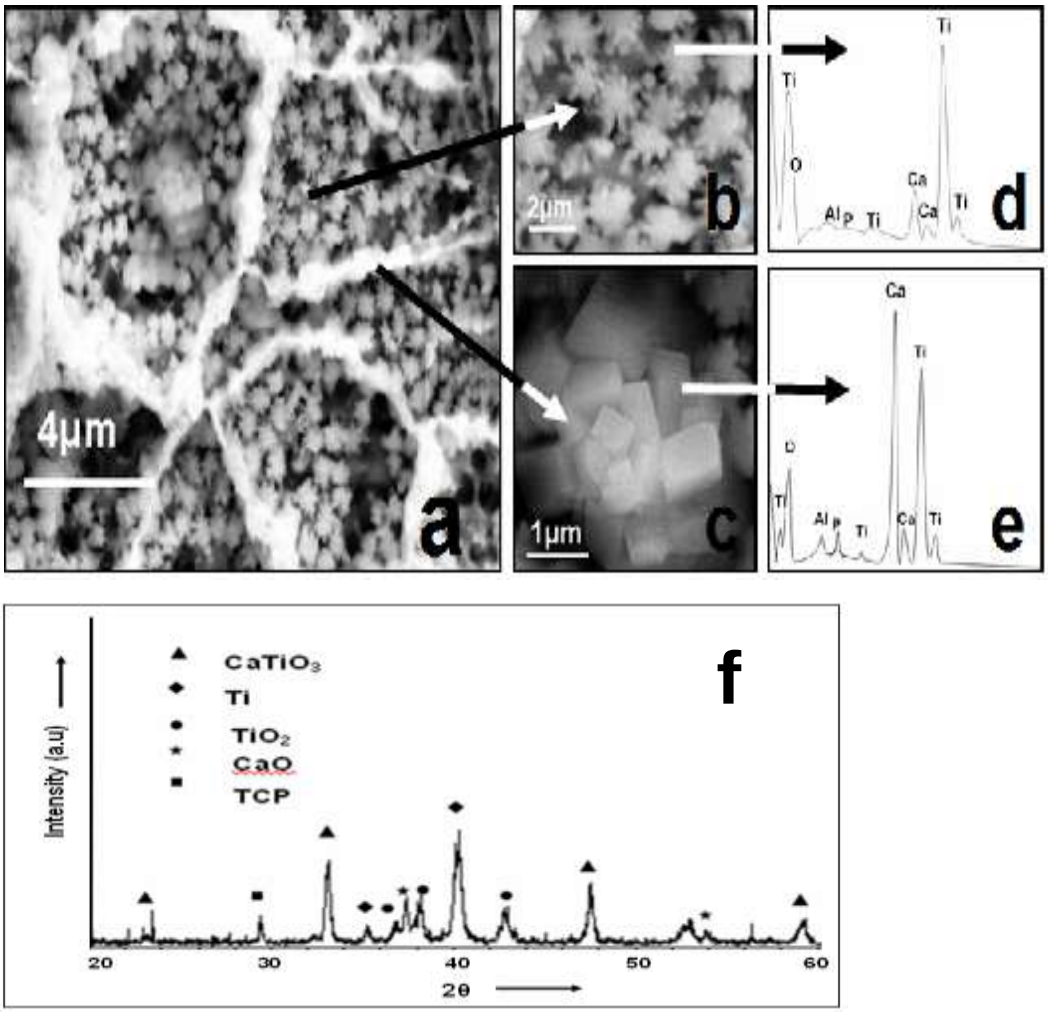

Figure 5.5 SEM –EDX analysis of a coating processed at 200cm/min. (a) Presents a low magnification image. (b) high magnification image of star shaped particles (c) high magnification of cuboids region. (d) EDX pattern of star shaped particle. (e) EDX pattern of the cuboid particles (f) XRD pattern of the sample for reference [64,66].

Coupling the XRD information of this coating with elemental analysis information from EDX will help in predicting the likely phases. In Figure 5.4f the XRD pattern indicated the presence of $CaTiO_3$, TiO_2, CaO, α-TCP (Tri Calcium Phosphate), along with Ti phase in the coating. The star shaped features due to deficiency of P could be $CaTiO_3$ particles. The cuboid particles making up the ring features were rich in P along with other chemical species suggesting the presence of CaP-TiO_2 phases.

Figure 5.6 provides interesting information. By imaging at different magnifications it was possible to appreciate the hierarchical evolution of this multiphase morphology. The figure vividly shows the arrangement of these multiple phases into multi scale textured assembly. The cellular features were organized at macro to microscale; the star shaped structures have evolved at micron scale while the cuboids that are arranged in cellular patterns are organized from micron to nanoscale. It is interesting to note that the multi scale texture also included nanoscale particles (labeled as 'C' in Figure 5.6). These fine particles could be the precursors for other phases observed in the coating.

Fractal analysis was carried out to better understand the surfaces post laser processing. Figure 5.7 compares typical fractal dimension calculated on laser processed samples. For simplicity the fractal dimensions recorded at multiple magnifications are presented for typical laser processing conditions of low (<175 cm/min), medium (200 cm/min) and high speeds (>275 cm/min). The average fractal dimensions are comparable but standard deviations are not. However this does not explain the role of length scale. To bring out the differences and understand the role of magnification the fractal dimensions are expressed with respect to magnification for various conditions

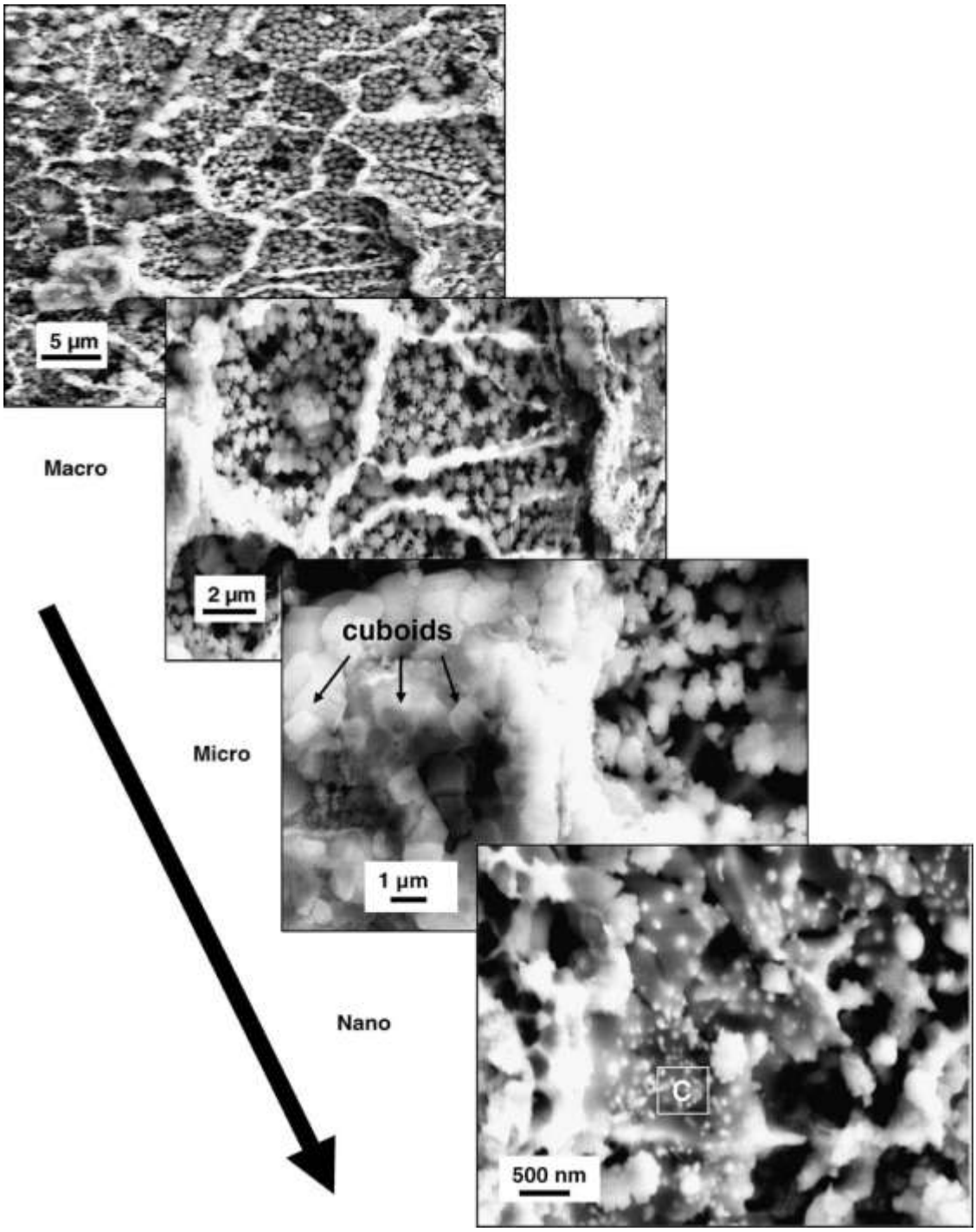

Figure 5.6 A multi-level structure revealed by imaging at scanning electron imaging at different magnifications [64].

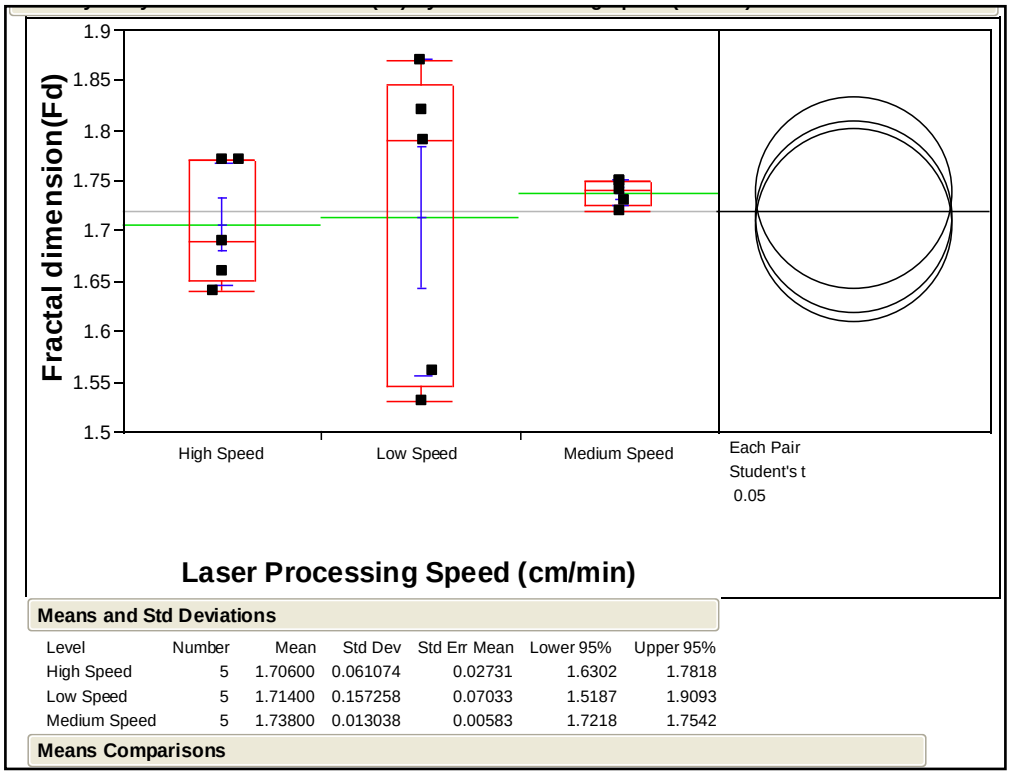

Figure 5.7 Fractal dimensions for various laser processing conditions.

Figure 5.8 presents this variation. As can be seen for medium processing conditions the fractal dimension values were consistent across multiple length scales. This suggests that surfaces are multi-scale and similar to features seen in natural environments. In comparison low and high speed laser processing conditions appear to be muti-scale over fewer length scales. The regions where there is no line tells us the fractal dimension values were not consistent in that range. The explanation for the fractal nature has got to do with the texture that the samples exhibit post laser processing. A lower processing speed resulted primarily in porous surfaces with no ring shaped arrangement of cuboid features and star shape particles inside. On the other hand faster laser processing conditions had an overlap of regions that a mix of reacted and un-reacted regions leading to the scatter in the data points. This could be because of the extremely high thermal gradients for faster speeds associated with these conditions the details of which will be covered in the later sections.

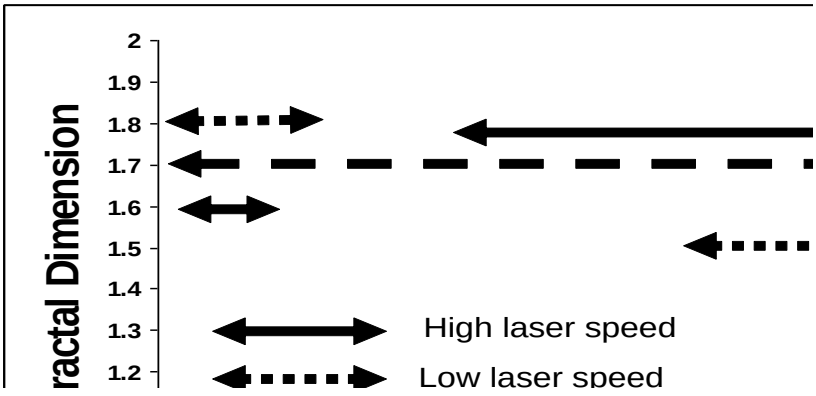

Figure 5.8 Regions of consistent fractal dimension depicted for various length scales for multiple laser processing speeds.

Detailed SEM analysis revealed the porous nature of the laser processed surfaces. Such features are extremely interesting from biocompatibility perspective. Figure 5.9 show typical porous surfaces observed for multiple laser processed surfaces. The nature of porosity varied with processing speeds. At low speeds (Figure 5.9a) the surfaces appeared highly porous although at one length scale. Figure 5.9b shows the multi-scale porosity observed due to the presence of the star shaped $CaTiO_3$ features.

The distribution of the star shaped particles; the arm spacing's of these particles provide multiscale pore features in the nanoscale to submicron scale (50nm-500nm). Moreover star shaped features tend to coalesce in few areas resulting in spherical voids at micron scale (0.5µ-1.5 µm). Figure 5.10 presents typical pore size distributions for 125 cm/min and 250 cm/min. From Figure 5.10 it is appears that lower processing speeds (125cm/min) presents a normalized pore size distribution centered roughly on 0.7µm. This is characteristic of a uniformly reacted surface that had been exposed to high temperature for prolonged period of time. In contrast at 250 cm/min the pore distribution is less normalized and closer to a biomodal distribution with critical densities centered around 0.1µm and 0.7µm. This could be attributed to the multi-scale features present in the coatings: mostly from the $CaTiO_3$ particles and their unique features discussed earlier. Typically, these features had arms around 0.1µm and their spacing's around 50nm. When these star shaped features come close and coalesce they end up as circular pores with typical diameters centered arround 0.7µm. The transitions from stars to circular pores correspond to the intermediate pore diameters observed in the Figure 5.10b. Having identified the multi-phases and their hierarchical arrangement it would be interesting to explore the thermodynamic and physical metallurgical phenomena that assisted their formation. The following sections will discuss these aspects

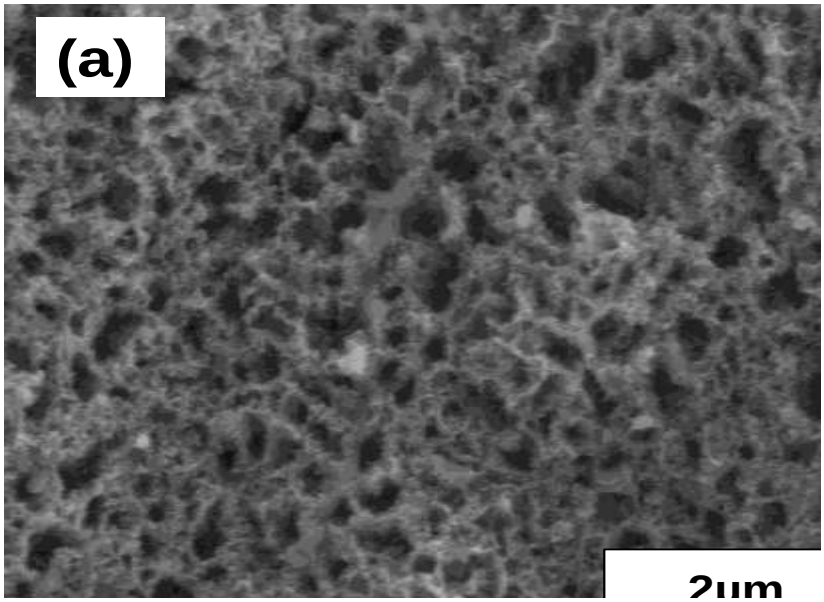

Figure 5.9 Porous nature of the coatings shown for samples laser processed at (a) 125cm/min (b) 250 cm/min.

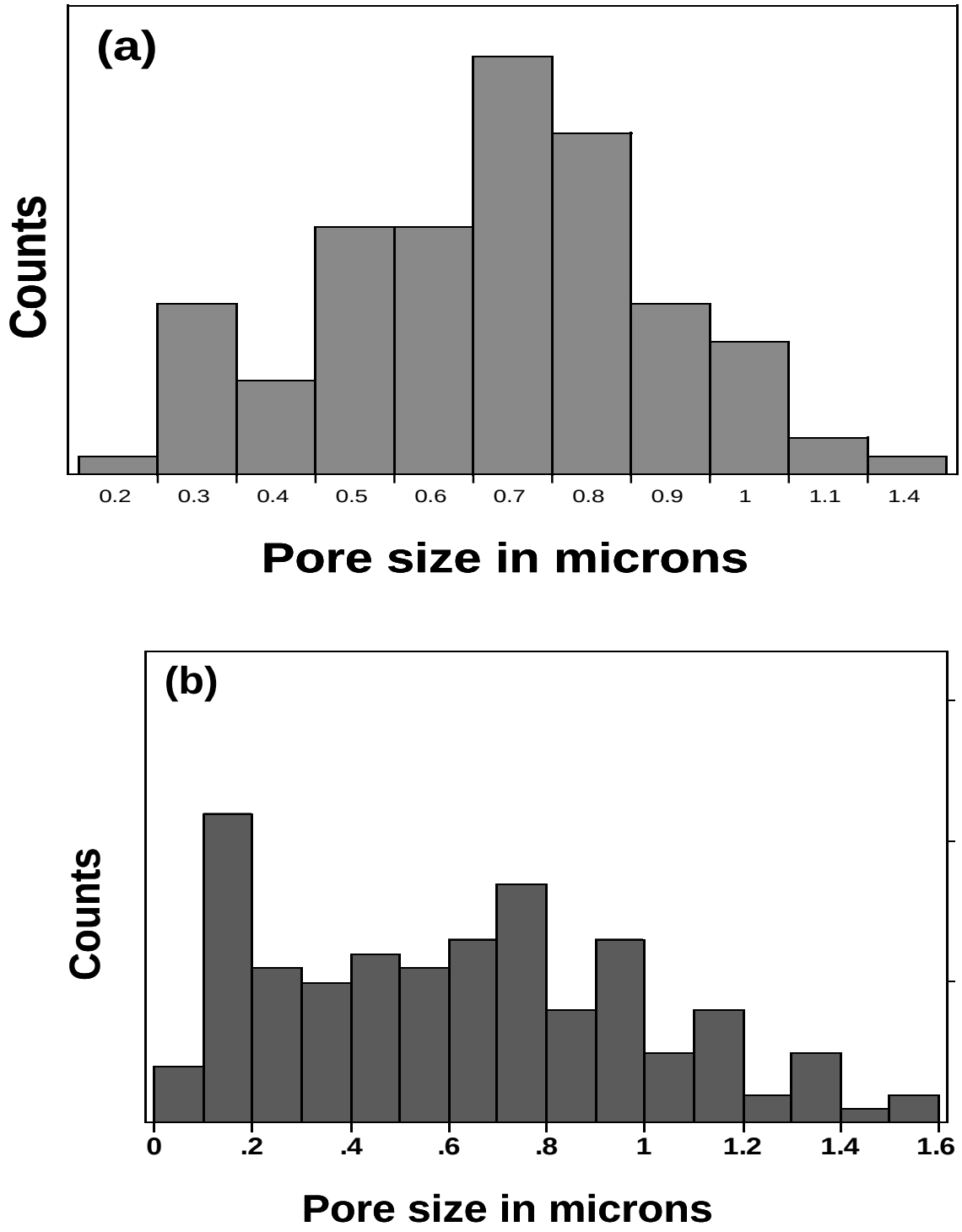

Figure 5.10 Pore distribution for typical laser processed surfaces at (a) 125 cm/min (b) 250 cm/min.

5.4 Thermodynamics of Transformation

During laser processing the temperatures in the precoated calcium phosphate tribasic salts (CPT) rise. This results in its dissociation into CaO and P_2O_5 which eventually vaporize at temperatures above 3123K and 3500K respectively [74]. Figure 5.11 depicts a computed temperature profile of a composite system consisting of CPT precoat on a Ti-6Al-4V substrate during the laser processing operation at a speed of 125 cm/min. The data points are computed using COMSOL's **™** heat transfer model discussed earlier in experimental section. Each curve in the plot represents a temperature profile at a particular speed for a particular track. Such calculations were performed for all the experimental laser processing conditions. However in the present documentation only select three cases corresponding to low (125 cm/min), medium (200 cm/min) and high (275 cm/min) laser processing speeds are presented. For simplicity only the temperature profiles representing the first (1st), middle (6^{th}) and final (11^{th}) track are presented. The details of the tracks are already presented in the experimental section (refer to Figure 3.3). Figure 5.12 and 5.13 show the temperature fluctuation with time for laser processing speeds of 200cm/min and 275 cm/min respectively. Considering Figure 5.12 the peak temperature reached for the first track is around 2000K. Moving to track 6 due to preheating effects of previous laid tracks the peak temperature rises to 2800K and in the 11 track (the last processed track for a coupon) the peak temperatures go to as high as 3500K. In addition, the temperature curves provide wealth of information about the cooling rates across critical temperature regimes that influence the final chemistry and final morphology. The trend discussed here is consistent for all laser speeds however the peak temperatures and cooling rates predicted are different, thus influencing the final coating morphology and chemistry.

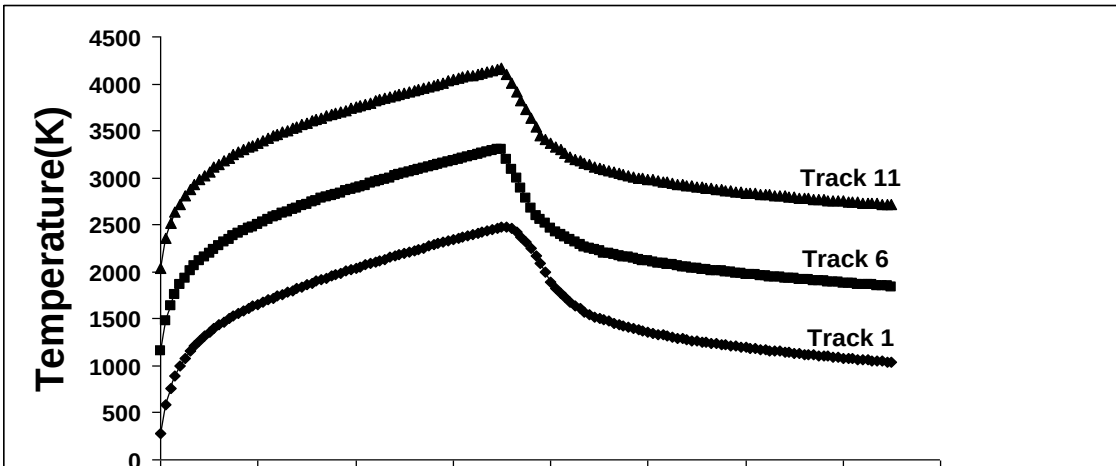

Figure 5.11 Temperatures for tracks 1, 6 and 11 when laser processed at 125 cm/min.

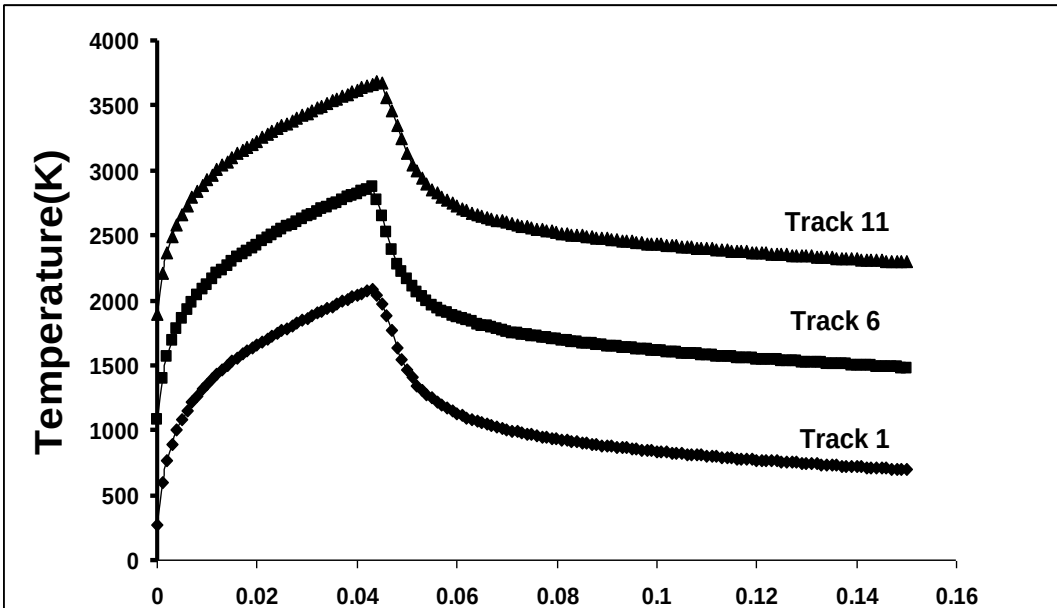

Figure 5.12 Temperatures for tracks 1, 6 and 11 when laser processed at 200 cm/min.

Figure 5.13 Temperatures for tracks 1, 6 and 11 when laser processed at 275 cm/min.

.Figure 5.14 is an over laid plot of temperatures obtained from different processing speeds and laser tracks. Faster laser processing speeds resulted in higher peak temperatures for any track compared to slower speeds. The maximum cooling rate regimes also vary for various laser processing speeds. For any speed when the peak temperatures for tracks 6 to 11 touch 3000K and above there is an evaporative loss of P_2O_5 and CaO constituents from the coating. Thus slower processing speeds have a greater exposure to such temperatures and evaporative losses. In general during the cooling cycle the residual CaO interacts with the TiO_2 in the molten pool to form $CaTiO_3$. TiO_2 comes from the oxidative reaction of Ti-6Al-4V substrate during high temperature laser processing. The various chemical reactions that occur at these high temperatures are already discussed earlier (refer to equations 5.1-5.5). Understanding the significance of these reactions with cooling rates will provide valuable information.

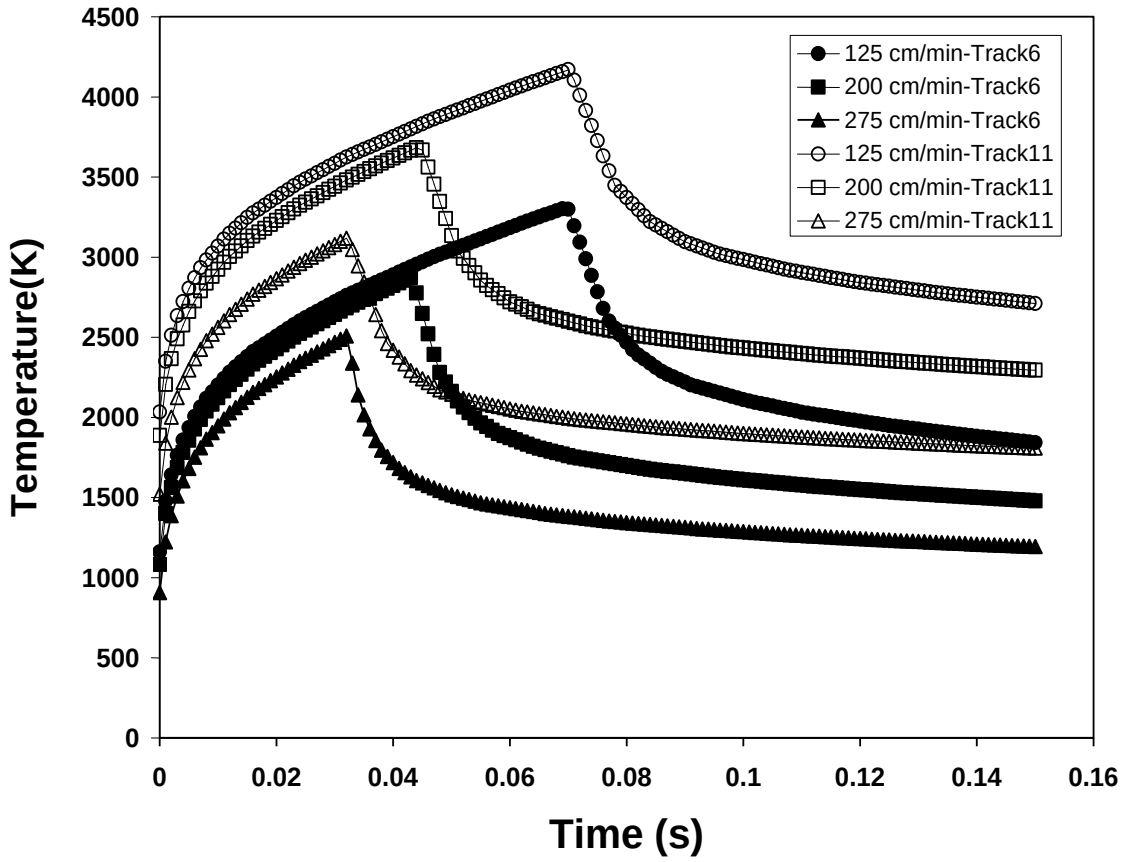

Figure 5.14 Temperature profiles for 3 different speeds (125 cm/min, 200 cm/min and 275 cm/min) at different 2 different tracks (6th and 11th) [66].

To better understand the CaO-TiO_2 interactions at different temperatures a binary phase diagram is presented in Figure 5.15 [66,90]. From the phase diagram the possible phases that can be present at room temperature are CaO, $Ca_3Ti_2O_7$, $CaTiO_3$, and TiO_2 [90, 91]. Since in the present work, $Ca_3Ti_2O_7$ was not detected in the XRD patterns (Figure. 5.1 and 5.2) it can be predicted that interactions occurred via eutectic solidification of $CaTiO_3$ concentrated in the region between 58 wt% TiO_2 (42 wt% CaO) and 100 wt% TiO_2 of the phase diagram.

For laser processing speeds (>250 cm/min) the peak temperatures barely reached 3000K by the end of processing (from eleventh track in the temperature plot calculations) and likely to have limited evaporative losses of dissociation products of CPT (CaO and P_2O_5) (Figure 5.13) For processing speeds >200 cm/min pronounced $CaTiO_3$ peaks in the XRD patterns suggests the good interactions between CaO, one of the dissociation products of CPT, and TiO_2 from the substrate. Exposure to lower temperatures during faster laser processing speeds seems to have limited decomposition of CPT as evident in the presence of stronger X-ray peaks of TCP at faster processing speeds (Figure. 5.2).

5.5 Kinetics of Transformation

Peak temperatures discussed in earlier sections will not alone explain for the complex chemical and morphological evolution in the coatings. Cooling rates are to be explored in parallel. With reference to the CaP-TiO_2 system few critical temperature regimes are to be considered. The various chemical phases seen in the XRD patterns are to considered while looking into the phase diagram Then the cooling rates across critical temperature regimes are to be considered.

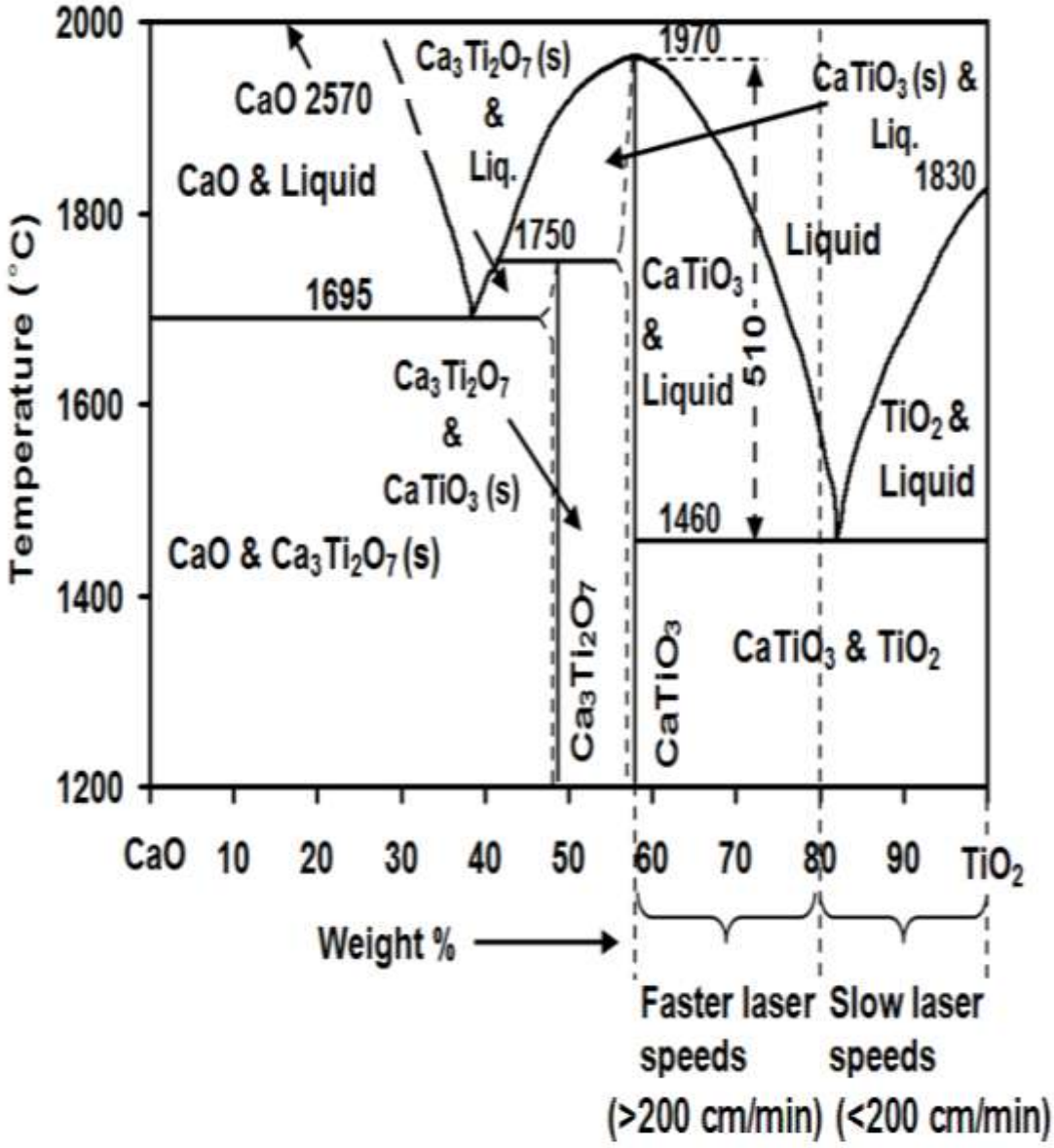

Figure 5.15 Identifying domains in the phase diagram of CaO-TiO2 system relevant to fast and slower laser processing conditions [66].

This is done by revisiting the heating and cooling cycle associated with various laser tracks laid with laser processing speed of 200 cm/min as shown in Figure. 5.16. In the figure, the insets provide the description of critical phase transformations occurring at various temperature regions across various laser tracks. Range 1 refers to the temperatures above 3000K while Range 2 refers to the temperatures in the 1500-2500K. From reactions perspective, Range 1 is primarily a region for vaporization of CPT phases (CaO and P_2O_5) while Range 2 is the regime where TiO_2 and CaO interact to form $CaTiO_3$ over wide range of temperatures. In this Range 2 regime, the eutectic reaction occurs with ~84 wt% TiO_2- 16 wt% CaO composition at 1733K (Figure. 5.15). Also in this regime the solidification of Ti-6Al-4V starts at 1903K. CaP rich phases like TCP are the ones that solidify last in this regime. In other words, until the temperature drops to 1500K these CaP rich phases remain in liquid form.

For a given traverse speed during laser processing thermal gradient varies in different temperature regimes: Higher temperature gradients exist at high temperatures and lower temperature gradients are evolved as temperature drops down (Figure 5.16). For example in the case of laser processing at 200 cm/min from (Figure. 5.16) for track 6 it can be seen that the temperatures drop steeply from 2800 to 2000K (the average cooling rate is $8x10^5$ K/s) followed by a gradual drop from 2000 to 1500K (the average cooling rate $5x10^3$K/s). As the temperature of the coating decreases so does the rate of cooling. Similar observations are made from the computations for tracks 6 and 11 in other processing speeds (Figure 5.11 and 5.13). In general, considering temperature in track 6 as an estimate of average temperature of the surface it is interesting to note that the gradual cooling rate across the range of temperatures in Range 2 (2500K to 1500K) provides sufficient time for separation and/or interaction of phases in this temperature window.

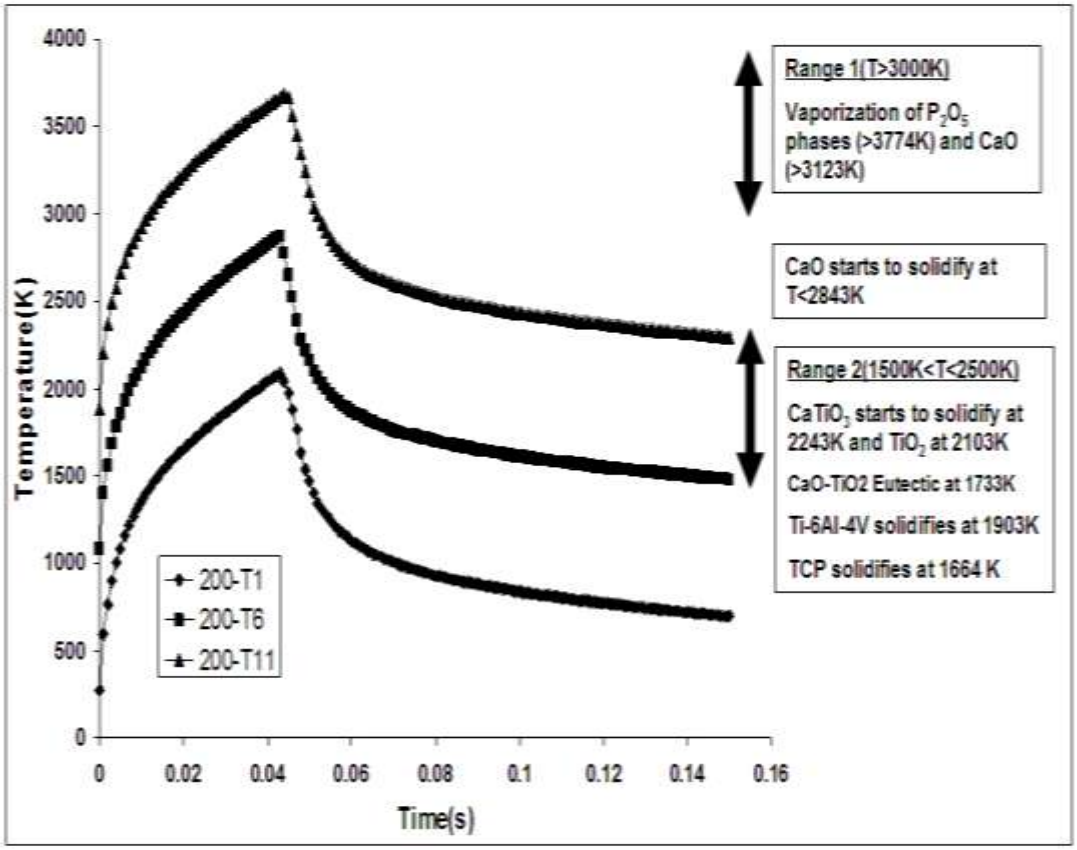

Figure 5.16 Temperature calculations for coatings processed at 200 cm/min with overlay of boxes identifying key phase transformations [66].

Another interesting fact is that in the CaO-TiO_2 phase diagram (Figure 5.15) there exists a steep slope for the liquidus during $CaTiO_3$ solidification. The separation between the liquidus and solidus temperatures increases with decreasing concentrations of TiO_2 from 80% wt. to 60% wt. indicating there is a wider temperature window (as high as 510^0C at around 60 wt% TiO_2) across which the structure remains fluid for longer time prior to complete solidification. This information is critical in understanding the evolution of phase morphology as function of cooling rate associated with the given processing speed. Another interesting observation is the nature of TiO_2 and CaO phases present in the final coating. For this refer to Figure 5.17, where the XRD pattern for samples laser processed at 150 cm/min and 250 cm/min are magnified between 30^0 and 50^0 of 2θ. These two speeds correspond to high and low speed regimes of the experimental conditions employed in the present work. TiO_2 is predominantly observed as anatase for higher processing speeds. Anatase transforms to rutile below 873K via an interface nucleation [92]. However in the present study the higher thermal gradients froze the metastable anatase phase for faster laser processing speeds. For speeds above 200 cm/min the TiO_2 peak corresponding to (004) at 38^0 has shifted to the left. The anatase peaks corresponding to (103) were also present at higher laser processing speeds. The broadness associated with this anatase peak appears as a shoulder on the left to CaO peak at $37^{o.}$ In general, the broadness and shift associated with the TiO_2 peaks on both sides of the CaO peak at higher speed indicate a possibility of a glass formation. The broad alpha-TCP peak at 35^0 having CaO and P_2O_5 constituents suggests a coexistence of glass formation chemistries when associated with TiO_2 from substrate. Comparatively, the TCP content was seen on limited scale at lower processing speeds.

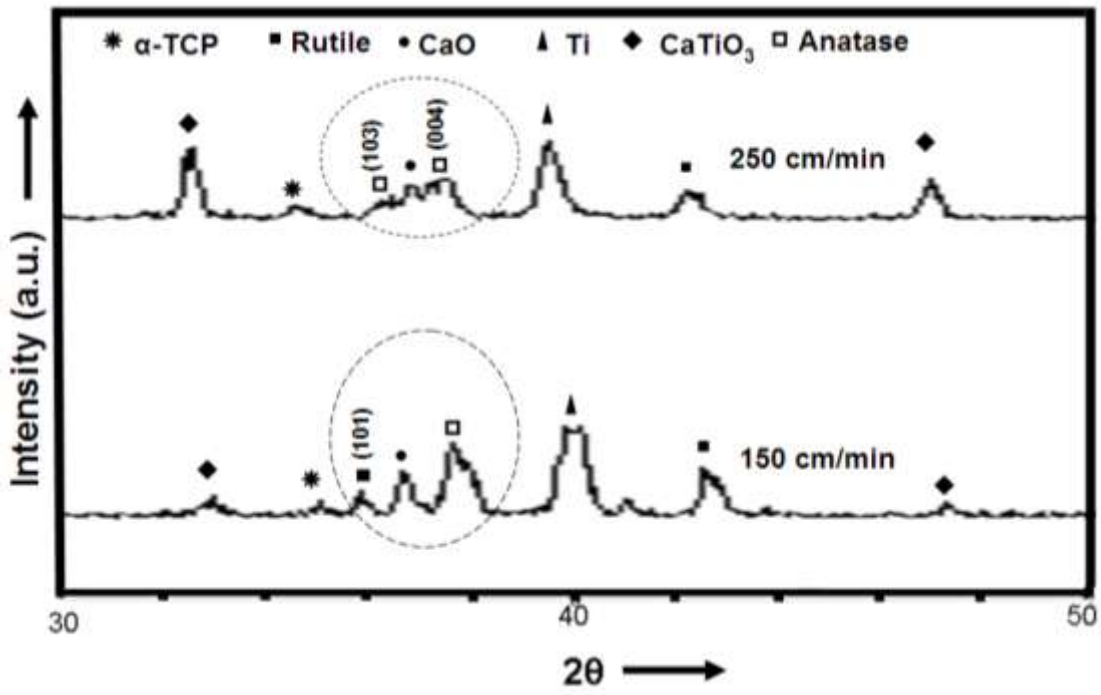

Figure 5.17 XRD patterns for low (150cm/min) and high (250cm/min) laser speeds [66].

It is interesting to note that under suitable thermodynamic conditions P_2O_5 acts as network former, TiO_2 acts as a network modifier by providing the extra oxygen atoms that bridge the network while CaO acts as modifiers to the glass network [93]. The broadness in the XRD peaks for various phases discussed in this section can be attributed to their possible glass formation tendencies in the final coating.

5.6 Microstructural Evolution

Understanding the microstructural features and their evolution is critical because it offers an opportunity to first identify the nature of multi-scale organization present in the coating and then correlate the evolutions of these features with knowledge of laser induced temperature variations

explored earlier. Previously it was shown from scanning electron microscopic imaging that the coating consisted of a cellular arrangement of cuboidal particles with star shaped particles dispersed inside these cellular pattern (Figure 5.5). Coupling the XRD analysis of the coatings with elemental analysis (EDX) done on specific features in the microstructure it was inferred that these cuboids are calcium phosphate-TiO_2 (CaP-TiO_2) rich particles and the star shaped particles are $CaTiO_3$. A low magnification view of such uniquely textured coatings and their corresponding 3D surface projection are presented in Figures. 5.18. Careful removal of the coating at specific locations followed by scanning electron imaging revealed an equiaxed faceted grain structure of the underneath Ti6Al4V substrate (Figure 5.18c). The 3D surface projection of this underneath substrate is presented in Figure 5.18d.

This observation corroborates with earlier observation of CaP-TiO_2 rich phases forming a cellular ring like structure around star shaped $CaTiO_3$ and TiO_2 features. This cellular and star shaped arrangement is seen clearly at speeds greater than 200 cm/min. This was observed on limited scale for coatings processed at lower laser processing speeds. It is believed that this hierarchically evolved morphology is desired from an osteointegration perspective. Hence, going forward the following sections in this work will focus on the evolution of cuboids and star structures and possible dynamics behind their assembly.

5.6.1 Dynamics of Particulate Formation

Chemical inhomogeneity and/or surface roughness at site specific locations on a particle in a fluidic interface could result in irregular or undulated contact line. These undulations, when overlapped result in change in the surrounding liquid interfaces inducing capillary interactions.

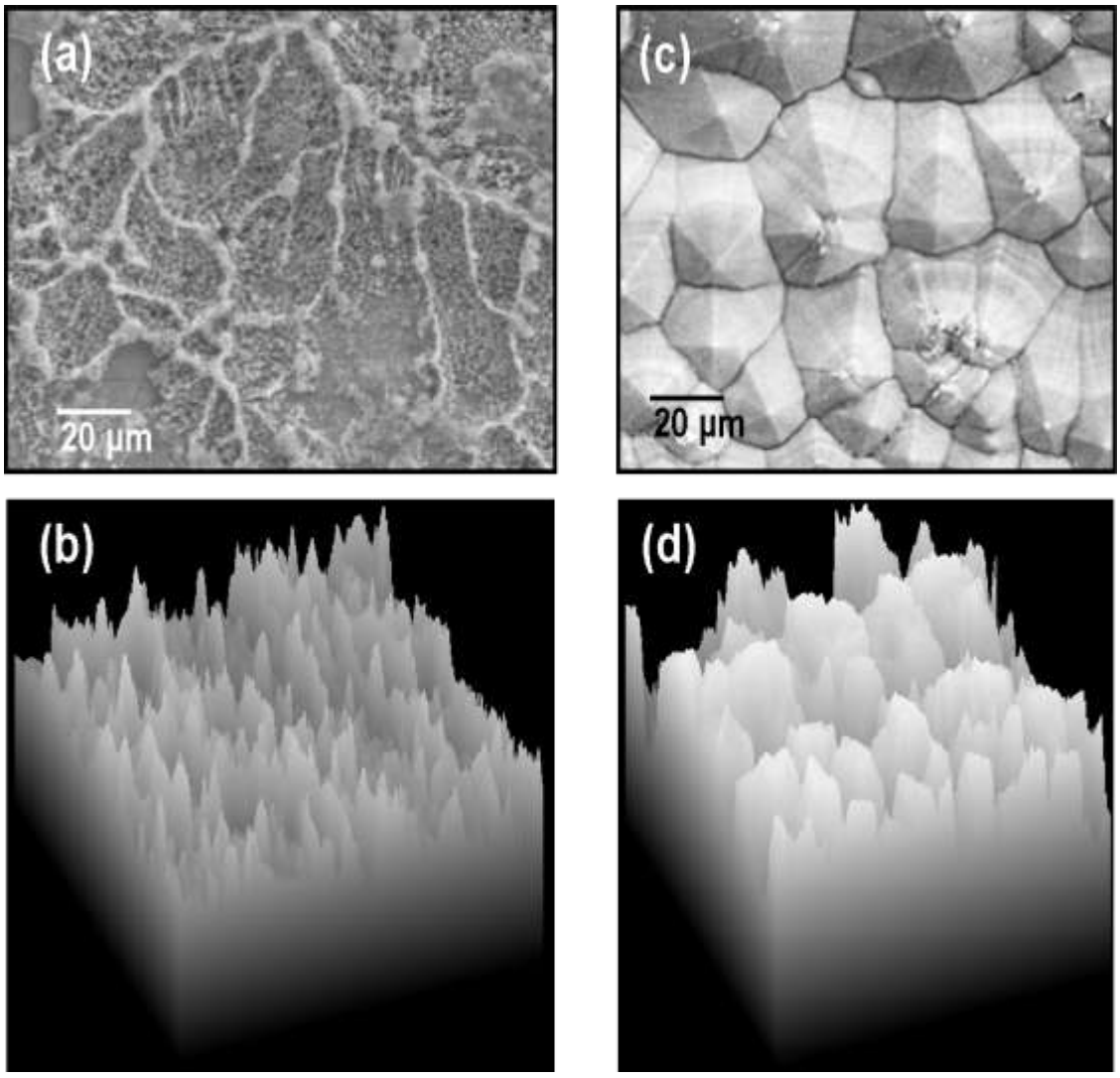

Figure 5.18 (a) Low magnification SEM image of a laser processed coating (b) Simulated 3D surface profile of the coating surface (c) SEM image of the underneath substrate after removing the coating (d) 3D surface profile of the underneath substrate [66].

Such surface deviations on neighboring particles, either concave or convex from planarity are considered as positive or negative charges [94,95]. Such interaction can either be flotation or immersion in nature. These perturbations in the shape of the liquid due to two such particles could result in lateral capillary forces which could be either immersion or flotation [96]. In general, the interaction for charges is isotropic while for multipoles the interaction sign and magnitude are influenced by mutual orientation of particles.

In the present case, in the molten pool during early part of laser processing any TiO_2 particle with area covered by CaP chemistry will have one type of charge/wettability characteristics as opposed to the other locations (CaP has different wettability compared to TiO_2). With respect to the liquid, such variation in charge (as a result of wettability variation) results in formation of hydrophobic and hydrophilic interfaces on the same particle. Such particles are considered as multipoles (m) and the charge distribution on them makes them dipole (m = 1), quadrupoles (m = 2), hexapoles (m = 3), etc. It is believed that the CaP rich TiO_2 particles discussed as cuboids in SEM and EDX (Figure 5.4) analysis could be a result of self assembly. These cuboids shaped particles are consistent in size (typically 200 nm x 1 μm). Due to the specific size and shape associated with these CaP rich TiO_2 cuboids, the underlying sub particles that are self assembled are suspected to be quadrupolar [95,96]. The explanation for their formation is as follows. Due to the angular dependence of the immersion forces it is difficult for a system that contains different multipole orders (m = 1, 2, 3, etc) to form ordered 2D crystals. In the present study, since CaO-TiO_2 cuboids of specific size were observed, the assembly is believed to be built with particles having the same multipolarity. Furthermore, due to the cuboid shape of these particles (Figure. 5.4) built on 2D square shaped framework, it is speculated that the immersion forces must have predominantly acted between particles that are

quadrupolar (m = 2) in nature as illustrated in Figure 5.19. According to Kralchevsky et al., for multipolar particles, mutual orientation will influence the magnitude and sign of the capillary force [94-96]. Therefore, hexagonal lattice will be formed for hexapoles (m = 3) while square shaped lattice is preferable for quadrupoles (m = 2). Fourier et al. have determined the interaction energy for all possible configurations of quadrupoles and reported that square alignment would result in the most stable ground state condition [97].

5.6.2 Energy of Interaction between Particles

Having explored the nature of multipoles, it is important to comprehend the possibility of their interactions for self assembly from a thermodynamic perspective. The following section presents the feasibility of such formations based on theoretical calculation at various length scales

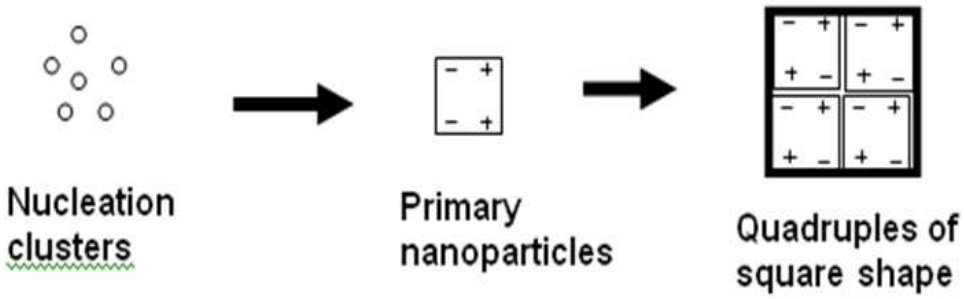

Figure 5.19 Schematic showing the quadrapular assembly of CaO-TiO2 particles at fundamental scale [64].

Figure 5.20 presents a schematic representation of contact lines between two capillary multipoles. For the present case shown in Figure 5.20, the theoretical interaction energy between two capillary quadrupoles is given by the following equation [94-97].

$$\Delta W(L) = -12\Pi\sigma H^2 \cos(2\varphi_A + 2\varphi_B)\frac{r_c^4}{L^4} \qquad (5.6)$$

(Where m = 2; L >> $2r_c$)

In the above equation, H represents undulation in the contact line, r_c represents average undulations, L represents the distance between two particles, φ_A and φ_B represents the angles subtended between diagonals for each qaudrupole and σ represents the interfacial tension. The equation can be simplified for two quadrupoles in contact as shown below. Considering an interfacial tension of 250 mN/m for CaO-P_2O_5 at 1673K the interaction energy exceeds thermal energy (kT) for fluctuations of amplitude as small as 2 angstroms [98].

$$dW = -(3/4)\,\pi\,\sigma\,H^2 \qquad (5.7)$$

Where (r_c /L) = 0.5 and cos ($\varphi_A + \varphi_B$) =1 [when they rotate spontaneously]

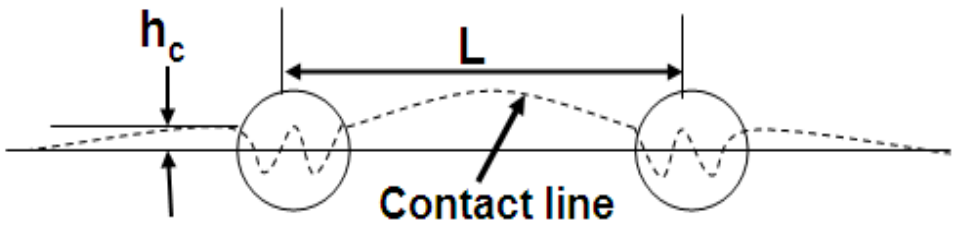

Figure 5.20 Schematic of two capillary particles separated by a distance 'L' [66].

In other words, for the present system capillary interactions between two quadrupole particles are considerable even for undulations as small as 2 angstroms. Kralchevsky et al. have reported that fluidic surface undulations at such small scale are hard to realize. They are typically over ridden by rough thermally excited fluctuation capillary waves usually in the 3-6 angstrom range [96].

Moving up the length scale, energy calculations were made by considering amplitudes in nanoscale range with undulations significantly larger than the background noises. Using an undulation (H) of 20 nm and considering σ = 250 mN/m and r_c/L = 0.3 the capillary interaction energy (dW) turns out to be 1.2 x 10^3 kT. Since the size of the cuboids was in the submicron range (>100nm) the underlying assembling particles are expected to be in nanoscale (<100nm) and therefore undulation (H=20 nm) was chosen in that length scale.

This significant capillary interaction energy values suggest higher tendency for self-assembly of sub-micron particles into two dimensional networks along the fluidic interface [96]. The assembly of these 2D particles forms the nucleus for eventual assembly into 3D cuboid structures. Fourier et al. have commented that a jammed system is formed when large numbers of such particles are attached to each other under such strong capillary conditions [97].

5.6.3 Macro and Microscale Assembly of Particles

From the microstructural observations self assembling has been realized at multiple length scales (Figure 5.5). In the previous section, energy calculations and self assembling concepts for cuboid particle formation at sub micron level under the action of immersion capillary forces have been explored.

The following section discusses their physical movement and orientation into ring like patterns at microscale under the influence of temperature and subsequent phase evolution during solidification. The convective particle flux results in drag forces (D_f) as the core cuboids grow in size and the surrounding liquid starts to evaporate. A phenomenon called hydrodynamic drag primarily influenced by evaporation of the liquid wetting film results in convective assembly that will result either in accumulation of these cuboids at the center or get dragged to periphery and pinned by local point of contacts. This is further enhanced by morphological changes due to multi-phase evolution as a result of solidification process during the cooling cycle post laser processing.

As described earlier, the observation of facet morphology and trough/crest formation in the underlying Ti-6Al-4V alloy during solidification (Figure 5.18c) forms the basis for this observation. A detailed sequential evolution of various phases during the cooling cycle is illustrated in Figure 5.21. The CaP phases owing to their low melting point (~1664K) solidify last. As a result, during solidification CaP phases mostly in liquid form move around the topographies created by already solidified $CaTiO_3$ from the top (Figure 5.18a) and Ti-6Al-4V from the bottom (Figure 5.18c). Some of the solidified TiO_2 particles floating in the CaP liquid are hydro dynamically dragged and finally get stuck irreversibly near the troughs during subsequent solidification process of the CaP liquid. This is further enhanced along the contact line in the trough by the pinning action typically associated with such particles. Typically, a contact line undergoes a sequence of depinning-pinning events with particles aggregating whenever the contact line is pinned. The pinned locations ensure the outermost boundaries of the cellular features and start to pull the other similar floating particles to its proximity. This would result in coarsening of the boundary network.

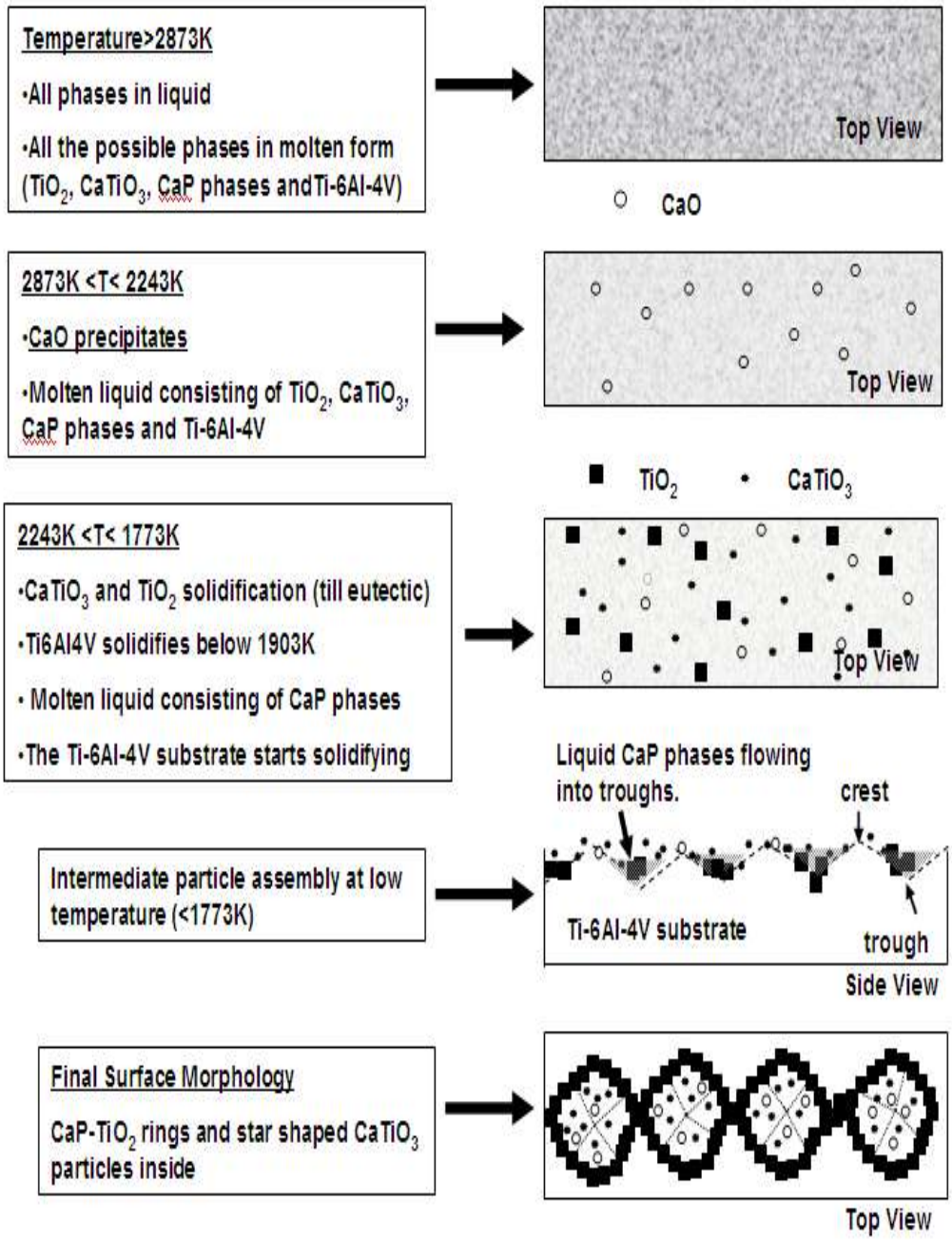

Figure 5.21 Morphological evolution of the coating with lowering temperatures during solidification [66].

Figure 5.22a shows how the cuboids typically get locked at contact points and agglomerate. Figure 5.22b shows the drag force (D_f) resulting in evaporative liquids pulling the particles towards the contact lines pinned down by normal force (N_f). This normal capillary force ensures the particles are irreversibly pinned to the substrate. These pinned locations act as focal points for further accumulation of particles during subsequent evaporation and hydrodynamic drag force exertion. For slower laser processing speeds where there are less CaP phases left on the surface only the Ti alloy solidified into a faceted morphology while for faster processing speeds the CaP phases (that underwent limited vaporization) oriented above the underlying faceted Ti alloy substrate morphology. The phenomenon of jamming or pinning usually affects glass forming systems which during sudden transition to amorphous phase exhibit a slowdown in their dynamics

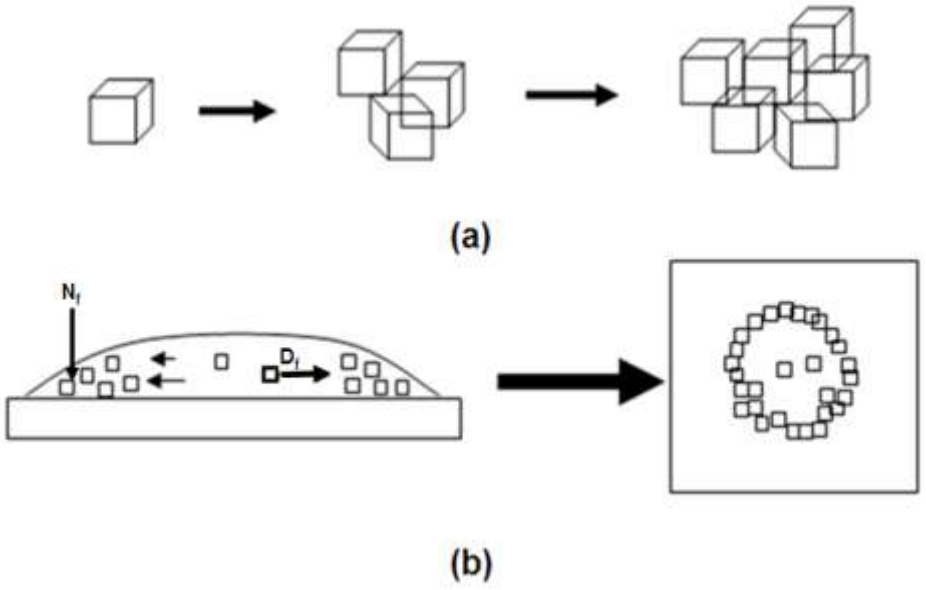

`

Figure 5.22 Schematic showing (a) pinning of particles along contact line and (b) hydrodynamic drag accumulation along the periphery of the contact line [64]

Thus pinned locations are created via vitrification during supercooling. Temperature is the critical parameter that controls this transformation. This transition creates geometrical constrains that result in accumulation of particles at these locations and restrict any other formation [99]. As discussed earlier, the present chemical system has glass forming tendency. Under favorable thermodynamic conditions it has been reported earlier that P_2O_5 acts as network former while TiO_2 and CaO act as network modifiers [93]. The resulting vitrification process during cooling would result in pinned locations where subsequent agglomeration of particles proceeds via hydrodynamic mechanism.

The final microstructures show the surfaces with CaP rich cuboids in a circular pattern arrangement with star shaped $CaTiO_3$ resulting from CaO-TiO_2 interaction distributed all around. Moreover as discussed earlier with reference to the CaO-TiO_2 phase diagram in the region where nucleation of $CaTiO_3$ taken place primarily towards the CaO rich section it was observed that there is a large temperature window across which particles can move freely before they finally solidify (Refer to Figure. 5.15 where a 500^0 C separation is seen between liquidus and solidus lines). This temperature window provides opportunity for particles to move around and time to settle during assembly. At faster laser processing speeds due to limited vaporization of CaP material (i.e. enough amount of retained CaP phases in the molten coating) and ideal thermal gradients in the 1500-2500K temperature window the particles have good possibility to orient and self assemble. The formation of this kind of hierarchically evolved assembly is very beneficial from a biocompatibility perspective. In the present research, it has been observed that there has been a multi-scale evolution of morphological features driven primarily by self assembly.

5.7 Biocompatibility of Coatings

Chemical and morphological analysis of the CaP coatings on Ti-6Al-4V alloy showed evidence of multi-scale arrangement for a multi-phase system. It would be interesting to see the biocompatibility aspects of these coating. The present section discusses results from experiments conducted to evaluate the performance of these coatings when exposed to simulated body fluids (SBF).

5.7.1 Wettability Studies

Wettability is a simple and easy parameter that determines the surface energy of a material. Surface energy dictates the nature of cell attachment and its proliferation. Surface components and surface chemistry are two critical components that define the wettability. Hence any surface engineering operation that involves changing surface chemistry and or morphology is tested for wettability. The final shape taken by a drop of liquid when brought in contact with a flat surface is expressed in terms of the contact angle ‘θ’ it subtends with the horizontal plane. Using the concept of virtual work Young’s equation relates this contact angle to liquid surface energy (γ_{lv}), solid surface energy (γ_{sv}), and solid–liquid interfacial energy (γ_{sl}) as shown below:

$$\cos\theta = \frac{\gamma_{sv} - \gamma_{sl}}{\gamma_{lv}} \qquad (5.8)$$

Surface chemistry and roughness also influence the surface energies and in turn the contacts angles observed. Therefore contact angle measurements were made for various laser processed samples are present in Figure 5.23. The hardness values are also overlaid in the plot. As can be seen from the figures with increasing laser processing speeds the roughness in general decreased suggesting generation of rougher surface at lower speeds. It has to be recollected that

there was marginal increase in the roughness for zirconia coatings on Ti alloy substrates as reported during pulsed laser processing. In the same fashion, the contact angle values decreased with increasing scanning speeds indicating better wettability of the surfaces for faster laser scanning speeds. The contact angle θ is related to the roughness factor, r_a by the following equation [100].This equation suggests an inverse relationship between contact angle and roughness factor. For good wettability θ needs to be small which results in higher cosθ and in turn higher r_a values suggesting rougher surfaces.

$$r_a \cdot (\gamma_{sv} - \gamma_{sl}) = \gamma_{lv} \cdot \cos\theta \qquad (5.9).$$

On the contrary in the current work the roughness values and contact angle measurements follow a direct proportionality (Figure 5.23). Therefore the surface energy components of the equation are expected to have significant impact on the contact angle (θ) values.

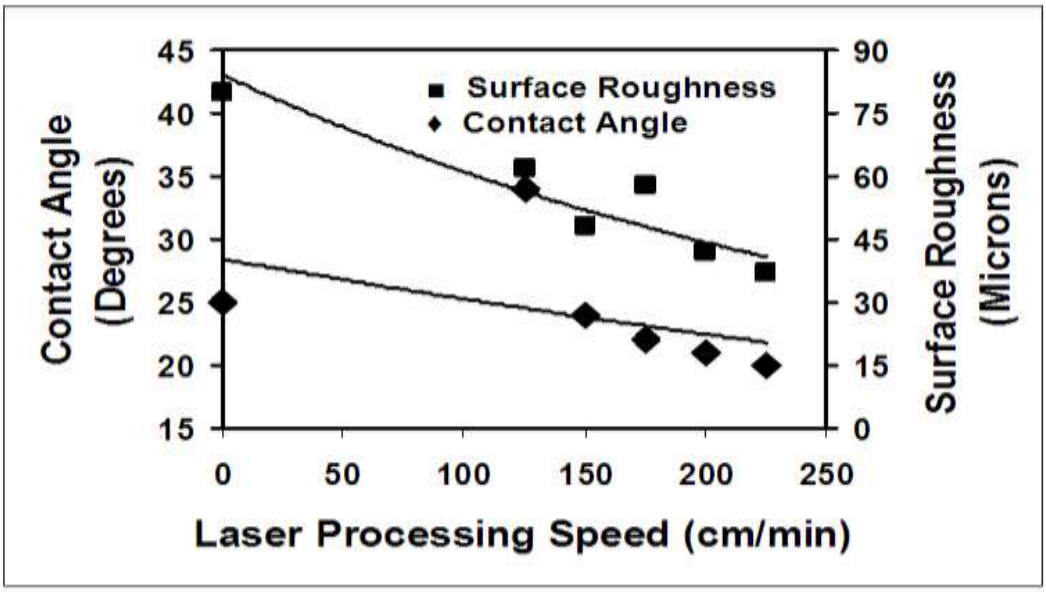

Figure 5.23 Change in contact angle and roughness values with laser processing speeds [65].

But determining the surface energy values of the laser processed surface is quite complicated. There are several important parameters such as oxygen content, chemical in-homogeneity due to multiple phases in addition to crystal shape and size. Cassie developed wettability equation analogues to Weznel by incorporating the role of surface chemical phases in a chemically heterogeneous surface as shown below: [101]

$$\cos\theta = f_1 \cos\theta_1 + f_2 \cos\theta_2 \qquad (5.10)$$

In the above equation, f_1 is the area fraction of phase 1 and θ_1 is the contact angle for a particular phase and likewise f_2 and θ_2 represent the area fraction and contact angle for the second phase in the composite coating surface.

As discussed earlier, for chemical analysis it is clear that the laser processed surfaces are multi-scale and multi phase providing a complicated scenario for identifying the effect of each of these constituents in the macroscopic wettability measurements. Looking back at the chemical analysis, specifically the XRD patterns in Figure 5.1 it can be seen that laser processing conditions have significant influence on the chemical phase composition of surface. The key phases present in all laser processed sample surfaces are $CaTiO_3$, TiO_2, and CaO along with Tri Calcium Phosphate (TCP) with varying degrees of concentrations. It is known that the wettability of a surface increases with amount of oxygen concentration in surface. In the present case, the presence of oxides and other phases are expected to influence the nature of wetting on the surface [100]. Considering the peak intensity values for various phases it is observed that with increasing laser processing speeds the amounts of $CaTiO_3$, CaO and TiO_2 increase as seen in Figure 5.3. Better wetting of the coatings processed at faster laser processing speeds can, therefore, be attributed to higher concentration of oxide based phases. Moreover, Agathopoulus

et al. have reported that binary oxide ceramic glassy phases aid wettability [102]. As discussed earlier, given the thermal gradients and the presence of chemical species like $CaO\text{-}TiO_2\text{-}P_2O_5$ it is not uncommon to expect glassy material formation **[**93,101,103]. Thus a greater probability that the glassy nature of the surface from faster laser speeds resulting in better wettability and lower contact angles. This is further exposed by the broadness associated with the XRD patterns for faster laser processing speeds suggesting amorphous constituents (refer to Figure 5.17).

However it has to be realized that regular contact angle measurement adopted in this study to determine wettability involved large liquid droplets. This size is large compared to size of the features that were characterized from chemical and physical perspective. This resulted in ambiguity while assessing the biocompatibility of surfaces via SBF wettability studies difficult. In addition, contact angles are determined on surfaces after interaction with the surfaces after first few seconds and not over a prolonged period of time. Therefore, immersion in simulated body fluids for prolonged period of time was considered more relevant and the results are presented in the following section.

5.7.2 Simulated Body Fluid Experiments

Simulated body fluid liquids closely represent the concentration of blood plasma. Ability of synthetic biomaterial surfaces to precipitate hydroxyapatite when exposed to this SBF solution provides a good in-vitro assessment of its biocompatibility. In experimental section the process for simulated body fluid preparation was described. The coatings immersed in this SBF solution are regularly monitored for chemical and morphological modifications. The morphology of the laser-coated surface after 14 days immersion in SBF is shown in Figure 5.24.

Elemental chemical analysis via EDX on the globular surface features clearly showed them rich in Ca and P indicating a possibility of apatite evolution. Figure 5.25 shows an overlay of XRD spectra from surfaces before and after SBF immersion. It can be observed that there is clear evolution of HA with dissolution of phases like CaO and recrystallization of hydroxyapatite from TCP during SBF immersion [104]. In order to appreciate the evolution on HA on the laser processed surface during SBF immersion, a study involving SEM was employed to regularly evaluate the morphology and its chemical nature. This was done by immersing the samples in SBF followed by electron microscopic imaging and chemical analysis. Following this procedure helped in understanding the role played by the ring shaped calcium phosphate cuboids and the star shaped calcium titanate networks.

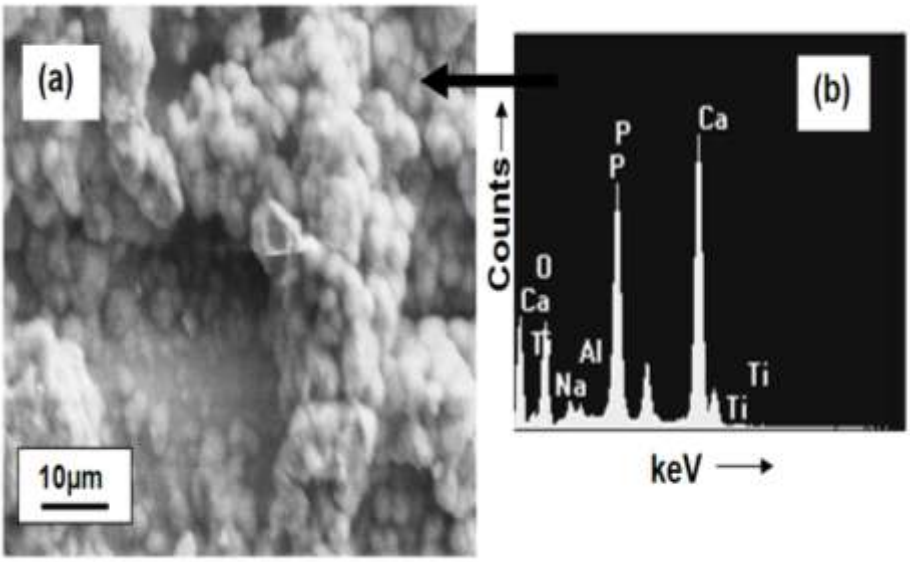

Figure 5.24 (a) Morphology and (b) chemical analysis of laser processed sample after 14 days SBF exposure [62]

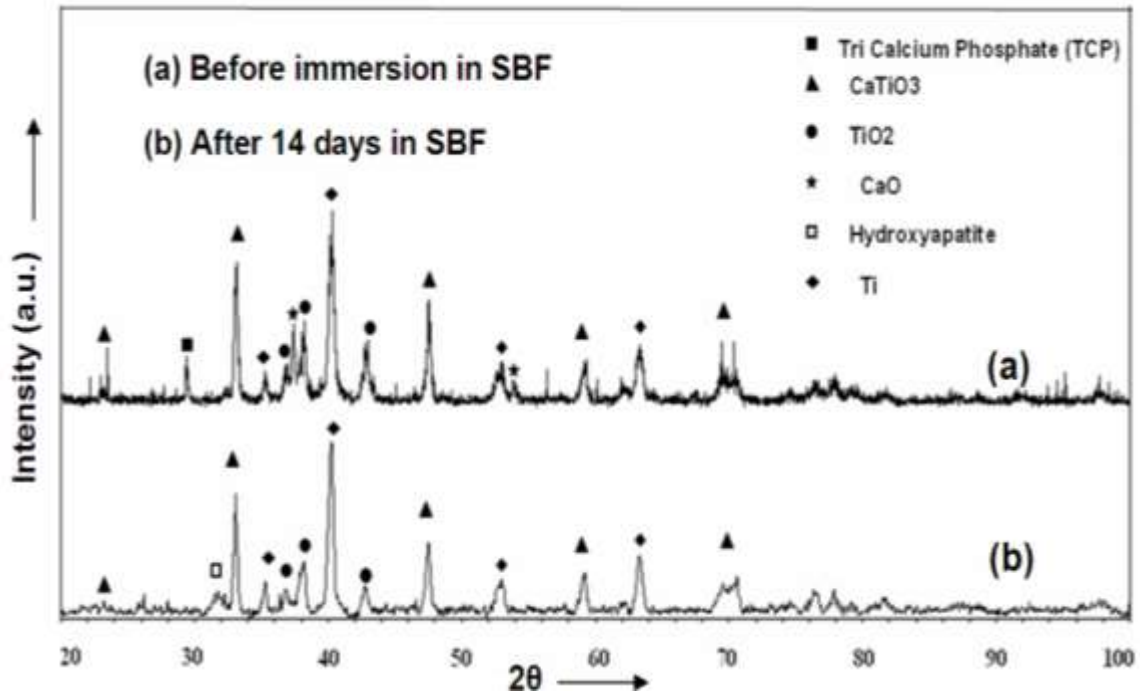

Figure 5.25 XRD patterns of coatings (a) before immersion in SBF and (b) after immersion in SBF [64].

Figure 5.26 provides a sequential pictorial description of the events. After two days the evolution of the networks becomes visible following dissolution of CaO. After 3 days of immersion, the network is far clearer with hydroxyapatite precipitation along networks and on star shaped particles (that appear like dots inside the circular networks). As days progress the thickness of the networks widens so are the precipitates on star shaped particles. Eventually the precipitation completely blankets the morphology. underneath. This observation suggested that presence of CaP-TiO_2 along with $CaTiO_3$ served as the nuclei for controlled precipitation of HA as shown in Figure 5.26d. This reinforces the fact that the multi-scale textured surface could provide early access points for early HA precipitation and improved biocompatibility. The quick dissolution of CaO was not surprising and falls is in line with existing literature published [105].

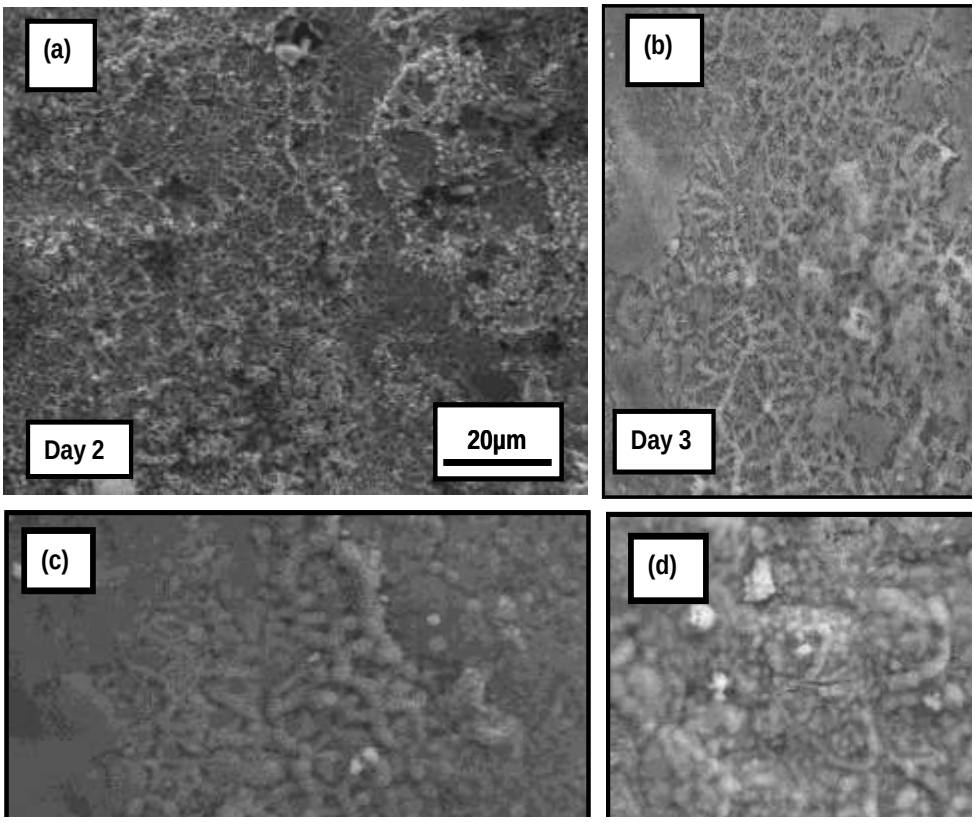

Figure 5.26 Sequential evolution of morphology during immersion in SBF. (a) Sharper features evolution following dissolution of CaO related phases (b) Day 3, the cellular structure clearly evolved after dissolution of the CaO from the surface. Note that the $CaTiO_3$ rich star like structures exist inside each of these cellular structures (c) After Day 4, the cellular structure coarsens with the precipitation of HA (d) Nucleation and precipitation of HA takes place clearly all along the cellular network and on the $CaTiO_3$ rich star shaped particles inside these cellular structures [62]

It is reported in literature that among hydroxyapatite decomposition products the order of dissolution decreases from CaO to tetra TCP, and further to TCP [105]. In the present work, immediate dissolution of CaO was observed as evident from the absence of the peaks corresponding to CaO in Figure 5.27 where the XRD pattern from a sample rinsed in water is compared to as received laser processed condition.

5.7.2.1 Fractal Dimension in SBF

Fractal dimensional analysis during the morphological evolution of hydroxyapatite when exposed to the simulated body fluids on the laser coated surfaces provides interesting understanding. Figure 5.28 presents the variation in fractal dimension with exposure time in days. These fractal dimensions were calculated from scanning electron images captures from a sample laser processed at 250 cm/min exposed to simulated body fluid.

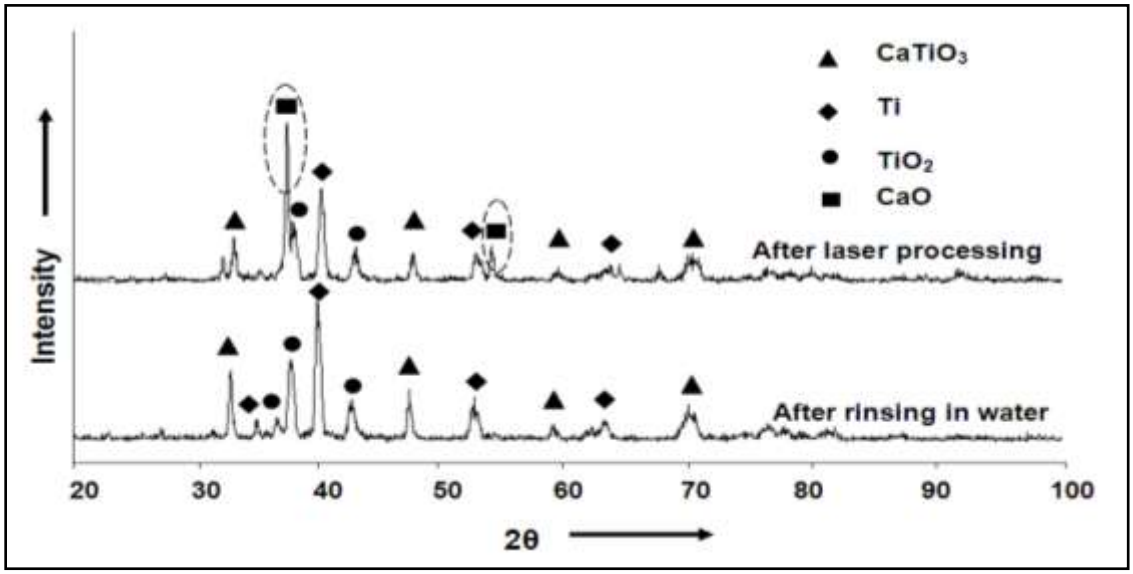

Figure 5.27 XRD patterns showing the dissolution of CaO from coatings via water rinsing process [62].

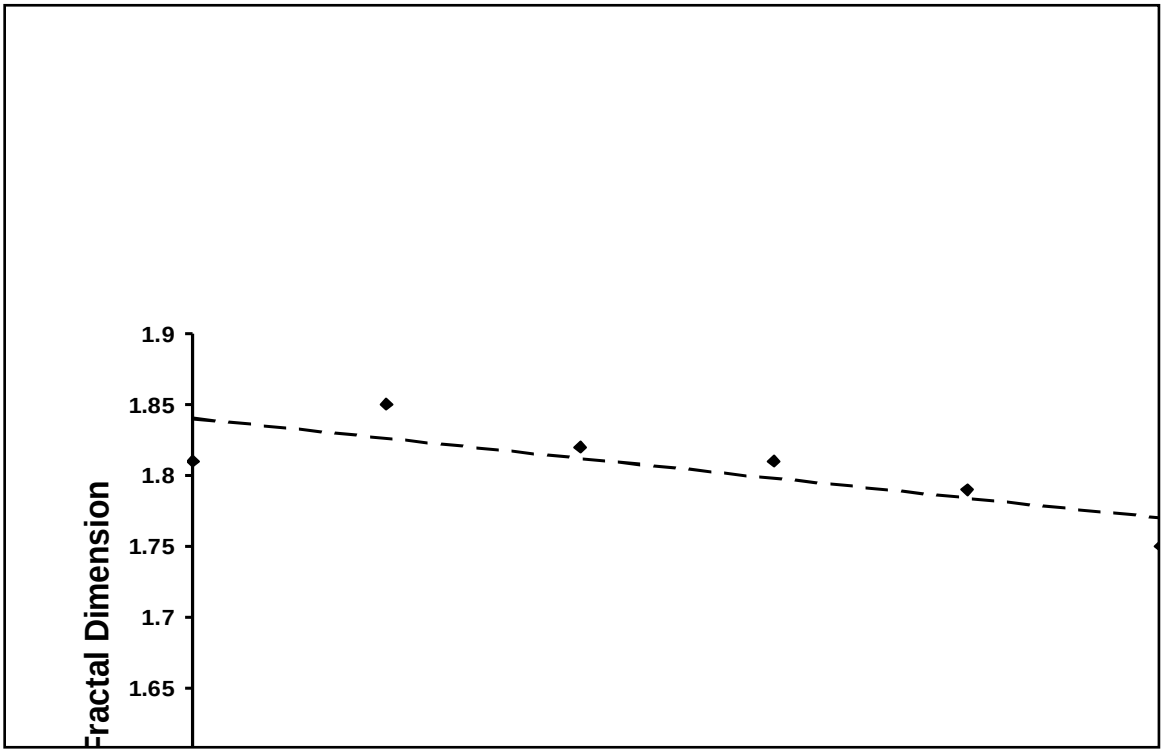

Figure 5.28 Variation in fractal dimension with days of exposure to simulated body fluid.

As can be seen from Figure 5.28 the fractal dimension marginally rises and then gradually drops as the day's progress. To understand this much further it was decided to study the morphological evolution during the first two days at higher magnification.

Figure 5.29 shows regions of the coating where precipitation (white spots and network chains) appear to cover the surface. In addition the $CaTiO_3$ particles seem to provide precipitation sites for hydroxyapatite. The edges of the $CaTiO_3$ particles and porosity induced by the gaps existing between adjacent particles seem to be filling up with precipitate particles. Figure 5.29b shows a region where the network grows and eventually gets connected. The figure also reveals fine pores on all particles (<100nm) as features that likely resulted from dissolution of phases like CaO in the coating.

The thicker regions of network branches are the regions where the CaP-TiO_2 cuboid particles begin to coarsen. The finer dendritic network attaching to these thicker chains are created from edges of $CaTiO_3$ particles as discussed earlier. Such finer particulate evolution explains for minor rise in the fractal dimension as observed in Figure 5.28. After the first two days the precipitated particles coarsen followed by coalescing and bridging across finer networks. The evolution of which is discussed earlier in Figures 5.26. Biomimetic growth rate is monitored for various samples after two days of immersion. The weight of the coupon before immersion and weight of sample after two days of immersion are recorded. The ratio of gain in weight with respect to its weight prior to immersion is referred to as biomimetic growth rate. Figure 5.30 presents this ratio for laser processed samples. The uncoated Ti-6Al-4V surface is for reference. Clearly sample processed at 250 cm/min having higher degree of biomimetic growth. It also supports the fact that the this sample has multi-scale features which consisted of fractal dimensions over multiple length scales seems to support greater degree of biomineralization.

5.7.3 Wear of CaP coatings

Bioimplants over a period of time become loose because of wear and are susceptible to failures. Titanium alloys although having good strength to weight ratios and ideal for load bearing applications have poor wear resistance. In the present work bioceramic calcium phosphate was coated onto Ti alloy to not only enhance biocompatibility but also improve the wear and hardness of the surface. Moreover laser processing has earlier been reported have improved the surface hardness and wear performance of Ti alloys hence there is interest to see if the surfaces presented have seen similar trend.

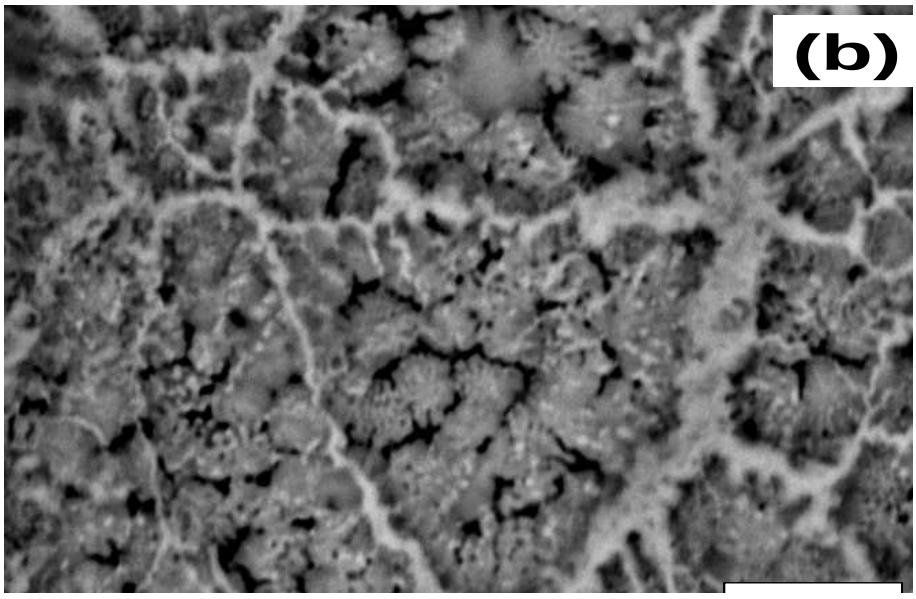

Figure 5.29 SEM micrograph showing (a) network of hydroxyapatite crystallized(white region) around star shaped features after 1 day of exposure.(b) region showing bridging of networks across the surface

.

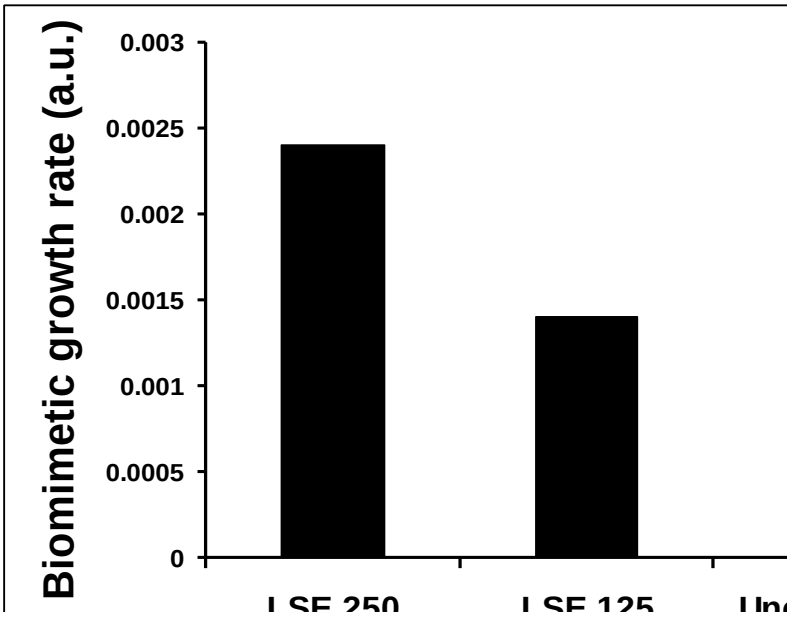

Figure 5.30 Biomimetic growth rate for various surface conditions.

For wear analysis to simulate a scenario similar to biological system a modified pin on disc study arrangement was conceived with wear experiments conducted in a cylinder of simulated body fluid liquid (refer to Figure 3.4).Results from wear analysis done in simulated body fluid also showed that laser processed samples showing better wear performance than untreated surface as shown in Figure 5.31. To further understand this improved mechanical performance of laser processed samples a cross section was performed on the sample processed at 200 cm/min. As can be seen from Figure 5.32a there is a coating followed by a martensitic Ti (α') region that has resulted when quenched from high temperature β phase. Figure 5.32b shows the α+β Ti region. In the figure the equiaxed region is shows α (light) with intergranular retained β(dark).

Figure 5.31 Wear rate post 12000 revolutions for surfaces with and without laser processing..

This martensitic Ti consists of individual platelets which are twinned and have been reported to have HCP crystal structure [88]. It has been shown that martensitic Ti is much harder than α-Ti and thus explains for the improved wear performance [88].

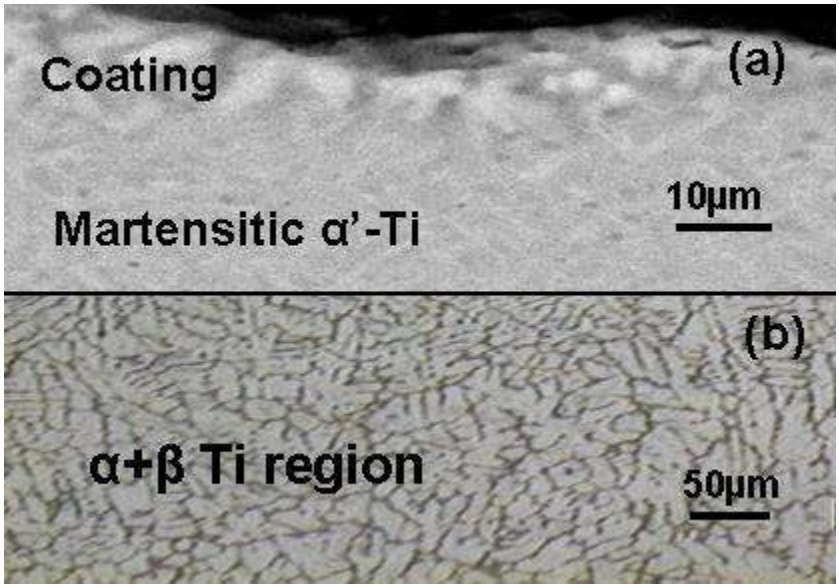

Figure 5.32 Variations in microstructure as observed by (a) SEM image of the coating region along with martensitic Ti phase below it(b) optical image of heat effected zone below showing α+β region.

Chapter 6

Conclusions and Suggested Future Work

6.1 Conclusions

- Bioceramic zirconia coating was achieved on Ti alloy surface via laser surface engineering. Modulating the speed of the laser changed the extent of retained zirconia as well as the final morphology. The success of this proof of concept paved wave for detailed experimentation with CaP coatings.
- Bioactive calcium phosphate based coatings were developed on Ti alloy surface via laser processing. The coatings are multi-scale.
- Chemical analysis revealed a variation in the distribution of phases with laser processing. Faster laser processing speeds >175 cm/min showed higher concentrations of $CaTiO_3$ along with TCP in the final coating.
- Thermal data coupled with chemical analysis showed that faster laser processing lead to greater retention of calcium phosphate constituents and greater interaction with substrate leading to the formation of $CaTiO_3$, CaP-TiO_2 assemblies.
- Morphological analysis of the coating revealed a hierarchically evolved coating for faster speeds (>175 cm/min). In general there was star shaped micron scale shaped arrangement of $CaTiO_3$ phases inside cellular shaped structures rich in Ca-P and TiO_2 phases. These cellular shaped structures are in turn an assembly of cuboids at sub-micron scale.
- Multi-scale porosity resulted in a fractal surface that mimics natural materials were created by modulating laser speed. This coupled with presence of bioactive phases and

greater distribution of these chemical features resulted in enhanced biomimetic hydroxyapatite precipitation when exposed to SBF.

- The laser processed coatings also exhibited better wear and hardness performance than substrate alloy.

.

6.2 Future work

The present work showed the feasibility of coating Ca-P rich surface on Ti while simultaneously inducing a morphological texture via phase evolution. The speed of laser process was the key parameter that was used for evaluation and thermal modeling was done based on these parameters. This chemistry induced texturing offers possible solutions for enhanced biocompatibility. However before this can be translated into real performance there are few areas that need to be addressed:

- Exhaustive cell and biological testing on laser processed surfaces. The in-vitro cell culture studies will provide insights into how effective the multi-scale features proposed and produced in the work are from biocompatibility perspective.
- Self assembly has been described to play critical role in the evolution of final morphology. The charge development and subsequent self assembly of these charged particles has been discussed in the present work based on experimental observations post laser. The future work would focus on developing explanations for why specific set of charge localization happens based on crystallographic arrangement. Are they any specific crystallographic planes which have a tendency to assist this charge localization need to be

known? Liquid TiO_2 has been reported to have electrical conductivity [106]. The role it plays in such assembly need to be studied.

- In the present work conventional contact angle based wettability analysis measurements were reported. Since these involve large liquid droplets compared to the size of the features that are to be studied it poses significant challenges in real applicability to methodologies that need to be adopted when interpreting the data. One solution to this challenge seems to be in developing mathematical models based on fluid dynamics at micron and nanoscale. The future efforts, therefore, will include both experimental design and theoretical modeling for studying the effects of micro to nanoscale morphological and chemical (phases) features on wettability at such fundamental scale.
- The role of residual stress during accelerated cooling conditions induced by laser processing influence the nature of the phases, their evolution and arrangement in the final structure. Future work would delve into investigating the role played by these factors in the final coating.

References

List of References

1 . Kurella, A.K, and Dahotre, N.B.(2005). Review paper: surface modification for bioimplants: the role of laser surface engineering, - *Journal of biomaterials applications*, Vol. 20, No. 1, 5-50.

2 . Park, J. B., Bronzino, J. D. and Kim, Y. K. (2003). Metallic Biomaterials, Ceramic Biomaterials, In: Park, J. B., Bronzino, J. D, editors. *Biomaterials Principles and Applications*, pp. 1-45, CRC Press, Boca Raton, USA.

3 . Ratner, B. D., Hoffman, A. S., Schoen, F J. and Lemons, J. E. (2004). Biomaterials Science : A Multidisciplinary Endeavor, Classes of Materials Used in Medicine, In: Ratner, B. D., Hoffman, A. S., Schoen, F J. and Lemons, J. E., *e*ditors. *Biomaterials Science*, 2nd Edition, pp. 1-209, Elsevier Academic Press, San Diego, California, USA.

4 . Pilliar, R.M., and Weatherly, G.C. (1984). Developments in Implant Alloys, *CRC Crit. Rev. Biocompatibility*, **1**: 371-403.

5 . Ratner, B. D., Hoffman, A. S., Schoen. (2004). Physicochemical Surface Modification of Materials Used in Medicine, In: Ratner, B. D., Hoffman, A. S., Schoen, F J. and Lemons, J. E., *e*ditors. *Biomaterials Science*, 2nd Edition, pp. 201-218, Elsevier Academic Press, San Diego, California, USA.

6 . Wang, K. (1996). The Use of Titanium for Medical Applications in the USA**,** *Mater. Sci. Eng.*, **213**:134-137.

7 . Sioshansi, P. and Tobin, E. J. (1996). Surface Treatment of Biomaterials by Ion beam Process, *Surf. Coat. Technol.*, **83**:175-182.

8 . Bhushan, B. and Gupta, B. K. (1991). Metals and Ceramics, In: Bhushan, B. and Gupta, B.K., editors, *Handbook of Tribology: Materials, Coatings and Surface Treatments,* pp 4.57, McGraw-Hill, Inc., New York.

9 . Piconi, C. and Maccauro, G. (1999). Zirconia as a Ceramic Biomaterial, *Biomaterials***, 20:** 1-25.

10 .Chevalier, J. J., Deville, S., Münch, E., Jullian, R. and Lair**,** F. (2004). Critical Effect of Cubic Phase on Aging in 3 mol% Yttria-stabilized Zirconia Ceramics for Hip Replacement Prosthesis, *Biomaterials*, **25**: 5539-5545

11 . Christel, P., Meunier, A. Dorlot, J.-M. (1988). Biomechanical Compatibility and Design of Ceramic Implants for Orthopaedic Surgery, *Ann. N.Y. Acad. Sci.*, **523**: 234-56.

12 . Yang, Y., Ong, J.L. and Tian, J. (2003).Deposition of Highly Adhesive ZrO2 Coating on Ti and CoCrMo Implant Materials using Plasma Spraying, *Biomaterials*, **24**: 619-627.

13 . Suchanek, W. and Yoshimura M.(1998). Processing and Properties of Hydroxyapatite-based Biomaterials for use as Hard Tissue Replacement Implants, *J. Mater. Res.*, **13:** 94-117.

14 . Lossdörfer, S., Schwartz, Z., Lohmann, C. H., Greenspan, D.C., Ranly, D.M. and Boyan, B.D. (2004). Osteoblast Response to Bioactive Glasses In vitro Correlates with Inorganic Phosphate Content, *Biomaterials*, **25**: 2547-2555.

15 . Healy, K.E. and Ducheyne, P.(1992). Hydration and Preferential Molecular Adsorption on Titanium In vitro, *Biomaterials*, **13**: 553-561.

16 . Curtis A. and Wilkinson C. (1997). Topographical Control of Cells, *Biomaterials,* **18**:1573-1583.

17 . Tan,J. and Saltzman,W.M.(2004). Biomaterials with hierarchically defined micro- and nano-scale structure,*Biomaterials*,**25:** 3593-3601

18 . Lemons, J.E. (1996). Ceramics: Past, Present, and Future, *Bone*, **19**: S121-S128.

19 . Zhu, B., Zhang. Q., Lu, Q., Xu, Y., Yin, J., Hu, J. and Wang, Z. (2004). Nanotopographical Guidance of C6 Glioma Cell Alignment and Oriented Growth, *Biomaterials*, **25**: 4215-4223.

20 . Curtis A. and Wilkinson C. (1998). Reaction of Cells to Topography. *J. of Biomaterials Science*. *Polymer edition*.**9**:1313-1329.

21 . Flemming, R. G., Murphy, C. J., Abrams, G. A., Goodman S. L. and Nealey, P. F. (1999). Effects of Synthetic Micro- and Nano-Structured Surfaces on Cell Behavior, *Biomaterials*, **20**: 573-588.

22 . Wilkinson, C. D. W., Riehle, M., Wood, M., Gallagher, J. and. Curtis, A. S. G. (2002). The use of Materials Patterned on a Nano- and Micro-metric Scale in Cellular Engineering, *Mater. Sci. Eng. C*, **19**: 263-269

23 . Craighead, H. G., James, C. D. and Turner, A. M. P. (2001). Chemical and Topographical Patterning for Directed Cell Attachment, *Current Opinion in Solid State and Materials Science*, **5:** 177-184.

24 . Karacs, A., Fancsaly, A. J., Divinyi, T., Peto G. and Kovách, G. (2003). Morphological and Animal Study of Titanium Dental Implant Surface Induced by Blasting and High Intensity Pulsed Nd-glass Laser, *Mater. Sci. Eng. C*, **23**: 431–435

25 . Martin, J.Y., Schwartz, Z., Hummert, T.W., Schraub, D.M., Simpson. J., Lankford, J. Jr., Dean, D.D., Cochran, D.L. and Boyan, B.D. (1995). Effect of Titanium Surface Roughness on

Proliferation, Differentiation, and Protein Synthesis of Human Osteoblast-like Cells (MG63). *J. Biomed. Mater. Res.*, **29**: 389-401

26 . Groessner-Screiber, B. and Tuan, R.S. (1992). Enhanced Extracellular Matrix Production and Mineralization by Osteoblasts Cultured on Titanium Surfaces In vitro, *J. Cell Sci.*, **101**: 209-17

27 . Rajnicek, A.M., Britland, S. and McCraig, C.D. (1997). Contact Guidance of CNS Neurites on Grooved Quartz: Influence of Groove Dimensions, Neuronal Age and Cell Type. *J. Cell Sci.*, **110**: 2905-13

28 . Clark, P., Connolly, P., Curtis, A.S.G., Dow, J.A.T. and Wilkinsin, C.D.W. (1990). Topographical Control of Cell behavior- II Multiple Grooved Substrata, *Development*, **108:** 635-44.

29 .Duncan, A.C., Weisbuch, F., Rouais, F., Lazare, S. and Baquey, C. (2002). Laser Microfabricated Model Surfaces for Controlled Cell Growth, *Biosensors Bioelectronics*, **17:** 413-426

30 .Oliveira, A. L., Mano, J. F. and Reis, R. L. (2003). Nature-inspired Calcium Phosphate Coatings: Present Status and Novel Advances in the Science of Mimicry. *Curr. Opinion Solid State Mater. Sci.*, **7:** 309-318.

31 . Kim, H.-W., Koh, Y.-H., Li, L.-H., Lee, S. and Kim, H.-E. (2004). Hydroxyapatite Coating on Titanium Substrate with Titania Buffer Layer Processed by Sol–gel Method, *Biomaterials*, **25:** 2533-2538.

32 .Wei, M., Ruys, A.J., Swain, M.V., Kim, S.H., Milthorpe B.K. and Sorrell, C.C. (1999). Interfacial Bond Strength of Electrophoretically Deposited Hydroxyapatite Coatings on Metals, J. *Mater. Sci., Mater. Med.*, **10**: 401–409.

33 .Wen, J., Leng, Y., Chen, J.Y. and Zhang, C.G. (2000). Chemical Gradient in Plasma-sprayed HA Coatings, *Biomaterials*, **21**: 1339–1343.

34 .Yan,L., Leng, Y. and Weng, L.-T. (2003). Characterization of Chemical Inhomogeneity in Plasma-sprayed Hydroxyapatite Coatings, *Biomaterials*: **24**: 2585-2592

35 . Kweh, S. W., Khor, K. A and Cheang, P.(2002). High Temperature In-situ XRD of Plasma sprayed HA Coatings, *Biomaterials*, **23**: 381-387

36 . Singh, R.K., Qian, F., Nagabushanam, V., Damodaran, R. and Moudgil, B.M. (1994). Excimer Laser Deposition of Hydroxyapatite Thin films, *Biomaterials*, **15:** 522-528

37 . Sardin, G., Varela, M. and Morenza, J.L. (1994). Deposition of Hydroxyapaptite Coatings by Laser Ablation. In: Brown PW, Constanz B, editors. *Hydroxyapatite and Related Materials*: pp. 225-30, CRC Press, London

38 . Fernández-Pradas, J.M., Clèries, L., Martínez, E., Sardin, G., Esteve J. and Morenza, J.L. (2001). Influence of Thickness on the Properties of Hydroxyapatite Coatings Deposited by KrF Laser Ablation, *Biomaterials*, **22**: 2171–2175.

39 .Semak, V.V and Dahotre, N.B. (1998), Laser Surface Texturing, In: N.B. Dahotre, editor, *Lasers in Surface Engineering, Surface Engineering Series*, pp. 35-67, ASM International, Materials Park, OH, USA

40 . Steen, W. M., (1991), Background and General Applications: In, Steen, W.M, editors, *Laser Material Processing*, pp. 7-37, Springer-Verlag, London, UK.

41 . Agarwal, A. and Dahotre, N. B. (2000), Mechanical Properties of Laser Engineered Composite Boride Coating on Steel: A Nanoindentation Approach, *Metall. Mater.Trans. A*, **31A**: 401-407

42 . Dasari, A., Nayak, S., Misra, R.D.K., Popoola, O.O. and Dahotre, N. B. (2002). Evaluation of Laser Surface Engineered Iron Oxide Coatings on Cast Aluminum Alloy for Wear Application, *Mater. Sci. Technol.*, **18:** 11-18.

43 . Dahotre, N. B., Nayak, S. and Popoola, O. O. (2001), Laser Assisted Iron Oxide Coating on Cast Al Alloy for Automotive Engine Application, *Journal of Minerals, Metals and Materials Society (JOM)*, **53**: 44-46.

44 . Hong, M. H., Huang, S. M., Luk'yanchuk, B. S. and Chong, T. C. (2003). Laser Assisted Surface Nanopatterning, *Sensors Actuators A: Physical*, **108**: 69-74

45 . D'Alessio, L., Teghil, R., Zaccagnino, M., Zaccardo, I., Ferro, D. and Marotta, V. (1999). Pulsed Laser Ablation and Deposition of Bioactive Glass as Coating Material for Biomedical Applications, *Appl. Surf. Sci.*, **138-139**: 527-532.

46 . Reimers, H., Gold, J. Kasemo, B., Chakarov, D. (2003). Topographical and Surface Chemical Characterization of Nanosecond Pulsed-Laser Micromachining of Titanium at 532 nm Wavelength, *Appl. Phys. A*, **77**: 491-498.

47 . Nakayama, Y, Matsuda, T. (1995). Surface Microarchitectural Design in Biomedical Applications: Preparation of Microporous Polymer Surfaces by an Excimer Laser Ablation Technique, *J. Biomed . Mater. Res.*, **29**: 1295-301.

48 . Zeng, H. and Lacefield, W.R. (2000). XPS, EDX and FTIR Analysis of Pulsed Laser Deposited Calcium Phosphate Bioceramic Coatings: The Effects of Various Process Parameters, *Biomaterials*, **21**: 23-30

49 . Clèries, L., Martínez, E., Fernández-Pradas, J.M., Sardin, G., Esteve, J. and Morenza, J.L. (2000). Mechanical Properties of Calcium Phosphate Coatings Deposited by Laser Ablation. *Biomaterials*, **21**: 967–971.

50 . Fernandez-Pradas, J. M., Cleries, L., Sardin, G., and Morenza, J.M. (2002). Characterization of Calcium Phosphate Coatings Deposited by Nd:YAG Laser Ablation at 355 nm: Influence of Thickness, *Biomaterials*, **23**: 1989-1994.

51 . Lusquin˜os,F., Pou , J., Boutinguiza, M., Quintero, F., Soto, R., Leo´n, B., Pe´rez-Amor, M.(2005). Main characteristics of calcium phosphate coatings obtained by laser cladding*Appl. Surf. Sci.*, **247** : 486–492

52 . Hao, L. and Lawrence. J. (2003). Effects of CO_2 Laser Irradiation on the Wettability and Human Skin Fibroblast Cell Response of Magnesia Partially Stabilized Zirconia, *Mater. Sci. Eng. C*, **23**: 627-639.

53 . Mele, A., Guidoni, A.G., Kelly, R., Flamini, C. and Orlando, S. (1997). Laser Ablation of Metals: Analysis of Surface-heating and Plume-expansion Experiments, *Appl. Surf. Sci.*, **109-110**: 584-590

54 . Tosto, S., Bartolomeo, A.D. and Lazzaro, P.D. (1996). Surface Ablation by Excimer Laser Irradiation of Ti and Ti6Al4V Alloy, *Appl. Phys. A*, **63**: 385- 389.

55 . Gyorgy, E., Mihailescu, I.N., Serra, P., Perez del Pino, A. and Morenza, J.L. (2002). Single Pulse Nd:YAG Laser Irradiation of Titanium: Influence of Laser Intensity on Surface Morphology, *Surf. Coat. Technol.* **154**: 63-67.

56 . Hallgren, C., Reimers, H., Chakarov, D., Gold, J. and Wennerberg, A. (2003). An In-vivo Study of Bone Response to Implants Topographically Modified by Laser Micromachining, *Biomaterials*, **24**: 701-710.

57 . Callewaert, K., Martelé, Y., Breban, L., Naessens, K., Vandaele, P., Baets, R., Geuskens, G. and Schacht, E. (2003). Excimer Laser Induced Patterning of Polymeric Surfaces, *Appl. Surf. Sci.*, **208-209**: 218-225

58 . Rizvi, N.H. and Apte, P. (2002). Developments in Laser Micro-machining Techniques, *J. Mater. Proc. Technol.*, **127**: 206-210.

59 . Rizvi, N.H. (1999). Production of Novel 3D Microstructures Using Excimer Laser Mask Projection Techniques, In: Courtois, B., Crary, S.B., Ehrfeld, W., Fujita, H., Karam, J.E., Markus, K.W., editors, *Proceedings of SPIE, Design, Test, and Microfabrication of MEMS and MOEMS*, **3680**, pp. 546-552, SPIE, Belligham, WA, USA.

60 .Chauvy, P.F., Madore C and Landolt D.(1998) Variable length scale analysis of surface topography: characterization of titanium surfaces for biomedical applications. *Surf. Coat. Technol.*,**110**:48-56.

61 .Yuan, C.Q., Li. J., Yan. X.P. and Peng Z.(2003).The use of the fractal description to characterize engineering surfaces and wear particles. *Wear,* **255**:315-326.

62 .Kurella, A.and Dahotre,N.B.(2006). A multi-textured calcium phosphate coating for hard tissue via laser surface engineering, *JOM*,**58**:64-66.

63 .Kurella, A. and Dahotre,N.B.(2006). Laser induced multi-scale textured Zirconia coatings on Ti-6Al-4V. *J. of Mater. Sci.:Mater.in Med.*,**17**: 565-572.

64 Kurella,A. and Dahotre,N.B.(2006). Laser induced hierarchical Calcium Phosphate structures, *Acta Biomaterialia*, **2**: 677-688.

65 .Kurella, A.K., Hu, M.Z., and Dahotre, N.B.(2008). "Effect of Microstructural Evolution on Wettability of Laser Coated Calcium Phosphate on Titanium Alloy," *Materials Science and Engineering C*,**28**:1560-1564.

66 .Kurella A.K.,Samant,,A. and Dahotre,N.B.(2009). Laser surface multilevel self-assembly of CaP-TiO_2 particles, *Journal of Applied Physics*, **105**:014913.

67 .Lawrence.J.(2002). Contrasting the beam interaction characteristics of selected lasers with a partially stabilized zirconia bio-ceramic. *J. Phys. D: Appl. Phys*.**35:**1828–1832

68 . Dyshlovenko, S.,Pateyron,B., Pawlowski,L. and Murano,D.(2004). Numerical simulation of hydroxyapatite powder behaviour in plasma jet. *Surface and Coatings Technology*, **179**:110-117.

69 .Samant, A.N., Dahotre, N.B.(2009). Laser machining of structural ceramics-A review, *J. of the European Ceramic Society*, **29**: 969-993.

70 . Samant, A.N., Dahotre, N.B.(2009). Differences in physical phenomena governing laser machining of structural ceramics, *Ceramics International,* **35**:2093-2097.

71 . Samant, A.N., Dahotre, N.B.(2008). Computational predictions in single-dimensional laser machining of alumina , *International Journal of Machine Tools and Manufacture*, **48**:1345-1353.

72 .Harimkar, S. P., Samant, A.N. and Dahotre, J.(2007). Temporally Evolved Recoil Pressure Driven Melt Infiltration During Laser Surface Modifications of Porous Alumina Ceramic. *J. of Appl. Phys*. **101**:054911.

73 . Harimkar,S.P., Samant,A.N., Khangar, A.A., and Dahotre,N.B.(2006). Prediction of Solidification Microstructures During Laser Dressing of Alumina-based Grinding Wheel Material,*J. Physics-D: Applied Physics*.**39**:1642-1649.

74 .Boivineau,M., Cagran, C., Doytier,D., Eyraud,V., Nadal, M.-H., Wilthan, B. and Pottlacher,G.(2006) *Intern. J. of Thermophysics*, **27**:507-529.

75 . Guillot‐Noël,O., San Roman, R.G. , Perrière, J., Hermann, J., Craciun, V., Leborgne, C.B., Barboux , P.(1996). *J.of Appl. Physics*, **80**:1803.

76 . Incropera, F. P. and Dewitt, D.P. (2002).*Fundamentals of Heat and Mass Transfer,* Wiley, New York.

77 . Oyane,A., Kim, H-M., Furuya, T., Kobuko, T., Miyazaki, T., Nakamura,T.(2003). Preparation and assessment of revised simulated body fluids. *J Biomed Mater Res A*,**65**:188-95.

78 . Kadolkar, P., Wang, H., Watkins, T.R. and Dahotre, N.B.(2003). Infrared thermography during laser surface engineering of ceramic coating on metal. *International J. of Adv. Manuf. Technol*, **23**: 350-357.

79 . Nayak, S., Wang, H., and Dahotre, N.B.(2004).Thermography during laser surface melting of cast aluminum alloy, *Materials Science and Technology*, **20**: 1609-1614.

80 . Dahotre, N.B., Kadolkar, P., and Shah, S.(2001).Refractory ceramic coatings: processes, systems, and wettability and adhesion. *Surface and Interface Analysis*,**31**: 659-672.

81 .Singh, A. and Dahotre, N.B. (2005). Phase evolution during laser *in-situ* carbide coating. *Metall. Mater. Transact. A*, **36A**: 1-7.

82 .Agarwal, A. and Dahotre, N.B.(2000).Mechanical properties of laser engineered composite boride coating on steel: a nanoindentation approach.*Metall. Mater. Transact.* **31A**: 401-407.

83 . Katepelli, L.R., Agarwal,A. and Dahotre, N.B.(1999). Laser surface engineered TiC Coating on 6061 Al Alloy: microstructure and wear. *Applied Surface Science*,**153(2-3)**:65.

84 . Malinov, S. Sha, W., Guo, Z., Tang, C. C. and Long, A. E.(2002).Synchrotron X-ray siffraction study of the phase transformations in titanium alloys. *Materials Characterization*, **48:**279-295.

85 . Cullity BD. Chemical analysis by X-Ray diffraction. In: Cullity BD. Elements of X-Ray diffraction. Addison- Wesley Publishing Company, Inc. Philippines: 1978. p. 397-417.

86 . Abkowitz, S., Burke, J.J., Hiltz Jr., R.H.(1955). Alloying and heat treatment. In: Abkowitz, S., Burke, J.J., Hiltz Jr., R.H: *Titanium in industry*. D. Van Nostrand Company, Inc. New York, USA: 50-70.

87. Singh, R., Martin, M. and Dahotre, N.B.(2005). Influence of laser surface modification on corrosion behavior of stainless Steel 316L and Ti6Al4V in simulated body fluid. Accepted for publication in *Surface Engineering*, January 12, 2005

88. Singh. R,, Kurella, A., and Dahotre, N.B.(2005). Laser Surface Modification of Ti-6Al-4V: Characterization of wear and corrosion in simulated body fluids,*Journal of Biomaterials Applications*,**21**:29-43.

89 . Guillemot, F., Prima, F., Tokarev, V.N., Belin, C., Port´e-durrieu1, M.C., Gloriant ,T., Baquey Ch, Lazare, S.(2003). Ultraviolet laser surface treatment for biomedical applications of titanium alloys: morphological and structural characterization. *Appl. Phys. A*, **77**: 899–904.

90 . De Vries, R.C., Roy, R. and Osborn, E.F.(1954). Phase equilibrium in the system of CaO-TiO_2, *J. Phys. Chem.*, **58**:1069-1073.

91 . Sun,L., Berndt,C.C. and Grey,C.P.(2003). Phase, structural and microstructural investigations of plasma sprayed hydroxyapatite coatings, *Materi.Sci.&Eng.A*,**360**:70-84.

92 . Barnard, A.S., and Zapol,P.(2004). Predicting the Energetics, Phase Stability, and Morphology Evolution of Faceted and Spherical Anatase Nanocrystals. *J. Phys. Chem. B* **108**:18435-18440

93 . Chiang, M. Birnie III, D.P. and Kingery, W.D.(1997) in: M.Chiang, D.P. Birnie III, and W.D.Kingery (Ed.), *Physical ceramics, Principles for ceramics science and Engineering*, John Wiley & Sons, New York,.

94 . Kralchevsky, P.A., Denkov,N.D.(2001). Capillary Forces and Structuring in Layers of Colloid Particles,*Current Opinion in Colloid & Interf. Sci.***, 6:**383-401.

95 .Danov, K.D., Kralchevsky, P.A.,Naydenov, B.N., Brenn, G.(2005). Interactions between Particles with an Undulated Contact Line at a Fluid Interface: Capillary Multipoles of Arbitrary Order, *J. of Colloid and Interf. Sci,* **287:1**21-134.

96 . Kralchevsky, P.A., Denkov, N.D. and Danov, K.D.(2001). Particles with an Undulated Contact Line at a Fluid Interface: Interaction between Capillary Quadrupoles and Rheology of Particulate Monolayers,*Langmuir*,**17:**7694-7705.

97 . Fournier,J.-B., Galatola,P.(2002). Anisotropic capillary interactions and jamming of colloidal particles trapped at a liquid-fluid interface. *Phys. Rev. E,* **65**:031601-031605..

98 .Toyoda,S., Fujino, S., Morinaga, K.(2003). Density, viscosity and surface tension of 50RO–50P2O5 (R: Mg, Ca, Sr, Ba, and Zn) glass melts, *J. of Non-Crystalline Solids*, **321:** 169-174

99 .D'Anna,G., and Gremaud,,G. (2001).The jamming route to the glass-state in weakly perturbed granular media, *Nature*,**413**: 407-409.

100 . Hao, L. and Lawrence, J.(2003). Effects of CO2 laser irradiation on the wettability and human skin fibroblast cell response of magnesia partially stabilised zirconia .*Mat. Sci.& Eng. C.* **23**:627-639.

101 . Eustathopoulos,N., Nicholas,M.G.and Drevit, B.(1999) in: *Wettability at High Temperatures*, Pergamon, New York:36-39.

102 . Agathopoulos, S., Nikolopoulos, P., Salomoni, A., Tucci, A. and Stamenkovic, I.(1996). Preparation and properties of binary oxide bioceramics. *J.Mater. Sci: Mater. in Med.* **7**: 629.

103 .Bento, A.C., Almond, D.P., Brown, S. and Turner,I. (1996). Thermal and optical characterization of the calcium phosphate biomaterial hydroxyapatite. *J. Appl. Phys*.**79** :6848.

104 .Paital,S., and Dahotre, N.B.(2007). Laser surface treatment for porous and textured Ca–P bio-ceramic coating on Ti–6Al–4V *Biomedical Materials*.**2:**274-281.

105 . Grassmann O., Heimann, R.B.(2000). Compositional and microstructural changes of engineered plasma-sprayed hydroxyapatite coatings on Ti6Al4V substrates during incubation in protein-free simulated body fluid. *J Biomed Mater Res*,**53**: 685-693.

106. Naomi, A.F.(1996). Electrical properties of binary solutions of molten Titanium oxide-Barium oxide, PhD dissertation thesis, MIT.

Appendices

Appendix A: List of Publications

1. **Kurella, A.K**, and Dahotre, N.B.(2005). Review paper: surface modification for bioimplants: the role of laser surface engineering, - *Journal of Biomaterials Applications*, Vol. 20, No. 1, 5-50.
2. **Kurella A.K**., Samant,,A. and Dahotre, N.B.(2009). Laser surface multilevel self-assembly of CaP-TiO_2 particles, *Journal of Applied Physics*, **105**:014913.
3. **Kurella, A**.and Dahotre, N.B. (2006). A multi-textured calcium phosphate coating for hard tissue via laser surface engineering, *JOM*,**58**:64-66
4. **Kurella, A**. and Dahotre,N.B.(2006). Laser induced multi-scale textured Zirconia coatings on Ti-6Al-4V. *Journal of Materials. Science: Materials.in Medicine.*,**17**: 565-572.
5. **Kurella,A**. and Dahotre,N.B.(2006). Laser induced hierarchical Calcium Phosphate structures, *Acta Biomaterialia*, **2**: 677-688.
6. **Kurella, A**., Hu, M.Z., and Dahotre, N.B.(2008). "Effect of Microstructural Evolution on Wettability of Laser Coated Calcium Phosphate on Titanium Alloy," *Materials Science and Engineering C*,**28**:1560-1564.
7. Singh,R., **Kurella**, A., Dahotre, N.B (2006)Laser surface modification of Ti-6Al-4V: wear and corrosion characterization in simulated biofluid,. - *Journal of Biomaterials Applications*,**21**:49-73
8. Engleman, P,G., Dahotre, N,B., **Kurella**, A., Samant, A., Blue, C,A. (2005)-The application of laser-induced multi-scale surface texturing, *JOM Journal of the Minerals, Metals and Materials Society*, **57:**1047.

9. **Kurella**,A., Dahotre, N,B.(2006) Phase and Morphological Evolution in Laser Textured Zirconia Coating on Ti alloy, *TMS outstanding award winning graduate paper*.
10. **Kurella**,A., Dahotre, N,B (2005).Multi-scaled Textured Coatings for Bioimplant Applications, Dahotre, *MST 2005*, Pittsburg, USA.

Appendix B: Reprints of publications.

Review paper: Surface Modification for Bioimplants: The Role of Laser Surface Engineering

ANIL KURELLA[1] AND NARENDRA B. DAHOTRE[1,2,*]
[1]*Department of Materials Science and Engineering*
The University of Tennessee, Knoxville, Tennessee 37996, USA
[2]*Materials Processing Group, Metals and Ceramics Division*
Oak Ridge National Laboratory
Oak Ridge, Tennessee 37831, USA

ABSTRACT: Often hard implants undergo detachment from the host tissue due to inadequate biocompatibility and poor osteointegration. Changing surface chemistry and physical topography of the surface influences biocompatibility. At present, the understanding of biocompatibility of both virgin and modified surfaces of bioimplant materials is limited and a great deal of research is being dedicated to this aspect. In view of this, the current review casts new light on research related to the surface modification of biomaterials, especially materials for prosthetic applications. A brief overview of the major surface modification techniques has been presented, followed by an in-depth discussion on laser surface modifications that have been explored so far along with those that hold tremendous potential for bioimplant applications.

KEY WORDS: biomaterials, interface, surface modification, bioimplants, osteointegration, lasers, coating, texturing.

INTRODUCTION

It is rare to find a material that meets all the requirements of a given application and biomaterials are no exception. For example,

*Author to whom correspondence should be addressed. E-mail: ndahotre@utk.edu

0885-3282/05/01 0005–46 $10.00/0 DOI: 10.1177/0885328205052974
© 2005 Sage Publications

Downloaded from http://jba.sagepub.com at OKLAHOMA STATE UNIV on March 23, 2009

JOURNAL OF APPLIED PHYSICS 105, 014913 (2009)

Laser surface multilevel self-assembly of CaP–TiO_2 particles

Anil K. Kurella,[a] Anoop N. Samant, and Narendra B. Dahotre[b]
Department of Materials Science and Engineering, Laboratory for Laser Materials Synthesis and Fabrication, University of Tennessee Knoxville, Tennessee 37996, USA

(Received 4 November 2008; accepted 23 November 2008; published online 15 January 2009)

Laser surface engineering of calcium phosphate coatings on Ti alloy is carried out in the present work. Using a continuous wave neodymium doped yttrium aluminum garnet laser, hierarchically textured multiphase coatings were engineered at multiple processing speeds. The evolution and enclosure of star shaped $CaTiO_3$ particles inside a calcium phosphate and TiO_2 rich circularly assembled cuboid particles was characteristic of higher laser processing speeds (>2000 mm/min). Self-assembly strongly dictated by thermochemical interactions resulted in creating such multiscale and multiphase textured surfaces. © *2009 American Institute of Physics*. [DOI: 10.1063/1.3065460]

I. INTRODUCTION

Calcium phosphate (CaP) based coatings on Ti alloys have been shown to provide good osteointegration.[1,2] In addition, surfaces if multiscale textured are expected to provide enhanced osteointegration.[3] The authors in their earlier work have reported laser surface coating and hierarchically texturing at the same time for rendering it bioactive.[4,5] The formation of such structures was believed to be influenced by self-assembly and thermophysical dynamics of CaP–TiO_2 particles (CaP–TiO_2). Laser processing results in high temperature, triggering multiple reactions within various temperature regimes. Each of these reactions is unique and seems to happen at different length scales. Self-assembling has been seen as the driving mechanisms dictating the final morphology in solidified structures. In the present work, the objective is to explore the self-assembling concepts at various length scales and comprehend the dynamics of bioactive phases during laser surface engineering of CaP coatings on Ti alloys.

II. EXPERIMENTAL WORK

A. Sample preparation, laser processing, and surface analysis

Ti–6Al–4V coupons $50\times100\times3$ mm^3 in size were cut and mechanically polished. The average surface roughness of the polished surface is 0.5 μm. A proprietary water based organic solvent (LISI WI5853, Warren Paint and Color Co., Nashville,TN) mixed with CaP Tribasic $Ca_5(OH)(PO_4)_3$ is obtained from Fisher Scientific (Catalog No. C13–500). The Ca:P molar ratio of 1.68 corresponds to the stoichiometric composition of the hydroxyapatite (HA). This was coated onto the coupons using an air spray gun to achieve a thickness of 40 μm. Using a 1064 nm neodymium doped yttrium aluminum garnet laser in continuous wave mode, the samples were processed by scanning a rectangular beam (with dimensions of 5.0×1.5 mm^2) of uniform intensity at speeds varying from 1000 to 2750 mm/min at 850 W power with the laser beam focused on the surface of sample (Fig. 1). The entire surface of the coating was processed by multiple tracks with 15% overlap between subsequent passes. Considering this overlap, roughly 11 tracks were required to coat the entire width of the coating of 50 mm. X-ray diffraction (XRD) analysis was carried out on samples by scanning it from 20° to 100° at steps of 0.02° in a Philips Norelco x-ray diffractometer. A Cu $K\alpha$ radiation with 1.5418 Å wavelength operating at 20 kV and 10 mA was used. The processed samples were also analyzed in a Leo 1525 scanning electron microscope (SEM) attached with energy dispersive x-ray (EDX) analysis.

B. Computational temperature estimation

The chemical and morphological characteristics of the coatings depend on the temperature distribution through the coating and associated cooling rates. Hence, the precursor (CaP Tribasic) and the substrate (Ti–6Al–4V) were modeled for thermal predictions using COMSOL's ™ heat transfer transient mode. The comprehensive model was based on the consideration of composite nature of material system, tempera-

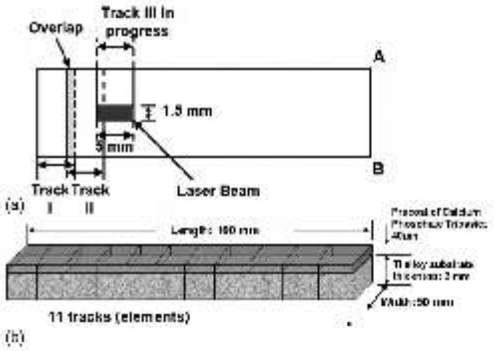

FIG. 1. Schematic of coated sample. (a) 2D view of the ongoing laser processing and (b) 3D view of laser processed sample.

[a]Also at Intel Corporation, Hillsboro, Oregon 97124, USA.
[b]Author to whom correspondence should be addressed. Tel.: 865-974-3609. FAX: 865-974-4115. Electronic mail: ndahotre@utk.edu.

 © 2009 American Institute of Physics

Author complimentary copy. Redistribution subject to AIP license or copyright, see http://jap.aip.org/jap/copyright.jsp

ture dependent thermophysical properties, preheating due to multiple laser tracks and conduction, convection, and radiation dependent heat transfer during laser processing under the formulations and assumptions originally described elsewhere.[6,7] The precursor, represented in the form of a slab (50 mm × 100 mm × 40 μm) and coupled with another slab representing the substrate (50 × 100 × 3 mm^3) simulated a scenario closer to the real sample prior to laser processing. All the speeds at which the processing was carried out were not considered for modeling purpose. The temporal evolution and cooling rates are governed by the input energy and the time for which the energy was incident on the material surface (residence time, t_p). The residence times were calculated by dividing the shorter axis of the laser beam (1.5 mm) by the different processing speeds as the beam traversed along this axis. Thus speeds of 125, 200, and 275 cm/min corresponded to residence times of 72, 45, and 33 ms, respectively. The laser energy density I (1.13×10^8 W/m^2) input to the model was obtained by diving the input power (850 W) by the cross-sectional area of the beam (7.5×10^{-6} m^2). The computations only corresponding to the processing speeds of 1250, 2000, and 2750 mm/min representing the lowest, medium, and highest speeds within the range of speed employed in the current work are presented. However, computations for all other speeds also remained within the same general trend in temperature and cooling rate evolutions provided by these three speeds.

1. Preheating

As mentioned above, 11 tracks were required to cover the entire surface of the coating with 15% overlap. Figure 1(a) shows a two-dimensional (2D) top view of the sample being processed and three-dimensional (3D) view of laser processed samples are presented in Fig. 1. The laser tracks were laid down along the direction from A to B, which as mentioned above was the direction of the track perpendicular to the longer axis of the beam (5 mm) while the gray region is the overlap [Fig. 1(a)]. As a laser track was laid on the surface, the temperature in the neighboring area also increased and the region where the subsequent tracks were be laid got preheated, thus affecting the temperature distribution within the sample. In order to incorporate this effect, the residence time and input energy corresponding to a single track were input to the model and the temperature distribution at the center of this track was obtained [Eqs. (1)–(3) below]. Simultaneously, the maximum temperature at the location where the center of the next track would lie was computed and input as an initial temperature for the following track. This procedure was followed until the computations for all the 11 tracks were completed, thus accounting for the effect of multiple tracks and associated preheating. Practically, a given track would have the preheating effect from not just the track immediately before it but also from the several tracks prior to that track. However, the theoretical computations indicated that under the laser processing and material parameters employed in the present case, the rise in temperature at a distance beyond next neighboring track was marginal (<150 °C); hence, only preheating by the earlier track was considered in the present computations.

2. Conduction

The heat transfer during the laser processing of the coating on the substrate was modeled using Fourier's second law of heat transfer,

$$\frac{\partial T(x,y,z,t)}{\partial t} = \frac{k(T)}{\rho C_p(T)}\left[\frac{\partial^2 T(x,y,z,t)}{\partial x^2} + \frac{\partial^2 T(x,y,z,t)}{\partial y^2} + \frac{\partial^2 T(x,y,z,t)}{\partial z^2}\right], \quad (1)$$

where $k(T)$ and $C_p(T)$ are the variations in thermal conductivity and specific heat as a function of temperature, ρ is the density, T is the temperature field, t is time, and x, y, and z are the spatial directions. For improved accuracy of calculations, variation in thermal conductivity and specific heat as a function of temperature for the coating and the substrate were considered in the model.[8,9] The variation in specific heat as a function of temperature accounted for the latent heat of solidification. At time $t=0$, the initial temperature of $T=T_0=300$ K was applied for the first track, while for the subsequent tracks, in order to incorporate the preheating effect, the maximum temperature induced at the center of the track under consideration by an earlier track was applied as the initial temperature.

3. Radiation and absorptivity

The balance between the absorbed laser energy at the surface and the radiation losses was given by

$$-k(T)\left(\frac{\partial T(x,y,0,t)}{\partial x} + \frac{\partial T(x,y,0,t)}{\partial y} + \frac{\partial T(x,y,0,t)}{\partial z}\right) = \delta a I - \varepsilon\sigma(T(x,y,0,t)^4 - T_0^4),$$

$$\delta = 1 \quad when \quad 0 \le t \le t_p,$$

$$\delta = 0 \quad when \quad t > t_p, \quad (2)$$

where I is the laser energy density mentioned above, $k(T)$ is the temperature dependent thermal conductivity of the material (W/m K), ε is the emissivity for thermal radiation, t_p is residence time, σ is Stefan–Boltzman constant (5.67×10^{-8} W/m^2 K^4), and a is the absorptivity of the material. The term δ takes a value of 1 when the time t is less than the residence time t_p and it is 0 when the time t exceeds the residence time. Thus the value of δ depends on the time t and ensures that the energy is input to the system only during the residence time and cuts off the energy supply after that. As conducting *in situ* absorptivity measurements in short duration high energy density dynamic process such as laser-material interaction is extremely difficult, the value of absorptivity of 0.1 (for the spectral range of 250–450 nm) of the coating material (CaP Tribasic) commonly found in literature was used for the calculations.[10] Based on exhaustive literature survey there was no value available corresponding to the exact absorptivity/emissivity of CaP Tribasic when exposed to 1064 nm wavelength. Hence attempts are ongoing for *in situ* absorptivity/emissivity measurements under laser processing conditions similar to the ones employed in the present study and they will be incorporated in future

Author complimentary copy. Redistribution subject to AIP license or copyright, see http://jap.aip.org/jap/copyright.jsp

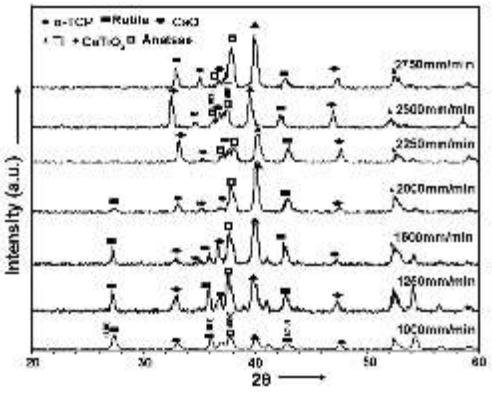

FIG. 2. XRD patterns of laser processed samples at various speeds.

calculations. Furthermore, as the laser energy is directly incident on the coating and it is then transferred to the substrate by different heat transfer phenomena, only the absorptivity of the coating was considered for calculations.

4. Convection

The convection at the bottom surface of the sample was given by

$$-k(T)\left(\frac{\partial T(x,y,D,t)}{\partial x}+\frac{\partial T(x,y,D,t)}{\partial y}+\frac{\partial T(x,y,D,t)}{\partial z}\right) = h(T(x,y,D,t)-T_0), \quad (3)$$

where D is the thickness of the sample, which was taken as 40 μm for the coating and 3 mm for the substrate, and h is the heat transfer coefficient (W/m^2 K), which was also included as a function of temperature.[11] The temperature profiles and the corresponding cooling rates (slope of the cooling curve at different time instants) were obtained from these computations and their effects on the microstructure are discussed in the following part of this paper.

III. RESULTS AND DISCUSSION

A. Chemical nature

XRD patterns of the surfaces treated at various laser processing speeds are presented in Fig. 2. The key compounds that are identified in the XRD patterns are $CaTiO_3$, TiO_2, tricalcium phosphate (TCP), and calcium oxide (CaO) along with Ti phases from the bulk substrate. Table I shows a semiquantitative analysis of various phases present for fast (2500 mm/min) and slow speeds (1500 mm/min). The peak intensity values for various phases were recorded and later normalized with respect to the Ti peak. As can be seen from the patterns there appears to be a trend in the phase evolution with the change in the processing speed. Notable differences seem to be the higher presence of $CaTiO_3$ at faster processing speeds, while TiO_2 (anatase and rutile) is predominantly present at lower speeds. Varying levels of CaO and TCP peaks are present at all processing conditions. Ti readily oxidizes into TiO_2 when exposed to elevated temperatures. Due to high temperatures attained during laser processing the calcium phosphate tribasic (CPT) may have undergone physical and chemical changes through one of the following steps: (a) decomposition into TCP, tetracalcium phosphate (TTCP), CaO, and phosphorus pentoxide (P_2O_5), (b) recrystallization, (c) solidification into anhydrous CaP, and (d) dehyroxylation into oxyhydroxyapaptite.[12] The higher the temperature reached, the more melting and decomposition of the CPT takes place. Table II lists the melting points of these key materials considered for discussion in this paper.[12,13] The effects of peak temperature and cooling rates attained during the process on the abovementioned physical and chemical transitions are discussed in Secs. III B–III G.

TABLE I. Melting points of key phases present in the coating.

Phase	Decomposition/ Melting temperature
CaO	2570 °C (2843 K)
$CaTiO_3$	1970 °C (2243 K)
TiO_2	1830 °C (2103 K)
Ti–6Al–4V	1630 °C (1903 K)
HA	1570 °C (1843 K)
TCP	1391 °C (1664 K)
TTCP	1230 °C (1503 K)

B. Thermodynamics of transformation

With the increase in temperature, the CaP salts dissociate further into CaO and P_2O_5, which eventually vaporize at temperatures above 3123 and 3500 K, respectively.[8] Figure 3 depicts a typical temperature profile of a composite system consisting of CPT precoat and Ti–6Al–4V substrate during the laser processing operation. The values are predicted using COMSOL's ™ heat transfer model discussed earlier. As can be seen, even with this medium processing speed within the range of speed employed in the present work, the peak temperatures reached above 3000 K within sixth track and continued to increase above 3500 K at the end of processing (11th track). This range of temperature is associated with higher evaporative losses of P_2O_5 and CaO constituents from the coating. During the cooling cycle the residual amounts of

TABLE II. Ratios of various phases normalized with Ti.

Speed (mm/min)	TiO_2 rutile (110)	TiO_2 rutile (101)	TO_2 anatase (004)	$CaTiO_3$	TCP	CaO
2500	0.069	0.227	0.522	0.909	0.20	0.466
1500	0.415	0.245	0.831	0.169	0.11	0.481

Author complimentary copy. Redistribution subject to AIP license or copyright, see http://jap.aip.org/jap/copyright.jsp

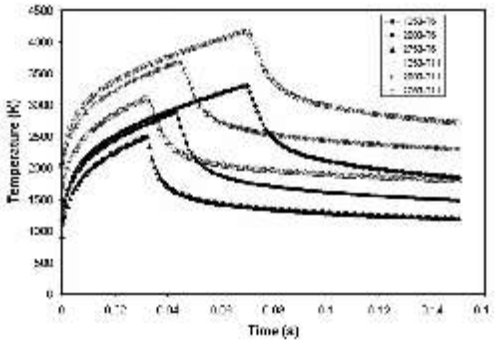

FIG. 3. Computed temperature vs time plots for tracks T1, T6, and T11 in samples processed at 2000 mm/min.

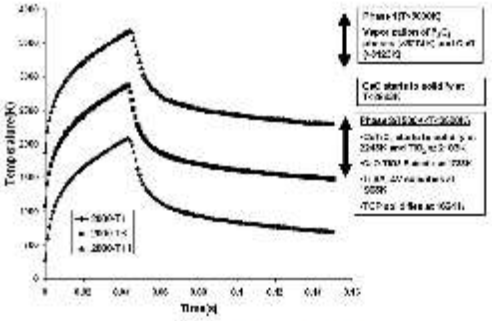

FIG. 5. Computed temperature profiles for tracks T6 and T11 in samples processed at 1250, 2000, and 2750 mm/min.

CaO interacted with TiO_2 to form $CaTiO_3$. TiO_2 was formed and available through oxidation of the Ti–6Al–4V substrate during laser processing. With reference to the binary phase diagram (Fig. 4) (Ref. 12) of the CaO–TiO_2 the possible phases prevalent at room temperature are CaO, $Ca_3Ti_2O_7$, $CaTiO_3$, and TiO_2.[13] Since no $Ca_3Ti_2O_7$ was observed in the XRD patterns (Fig. 2), it can be predicted that interactions resulted in eutectic solidification of $CaTiO_3$ within the region between 58 wt % TiO_2 (42 wt % CaO) and 100 wt % TiO_2 of the phase diagram. On the contrary, for faster processing speeds (≥2000 mm/min) the peak temperatures marginally reached 3000 K by the end of processing (11th track) and likely to have minimal or no evaporative losses of dissociation products of CPT (CaO and P_2O_5) (Fig. 3). Pronounced $CaTiO_3$ peaks seen in faster processing speeds (≥2000 mm/min), therefore, are due to the interactions between CaO, one of the dissociation products of CPT, and TiO_2. Lower temperatures also prevented excess decomposition of CPT as evident in the presence of stronger x-ray peaks of TCP at faster processing speeds (Fig. 2).

C. Kinetics of transformation

Peak temperatures do not alone explain for the complex chemical and morphological natures of the coatings. Cooling rates are to be considered. The various critical temperature regimes in the present CaP–TiO_2 system are discussed below. Typical heating and cooling cycles associated with various laser tracks laid with laser processing speed of 2000 mm/min are presented in Fig. 5. The insets in the figure provide the description of critical transformations occurring within various regions (laser tracks) as function of temperature. The temperatures above 3000 K are referred to range 1, while temperatures in the 1500–2500 K are classified as range 2 region. Range 1 is primarily a region of vaporization of CPT phases (CaO and P_2O_5), whereas range 2 is the regime where CaO and TiO_2 interact to form $CaTiO_3$ over wide range of temperatures. In this regime, the eutectic reaction occurs for ~84 wt % TiO_2–16 wt % CaO composition at 1733 K (Fig. 4). The solidification of Ti–6Al–4V also starts at 1903 K. The phases that are last to solidify in this regime are TCP and TTCP. In other words, these CaP rich phase remain in liquid form until the temperature reaches 1500 K. During laser processing under a given traverse speed, high thermal gradient is associated with rapid cooling at higher temperature level (Fig. 5) and the cooling rate drops with a drop in temperature. Considering the case of laser processing speed of 2000 mm/min (Fig. 5) the temperature drops considerably steeply from 2800 to 2000 K (corresponding average cooling rate 8×10^5 K/s), followed by a gradual drop from 2000 to 1500 K (corresponding average cooling rate of 5×10^3 K/s). The cooling rate continues to decrease with the drop in temperature. Similar observations are recorded for both tracks 6 and 11 in other processing speeds (Fig. 3). In general, if the temperature in track 6 is considered as representative of the average surface temperature in range 2 (2500–1500 K) of all samples, then associated gradual cooling (sufficient time) will be responsible for phases to separate and/or interact within the 2000–1500 K window of this temperature range. Another observation drawn from the phase diagram of CaO–TiO_2 system (Fig. 4) is the steep slope of the liquidus during $CaTiO_3$ solidification.[12] The separation between the solidus and liquidus increases with the increasing concentrations of TiO_2 (decreasing concentration of CaO) indicating there is a wider temperature window (as high as 510 C at around 60 wt % TiO_2) across which the structure remains fluid for longer

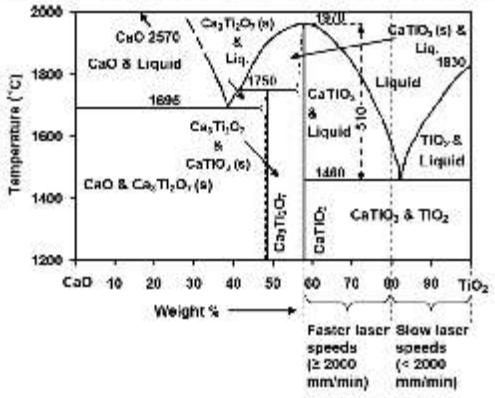

FIG. 4. Binary phase diagram of CaO and TiO_2.

Author complimentary copy. Redistribution subject to AIP license or copyright, see http://jap.aip.org/jap/copyright.jsp

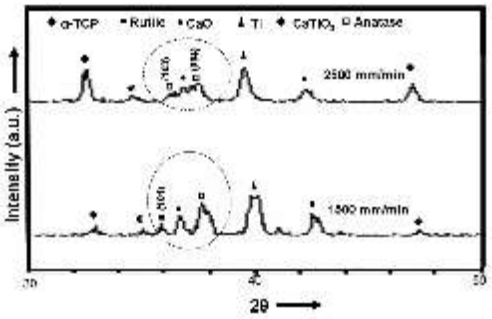

FIG. 6. XRD patterns in 2θ range of 30°–50° for low (1500 mm/min) and high (2500 mm/min) laser processing speeds.

time prior to complete solidification. This bears a tremendous impact on development of phase morphology as function of cooling rate associated with the given processing speed and it is discussed in Secs. III D–III G.

Another interesting observation is the nature of CaO and TiO_2 phases from 33° to 39° (Fig. 6) where the XRD pattern is magnified for two laser processing speeds (1500 and 2500 mm/min) representing high and low speed regimes within the range of speeds employed in the present work. TiO_2 is predominantly present as anatase at higher processing speeds. The TiO_2 peak (004) at 38° has shifted to the left at faster processing speeds above 2000 mm/min. The anatase peaks corresponding to (103) were also observed at higher laser processing speeds. The broadness associated with this peak appears as a shoulder to CaO peak at 37°. The shift and broadness associated with the TiO_2 peaks on both sides of the CaO peak at higher speed indicate a possibility of a glass formation. The broad alpha-TCP peak at 35° at faster speeds with CaO and P_2O_5 constituents coexist in the glass formation chemistry. Comparatively the TCP content was less at lower processing speeds. It is interesting to note under suitable thermodynamic conditions the availability of phases such as CaO (modifier), TiO_2 (network modifier), and P_2O_5 (network former) results in glass forming networks.[14] The broadness in the XRD peaks discussed in this section can be attributed to this possible glass formation.

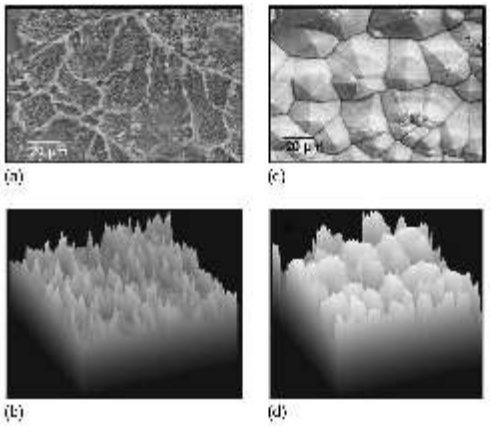

FIG. 8. Low magnification view of laser processed coating. Surface morphology of laser processed coating (a) and the corresponding 3D roughness profile (b). The equiaxed faceted grain structure of the substrate material underneath the coating (c) and corresponding 3D roughness profile.

D. Microstructural evolution

SEM analysis of the coating indicated the existence of cellular arrangement of cuboidal particles with star shaped particles dispersed inside the cellular pattern [Figs. 7(a)–7(c)]. The authors in their previous works based on SEM. EDX and XRD analyses showed that these cuboids are ($CaP–TiO_2$) rich particles, whereas star shaped particles are attributed to $CaTiO_3$.[4] Ca, P, Ti, and O peaks were detected in EDX analysis on the walls of cellular and star structures as can be seen in Figs. 7(d) and 7(e). The low magnification view of such uniquely textured coating and corresponding 3D representation are presented in Figs. 8(a) and 8(b), re-

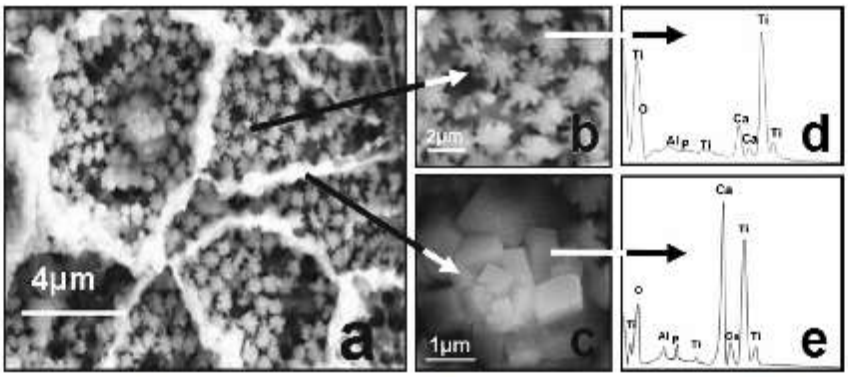

FIG. 7. Scanning electron micrograph of laser processed coating. (a) Surface morphology with starlike particles enclosed in ringlike assembly of cuboidal particles, (b) high magnification view of starlike particles, (c) high magnification view of cuboidal particles, (d) EDS spectrum of starlike particle and EDS spectrum of cuboidal particle.

Author complimentary copy. Redistribution subject to AIP license or copyright, see http://jap.aip.org/jap/copyright.jsp

spectively. Careful removal of the coating at selected locations followed by electron imaging at those locations also revealed equiaxed faceted grain structure of the underneath Ti–6Al–4V substrate [Fig. 8(c)]. The 3D projection corresponding to this structure is presented in Fig. 8(d). This observation falls in line with earlier observation[4] where CaP–TiO_2 rich phases form a ringlike structure around star shaped $CaTiO_3$ and TiO_2. This ring and star shaped arrangements were seen clearly at speeds greater than 2000 mm/min. At lower speeds this arrangement was observed on a limited scale. It is believed that this multiscale morphology is interesting from an osteointegration perspective. Going forward the present paper will focus on the evolution of cuboids and star structures and possible dynamics behind their assembly

E. Dynamics of particulate formation

Surface roughness and/or chemical inhomogeneity at site specific locations on a particle in a fluidic interface could result in undulated or irregular contact line. These undulations when overlapped induce change in the surrounding liquid interface resulting in capillary interactions. Such surface deviations on neighboring particles, either convex or concave from planarity, are considered as negative or positive charges.[15,16] Such interaction can either be flotation or immersion in nature. The perturbation in the shape of the liquid due to two such particles results in lateral capillary forces.[17] These capillary interaction forces are either flotation or immersion in nature. In general, for charges the interaction is isotropic but for multipoles the interaction sign and magnitude are influenced by mutual orientation of particles. In the present case, during early part of laser processing, any TiO_2 particle with area covered by CaP will have one type of charge/wettability characteristics as opposed to the other locations (CaP has different wettabilities compared to TiO_2). With respect to the liquid such variation in charge/wettability results in formation of hydrophilic and hydrophobic interfaces on the same particle. Such particles qualify to be multipoles (m) and the charge distribution on them makes them dipole ($m=1$), quadrupoles ($m=2$), hexapoles ($m=3$), etc. Based on the SEM and EDX (Fig. 7) analyses, CaP rich TiO_2 particles appeared to self-assemble into cuboid shaped particles. These cuboids are consistent in size (typically 200 nm–1 μm). Due to such specific shape and size associated with the CaP rich TiO_2 cuboids, the underlying self-assembled subparticles are suspected to be quadrupolar.[16,17] The explanation for which is as follows. For a system that contains different multipole orders ($m=1,2,3$, etc) because of the angular dependence of the immersion force, it is difficult to form ordered 2D crystals. In the present case, since CaO–TiO_2 cuboids of specific size were observed the assembly is built with particles having the same multipole order. Furthermore, due to the cuboid (2D square lattice) shape of these particles (Fig. 7), it is speculated that the immersion forces must have predominantly acted between particles that are quadrupolar ($m=2$) in nature. Based on Kralchevsky *et al.*,[15–17] for multipole particle mutual orientation will influence the sign and magnitude of the capillary force. Hence, hexagonal lattice will be preferably formed for hexapoles ($m=3$), while square lattice is preferable for quadrupoles ($m=2$). Fournier and Galatola[18] calculated the interaction energy for various configurations of quadrupoles and reported that square alignment would result in the most stable and ground state condition.

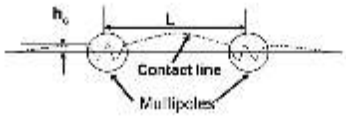

FIG. 9. Schematic of contact line between two capillary multipoles.

F. Energy of interaction between two particulates

Having understood the nature of multipoles, it is important to comprehend the feasibility of their interactions and self-assemblies from a thermodynamic perspective. The following section discusses the possibility of such formations based on theoretical calculation at various length scales. A schematic representation of contact lines between two capillary multipoles is represented in Fig. 9. In such a scenario the theoretical interaction energy between two capillary quadrupoles is given by Eq. (4),[15–17]

$$\Delta W(L) = -12\Pi\sigma H^2 \cos(2\varphi_A + 2\varphi_B)\frac{r_c^4}{L^4} \tag{4}$$

(where $m=2$; $L \gg 2r_c$).

In the above equation undulation in the contact line is represented by H, the average undulation radius is given by r_c, the distance between two particles by L and the angles subtended between diagonals for each qaudrupole are represented by ψ_A and ψ_B, respectively, while σ is the interfacial tension. For quadrupoles when brought in contact the equation can be simplified to Eq. (5),

$$dW = -(3/4)\pi\sigma H^2, \tag{5}$$

where $(r_c/L)=0.5$ and $\cos(\psi_A+\psi_B)=1$ (when they spontaneously rotate).

For interfacial tension of 250 mN/m for CaO–P_2O_5 at 1673 K,[19] the interaction energy exceeds thermal energy (kT) for fluctuations of amplitude of 2 Å. In other words, for the present system capillary interactions between two quadrupoles are considerable even at undulations as small as 2 Å. Kralchevsky *et al.*[17] commented that fluid surface at such small scale is hard to realize and is overridden by rough thermally excited fluctuation capillary waves typically in the 3–6 Å range. Thus moving up the length scale for nanoscale particles, the following calculations consider amplitudes in nanoscale range with undulations significantly larger than the background noises. The capillary interaction energy (dW) turns out to be 1.2×10^3 kT based on calculations made with $H=20$ nm, taking $\sigma=250$ mN/m and $r_c/L=0.3$. Such significant capillary interaction energies can contribute to the assembly of submicron particles into 2D networks along the fluidic interface.[17] These assembled 2D particles form the nucleus for eventual assembly into 3D cuboid structures.

Author complimentary copy. Redistribution subject to AIP license or copyright, see http://jap.aip.org/jap/copyright.jsp

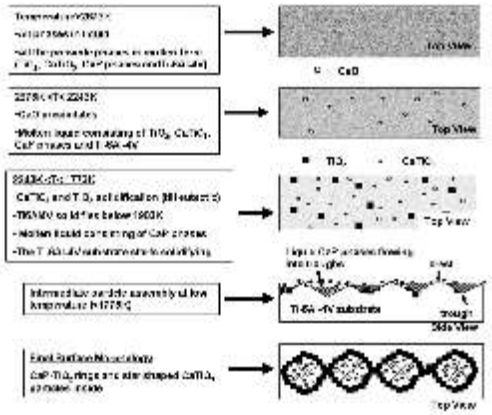

FIG. 10. Schematic of evolution of possible morphological features in the coating as function of temperature during cooling cycle.

Fournier and Galatola[18] reported that a jammed system resulted when large number of such particles attached to each other under such strong capillary conditions.

G. Macro- and microscale self-assembly of particulates

Self-assembling has been observed at multiple length scales. So far the self-assembling concepts of cuboid particle formation at submicron level under the action of immersion capillary forces from an energy calculations have been explored. The following portion describes their physical movement and orientation into ringlike patterns at microscale under the influence of temperature and evolution of other phases during solidification. As the core cuboids grow in size and the liquid surrounding starts to evaporate, the convective particle flux results in drag forces (F_d). Hydrodynamic drag mechanism, mostly influenced by evaporation of the liquid wetting film, results in convective assembly that will result either in accumulation of these cuboids at the center or dragged to periphery and pinned by local point of contacts. This is further assisted by morphological modifications due to multiphase evolution as a result of solidification process during the cooling cycle postlaser processing. The observation of facet morphology and crest/trough formation on underlying Ti–6Al–4V alloy during solidification as described earlier [Fig. 8(c)] is the basis for this explanation. Figure 10 illustrates in detail the sequential evolution of various phases during the cooling cycle. During solidification, owing to the fact that CaP phases are the last one to solidify (melting point ~1664 K), they are expected to be moved around the topographies created by already solidified $CaTiO_3$ from the top [Fig. 8(a)] and Ti–6Al–4V from the bottom [Fig. 8(c)]. Few of the solidified TiO_2 particles within this CaP liquid are hydrodynamically dragged and irreversibly stuck at the troughs created during subsequent solidification process of the CaP liquid. This is further enhanced by the pinning action typically associated with such particles along the contact line in the trough. Often the contact line undergoes a sequence of pinning-depinning events with particles accumulating whenever the contact line is pinned. The pinning process where the particles irreversibly stick to the substrate is under the influence of normal capillary force. Such pinned locations as a result of these stuck particles are the points where accumulation of particles happens during subsequent evaporation and hydrodynamic drag force exertion. In cases where there is no sufficient CaP phases left (slower laser processing speeds) on the surface only the Ti alloy solidified in faceted morphology and where there was less vaporization of CaP (higher processing speeds) the phases oriented above the substrate morphology.

The phenomenon of pinning or jamming usually impacts glass forming systems, which during sudden transition to amorphous phase exhibit a slowdown in their dynamics. Thus vitrification via supercooling aids in creating these pinning locations. Temperature that typically controls this transition causes geometrical constrains that help in buildup of particles at these locations and restrict any other formation.[20] As stated earlier, the present system has glass forming tendency. Under favorable cooling rates it has been reported earlier that P_2O_5 acts as network former, while TiO_2 and CaO act as network modifiers.[14] The ensuing vitrification process during cooling could result in pinned locations where subsequent accumulation of particles proceeds via hydrodynamic mechanism. The final microstructures show the surfaces composed of star shaped $CaTiO_3$ (from $CaO-TiO_2$ interaction) all around and CaP rich cuboids in a circular pattern arrangement. As discussed earlier with reference to the $CaO-TiO_2$ phase diagram the nucleation of $CaTiO_3$ at regions rich in CaO indicates lager temperature window across which particles can move freely before they finally solidify (Fig. 4, 500 °C separation between liquidus and solidus). This feature provides opportunity for particles to move around and time to settle during assembly. At faster laser processing speeds due to abundance of CaP material and ideal thermal gradients in the 1500–2500 K temperature window, they have ample opportunity to orient and self-assemble. The formation of this kind of multiscale assembly is very interesting from a biocompatibility perspective. Tan and Saltzman[3] reported that surfaces patterned at multiscale provide enhanced osteointegration. In the present work it has been observed that there has been a hierarchical evolution of morphological features driven primarily by self-assembly.

IV. CONCLUSIONS

CaP based composite coatings are obtained on Ti alloy surface via laser processing. The morphological and chemical evolutions of these coatings are dictated by laser processing speeds and subsequent temperatures attained. Of particular interest are the coatings observed at higher laser processing speeds that have evolved into multiscale features. Based on the current understanding it appears that the self-assembly plays an important role during this hierarchical evolution. Quadrupolar multipoles influenced cuboid particle formation under ideal temperature and chemical environments. A higher level of assembly of these cuboids during

Author complimentary copy. Redistribution subject to AIP license or copyright, see http://jap.aip.org/jap/copyright.jsp

subsequent process resulted in ringlike structure. Such hierarchically evolved structures are expected to provide enhanced biocompatibility.

[1]M. A. Lopez-Heredia, P. Weiss, and P. Layrolle, J. Mater. Sci.: Mater. Med. 18, 381 (2007).
[2]A. L. Oliveira, J. F. Mano, and R. L. Reis, Curr. Opin. Solid State Mater. Sci. 7, 309 (2003).
[3]J. Tan and W. M. Saltzman, Biomaterials 25, 3593 (2004).
[4]A. Kurella and N. Dahotre, Acta Biomater. 2, 677 (2006).
[5]A. Kurella and N. D. Dahotre, J. Biomater. Appl. 20, 5 (2005).
[6]S. P. Harimkar, A. N. Samant, and N. B. Dahotre, J. Appl. Phys. 101, 054911 (2007).
[7]S. P. Harimkar, A. N. Samant, A. A. Khangar, and N. B. Dahotre, J. Phys. D: Appl. Phys. 39, 1642 (2006).
[8]S. Dyshlovenko, B. Pateyron, L. Pawlowski, and D. Murano, Surf. Coat. Technol. 179, 110 (2004).
[9]M. Boivineau, C. Cagran, D. Doytier, V. Eyraud, M.-H. Nadal, B. Wilthan, and G. Pottlacher, Int. J. Thermophys. 27, 507 (2006).
[10]O. Guillot-Noël, R. G. San Roman, J. Perrière, J. Hermann, V. Craciun, C. B. Leborgne, and P. Barboux, J. Appl. Phys. 80, 1803 (1996).
[11]F. P. Incropera and D. P. Dewitt, *Fundamentals of Heat and Mass Transfer* (J. Wiley, New York, 2002).
[12]R. C. De Vries, R. Roy, and E. F. Osborn, J. Phys. Chem. 58, 1069 (1954).
[13]L. Sun, C. C. Berndt, and C. P. Grey, Mater. Sci. Eng., A 360, 70 (2003).
[14]M. Chiang, D. P. Birnie III, and W. D. Kingery, in *Physical Ceramics, Principles for Ceramics Science and Engineering*, edited by M. Chiang, D. P. Birnie III, and W. D. Kingery (Wiley, New York, 1997).
[15]P. A. Kralchevsky and N. D. Denkov, Curr. Opin. Colloid Interface Sci. 6, 383 (2001).
[16]K. D. Danov, P. A. Kralchevsky, B. N. Naydenov, and G. Brenn, J. Colloid Interface Sci. 287, 121 (2005).
[17]P. A. Kralchevsky, N. D. Denkov, and K. D. Danov, Langmuir 17, 7694 (2001).
[18]J.-B. Fournier and P. Galatola, Phys. Rev. E 65, 031601 (2002).
[19]S. Toyoda, S. Fujino, and K. Morinaga, J. Non-Cryst. Solids 321, 169 (2003).
[20]G. D'Anna and G. Gremaud, Nature (London) 413, 407 (2001).

Author complimentary copy. Redistribution subject to AIP license or copyright, see http://jap.aip.org/jap/copyright.jsp

Laser-Induced Functionally Textured Bio-Coating*

Anil Kurella and Narendra B. Dahotre

Surface engineering continues to play an important role in improving the biocompatibility of hard tissue replacements. Recently, the hierarchical organization of natural biomaterials has been realized as an important property that guides the attachment of tissues, cells, and proteins at various levels of interactions. Currently, researchers are focusing interest on developing hierarchical bioactive structures for effective osseointegration. The present effort discusses a multi-textured calcium-phosphate-based coating produced by laser surface engineering. The chemical and morphological evolution of these bioactively textured coatings was studied along with biomimetic precipitation of calcium phosphates when immersed in simulated body fluids.

INTRODUCTION

Metallic materials such as titanium and its alloys are frequently considered for load-bearing orthopedic applications.[1] However, it is widely perceived that the nature of interaction of the implant surface with its surrounding environment plays an important role in the good fixation of these implants with the surrounding tissue. Traditionally, researchers have focused on developing surfaces that are osseoconductive using coatings or texturing operations. In recent years, however, with improved understanding of the multi-scale nature of biological materials through hierarchical evolution, efforts are being concentrated in producing surfaces that are not only bioactive but also textured in a multi-scale nature.[2]

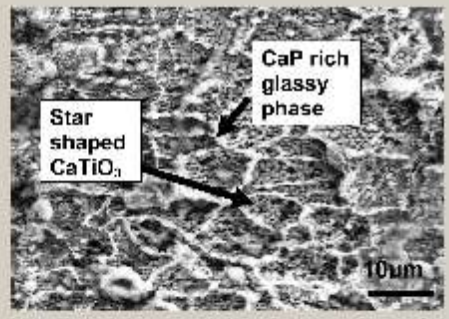

Figure 1. The surface morphology of a laser surface coated sample (processing speed 200 cm/min.).

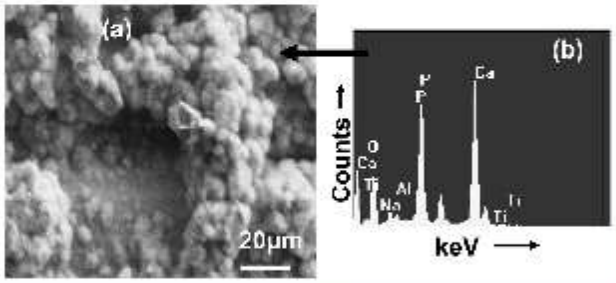

a b

Figure 2. (a) The surface morphology after 14 days dissolution in SBF; (b) an EDS taken on the globular-shaped particles precipitated after SBF dissolution1.

LASER PROCESSING, ANALYSIS, AND TESTING

In this study, Ti-6Al-4V alloy coupons (50 mm x 100 mm x 3 mm) were polished to a roughness of 0.5 µm followed by washing in water and rinsing in acetone. Calcium phosphate tribasic ($Ca_3(PO_4)_2$) powder obtained from Fisher Scientific was mixed with water-based organic solvent and was sprayed onto these coupons using an air spray gun to achieve a consistent thickness of 40 ± 5 µm. With a continuous-wave Nd:yttrium aluminum garnet laser (a wavelength of 1,064 nm) beam (5 mm x 1.5 mm size in cross section at the focus), the sprayed samples were processed at 850 W power with processing speeds ranging from 100 cm/min. to 300 cm/min. Using Philips Norelco X-ray diffractometer, the laser-processed surfaces were characterized with copper Kα radiation operating at 30 kV and 20 mA. The surfaces were scanned in the diffraction range of 20° to 100° with a step increment of 0.02° and a count time of 1 s. The surface morphology was studied using a JEOL scanning-electron microscope (SEM). An energy-dispersive spectroscopy (EDS) attached to the SEM was used for chemical microanalysis. In order to

examine the precipitation of hydroxyapatite (HA) as an indirect indication of biocompatibility of modified surface, the laser-surface-modified samples were immersed in conventional simulated body fluid (SBF). The SBF was prepared as per standard procedures reported in literature.[3] The sample was immersed for 14 days in SBF maintained at a constant pH of 7.4 at 370°C and refreshed every 24 h. Periodically, the samples were taken out of the solution and dried prior to characterization using SEM and x-ray diffraction (XRD) analyses for morphological and chemical evolution of precipitates during SBF immersion.

LASER SURFACE MORPHOLOGY

The surfaces produced by laser-textured coatings exhibited a multi-scale and multiphase nature. The morphology of the laser-processed coating consisted of a periodic arrangement of star-like phases uniformly distributed inside a self-assembled cellular structure (Figure 1). The elemental analysis based on electron-dispersion spectroscopy (EDS) revealed that the star-like structure is titanium rich and Ca-P deficient whereas the cellular structure is a Ca-P rich region. Furthermore, XRD analysis predicted the presence of CaO, α-TCP (tri calcium phosphate), $CaTiO_3$, and TiO_2, along with titanium phase in the coating.[4] The star-like structures are about 1 μm in average size whereas the cellular structures ranged in diameter from 2.5 μm to 10 μm. The evolution of a multiple number of such phases is highly likely to happen during laser processing due to prevailing near-non-equilibrium or non-equilibrium thermodynamic conditions. The detailed discussion on evolution, distribution, and chemical nature of these multiple phases/precipitates is presented elsewhere.[4] The presence of such a multiphase and multi-scale coating can be beneficial for better osseoconductivity and for development of the chemistry in a physiological environment that is biocompatible for tissue growth.

SBF-INDUCED SURFACE MORPHOLOGY

Figure 2 shows the morphology of the laser-coated surface after immersion in SBF for 14 days. Electron-dispersion spectroscopy (EDS) on the globular

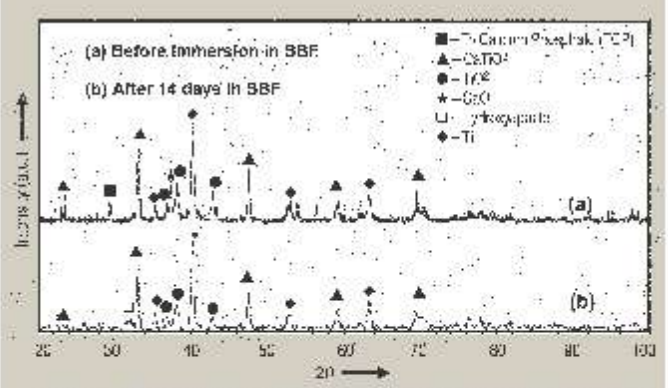

Figure 3. A comparison of XRD spectra from laser-processed samples before and after immersion in SBF for 14 days.

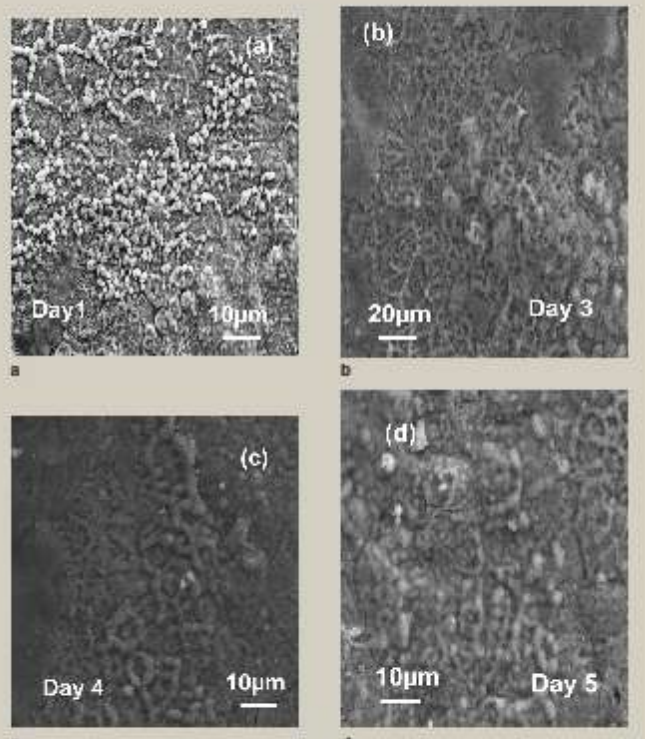

Figure 4. The sequential evolution of morphology during immersion in SBF. (a) As-laser-processed surface on day 1 before immersion in SBF. A network of cuboidal shaped particles exist on the surface. (b) On day 3, the cellular structure clearly evolved after dissolution of the CaO from the surface. Note that the $CaTiO_3$-rich star-like structures exist inside each of these cellular structures. (c) After day 4, the cellular structure coarsens with the precipitation of HA. (d) Nucleation and precipitation of HA takes place clearly all along the cellular network and on the $CaTiO_3$-rich star-shaped particles inside these cellular structures.

surface features clearly showed that the region is rich in calcium and phosphorous, which are the components of HA. A comparison of the XRD spectra of the surfaces before and after SBF immersion clearly indicated the initiation of the evolution of HA with dissolution of phases, CaO and TCP (Figure 3).

In order to understand the sequence of steps evolved in the laser-processed surface immersed in SBF, SEM coupled with EDS was employed to regularly evaluate the morphology and its chemical nature. Figure 4 provides a pictorial description of the events. Based on XRD analysis it is clear that the surface of the laser-processed sample immersed in SBF for initial few days (<3 days) had the same composition as an as-laser-processed (prior to immersion) sample that consisted of a mixture of such phases as TCP, $CaTiO_3$, and CaO along with titanium (Figures 3 and 4a). However, soon after the first few days (>3 days) of SBF immersion of the laser-processed sample, most of the CaO 53(6):685-93 dissolved in the solution, leaving the porous surface structure comprised of a cellular glassy network of CaP-TiO_2 and the star-like $CaTiO_3$ inside these networks (Figure 4b), a morphology similar to that in the as-laser-processed sample (Figure 1). The dissolution of CaO is in line with the existing understanding that among all the products of high-temperature reaction, the order of dissolution decreases from CaO to tetra TCP, and further to TCP.[5] As the days progressed (≥4 days) it appeared that the cellular network served as the locations for precipitation of HA (Figure 4c). This indicated that the presence of CaP-TiO_2 along with $CaTiO_3$ served as nuclei for the controlled precipitation of HA (Figure 4d), thus reinforcing the belief that the multi-scale textured surface could provide improved biocompatibility. Although the formation of such HA precipitates on a laser-modified surface is an indirect indication of biocompatibility of the surface, the authors are currently involved in translational research in collaboration with researchers in the biomedical and medical fields to conduct in-vitro studies on these samples. Detailed results will be the subject of future publications.

ACKNOWLEDGEMENTS

Research incorporated as examples in this paper has been supported in part by several projects funded by the Southwest Consortium for Environmental Research and Policy and a Mr. and Mrs. MacIntosh Murchison Endowed Chair. The help of Micah Baquera, Erika Esquivel, and others in creating selected SEM images utilized in this paper is especially acknowledged.

References

1. A. Kurella and N.B. Dahotre, "Surface Modification for Bioimplants: The Role of Laser Surface Engineering," *J. Biomater. Appl.*, 20 (2005), pp. 5–50
2. J. Tan and W.M. Saltzman, "Biomaterials with Hierarchically Defined Micro- and Nanoscale Structure," *Biomaterials*, 25 (2004), pp. 3593–3601.
3. A. Oyane et al., "Preparation and Assessment of Revised Simulated Body Fluids (2003), *J. Biomed. Mater. Res. A*, 65 (2), pp. 188–195.
4. A. Kurella and N.B. Dahotre, "Laser Induced Hierarchical Calcium Phosphate Structures," *Acta Biomaterialia* (2006), in press.
5. O. Grassmann and P.B. Helmann, "Compositional and Microstructural Changes of Engineered Plasma-Sprayed Hydroxyapatite Coatings on Ti6Al4V Substrates during Incubation in Protein-Free Simulated Body Fluid," *J. Biomed. Mater. Res.* 53 (6) (2000) pp. 685–693.

Anil Kurella is with Intel Corporation, Portland, Oregon, and formerly with the Department of Materials Science and Engineering at the University of Tennessee in Knoxville, Tennessee. Narendra B. Dahotre is with the Department of Materials Science and Engineering at the University of Tennessee in Knoxville, Tennessee.

For more information, contact Narendra B. Dahotre, Department of Materials Science and Engineering, University of Tennessee, Knoxville, TN 37996; (865) 974-3609; fax (865) 974-4115; e-mail ndahotre@utk.edu.

J Mater Sci: Mater Med (2006) 17: 565–572
DOI 10.1007/s10856-006-8941-3

Laser induced multi-scale textured zirconia coating on Ti-6Al-4V

Anil Kurella · Narendra B. Dahotre

Received: 3 April 2005 / Accepted: 9 August 2005
© Springer Science + Business Media, LLC 2006

Abstract A textured coating of zirconia on Ti-6Al-4V alloy was produced using pulsed laser based processing technique. Scanning electron microscope observations coupled with fractal analysis revealed the multi-scale nature of the textured coating. Both stylus based profilometric measurements and fractal analysis indicated non-linear nature of the relationship between laser processing speed at constant pulse frequency (10 kHz) and roughness of the textured coating. The textured coatings produced with all the three processing speeds (40, 160, 290 cm/min) were fractal over certain length scales. Processing at 40 cm/min resulted in structures that are fractal across a large number of length scales where as higher processing speeds resulted in fractality over fewer length scales. The processing speed influenced the zirconia content in the coating and the phase transformation within Ti-matrix of the coating. Within the coating, while zirconia content decreased the amount of retained β-Ti increased with increase in processing speed. Such physical and chemical transformations are desired in a titanium bio-implant for effective contact with protein, cells and tissues at various length scales and its effective chemical performance in bio-environment.

A. Kurella · N. B. Dahotre
Department of Materials Science and Engineering,
The University of Tennessee, Knoxville, Tennessee 373996, USA

N. B. Dahotre (✉)
Department of Materials Science and Engineering,
The University of Tennessee, Knoxville, Tennessee 373996, USA;
Materials Processing Group, Metals and Ceramics Division,
Oak Ridge National Laboratory, Oak Ridge, Tennessee 37831,
USA
Tel.: 865-974-3609
e-mail: ndahotre@utk.edu

1. Introduction

Ti and its alloys are excellent biomaterials because of their good biocompatibility and corrosion resistance. The spontaneous formation of a passive TiO_2 layer provides the necessary inertness and biocompatibility [1]. However this TiO_2 layer has inferior mechanical properties and fractures easily under wearing conditions. This results in detrimental accumulation of wear debris and eventual ion release into biosystems [2]. To overcome this problem and to provide effective osseointegration hard and wear resistant bioceramic materials are coated on implant surfaces. Bioceramics like zirconia have good fracture toughness, bending strength apart from excellent biocompatibility and have been coated on Titanium alloys [3, 4].

The other surface engineering processing for implant surfaces involves texturing the surfaces to make the tissues grow into the surface and hold them better. Physical texturing is now recognized to play a major role in the way cells respond to surfaces and thus great deal of studies were dedicated to correlate the proliferation, adhesion, migration and differentiation [5, 6]. Surfaces textured with micro and nano features have been to some extent successful in osseointegration [5, 6]. At this point it is worth remembering that in nature materials are organized at various length scales ranging from nano to micro level. Thus a synthetic material designed to survive and effectively integrate into a bio environment might be expected to show compatibility at multi-scales rather than at a single level. Hence the present emphasis is to develop materials that are functionally active and hierarchically organized at various length scales. So far the efforts to produce integrated micro to nano features for bio applications are limited and rare [5]. There exist many techniques to provide either efficient coatings or textures but so far there has been

no effort to effectively integrate both coatings and texture together to produce textured coatings [6].

This paper is focused on the concept of simultaneous coating and texturing using a laser source. The use of laser for surface engineering offers great flexibility and presents manifold advantages [6]. By carefully modulating the laser optics and processing parameters it is possible to produce tailor made surfaces for various applications [7].

However, a major problem associated with engineered surfaces like coatings or textures for bio applications is their physical characterization. Generally, a surface is characterized by a large number of length scales mutually superimposed onto one another. The arithmetic average roughness, R_a, or the root mean square average, R_q (rms), commonly used to characterize the surface roughness do not convey information on the range of length scales over which different topographic features exist. The roughness measuring instruments often provide different values for surfaces at different scales depending on the resolution and the filtering capabilities of the instrument at that length scale. Therefore, surfaces should be characterized in a way such that the structural information at all scales is retained [8]. Over the last few decades researchers have tried to characterize multi-scaled surfaces using the mathematical concept of fractals which are invariant with respect to scale. Fractals are unique because of their extreme fragmentation bounded by non–euclidean geometry instead of topological dimensions. These fractals are quantified by fractal dimension, D_f, which permits to distinguish fractals at any scale.

Typically the calculation of fractal dimensions of engineering surfaces is a complicated process since it involves not only a number of mathematical models but also surface topography image processing. These fractal dimension calculators are built into commercial surface instruments, such as atomic force microscope (AFM) and Talysurf PG I [9]. Apart from being costly the fractal dimension calculators attached with these instruments cannot be used to calculate the surface fractal dimension of data acquired by other equipments. In light of this, the present paper reports a laser based technique to simultaneously coat and texture surfaces with potential for bio applications and deals with simple fractal based analysis to characterize surfaces for their multi-scale nature using a free public domain software called ImageJ (available with National Institutes of Health, USA).

2. Materials and methods

Ti alloy (Ti-6Al-4V) plates were cut into small coupons (25 mm × 25 mm × 3 mm) using Techcut10™ Allied High Tech Products Inc. The starting powders zirconia (ZrO_2) (stabilized with 5.4 wt% Y_2O_3) were obtained from Goodfellow Cambridge Limited, England. The mean particle size of zirconia powder used in this process was less than 1 μm. The coupons were sand blasted and rinsed with acetone. Using an air spray gun the zirconia powder mixed with a water based organic solvent was sprayed onto these coupons to achieve a uniform thickness of 40 μm.

In this work, a pulsed Nd:YAG laser (Trumpf Laser and VectorMark workstation) was employed. This laser emits infrared radiation of wavelength 1064 nm. With a focus diameter of 40 μm it is capable of delivering a fundamental-mode beam quality with pulse frequencies ranging from 1–60 kHz. In the present efforts, the samples were processed with 25 W power at frequency of 10 kHz for three different traverse speeds of 40 cm/min, 160 cm/min and 290 cm/min. For the purpose of covering the entire surface of the sample the overlapped laser pulses were laid in a linear track and such successive linear tracks were laid with a fixed overlap between them. The overlap between successive passes was 20% whereas the successive laser pulsing spots in a linear track resulted in an overlap of 95%, 80 and 70% for processing at 40 cm/min, 160 cm/min and 290 cm/min respectively.

Using Philips Norelco X-ray diffractometer the starting powders as well as the coatings were characterized with Cu Kα radiation operated at 30 kV and 20 mA. The diffraction range was from 20° to 100° with a step increment of 0.02° and a count time of 1 s. Surface morphology was evaluated using a Hitachi-3500 scanning electron microscope (SEM) (Hitachi, Tokyo, Japan). The images were recorded at various magnifications and were further processed using conventional image processing techniques. Each of these images were converted from spatial domain of brightness to a frequency domain components using fourier transforms, filtered from noises and then thresholded to convert them into a binary digital image. A parameter called fractal dimension was calculated from these binary images by implementing a box counting technique using macros available in the public domain software ImageJ available with National Institutes of Health (NIH) USA.

Surface roughness of the coated samples was measured using a Mahr Federal profilometer. This is equipped with a stylus based tip which traverses the surface following the local irregularities. The motion of the stylus tip is recorded by a photoelectric cell and amplified. The stylus tip has a radius of 2 μm. In each measurement the tip traces a length of 5.6 mm and different roughness parameters like Ra (arithmetic mean deviation of the roughness profile), Rz (mean peak to valley height), Rmax (maximum roughness depth) were recorded. Six different profiles were analyzed for each sample and the average value was reported.

3. Results and discussions

3.1. Phase evolution in coating and substrate

Since laser processing is energy intensive operation variation in processing speed (at constant pulse frequency of 10 kHz) is expected to influence the total heat input and subsequently the phases evolved in the final material. X-ray diffraction (XRD) analysis was, therefore, carried out to evaluate the changes. Fig. 1a shows the overlaid XRD spectra of zirconia powder, Ti-alloy (Ti-6Al-4V) substrate along with the coatings. The XRD analysis of zirconia powder indicated the existence of primitive tetragonal phases. Two small peaks at 28.1° and 30.6° indicated the presence of monoclinic phase in the powder. The coatings on Ti-6Al-4V showed the existence of zirconia peaks along with the substrate peaks. As the speed of the laser processing decreased the intensity of {111} peak corresponding to retained zirconia on the surface increased (Fig. 1a). The variation in the intensity of {111} peak can then be semi-quantitatively related to the variation

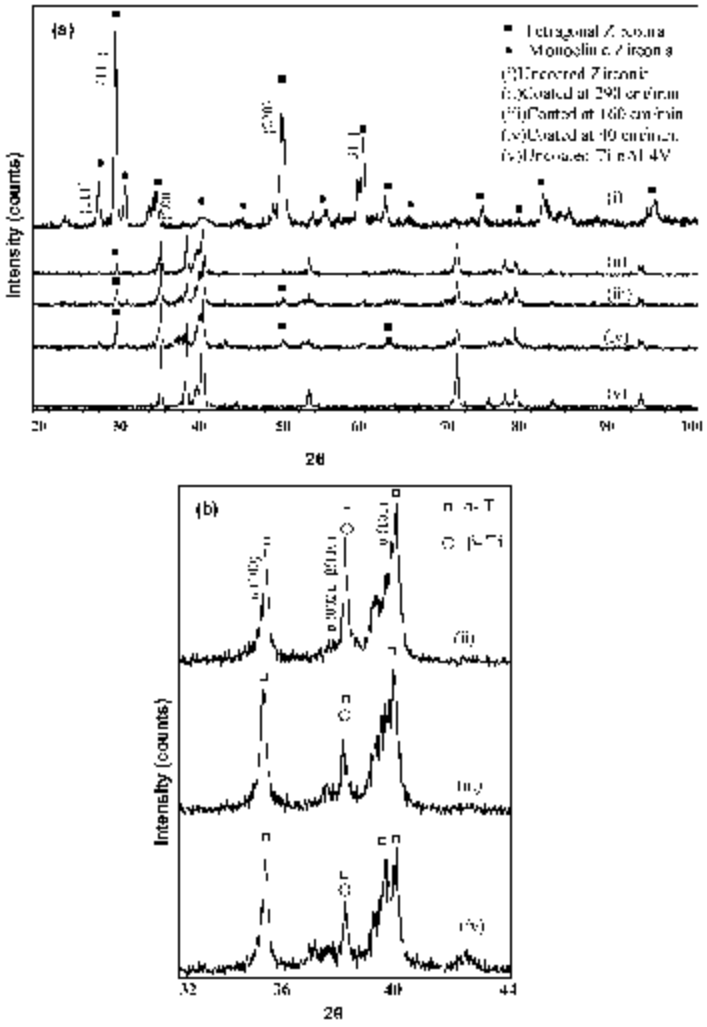

Fig. 1 XRD spectra for (a) Zirconia powder, and coatings produced at various speeds and (b) coatings scanned between 32°–44° for detailed phase identification.

in amount of retained zirconia. Furthermore, as expressed earlier, the total heat input (at constant pulse frequency of 10 kHz) is a function of processing speed and, therefore, a function of maximum temperature attained during the process [10, 11]. As the processing speed increases, the interaction time of laser beam with and subsequently the maximum temperature attained by substrate decrease. Thus the level of maximum temperature is expected to influence the characteristics of mixing and bonding between the coating precursor and the melted portion of substrate material [10, 12]. It is, therefore, in the present work the amount of retained zirconia in the laser modified region expected to decrease as the processing speed increased which may be the major cause for low intensities of zirconia peaks at higher processing speeds.

At the same time the variation in speed also offered possibilities for various Ti-alloy phase transformations within the laser modified surface region. A detailed observation of this was carried out by running new X-Ray scans from 32°–44° where intense and major peaks of Ti exist (Fig. 1b). The speed of laser processing is expected to influence the rate of cooling cycle [10]. Accordingly, processing at 290 cm/min would set up extremely high thermal gradients compared to 40 cm/min. Under the condition of such high thermal gradient the kinetics of phase transformation is greatly influenced and can lead to various events such as but not limited to incomplete phase transformation and formation of unconventional phases [13–16]. Such changes are evident from the XRD spectra presented in Fig. 1a and 1b. In Ti-6Al-4V at high temperature (>1100°C) β-Ti phase exists and during the cooling from these high temperatures the β-Ti tries to transform into α-Ti [17]. In the contrast, in the present work the amount of retained β-Ti seemed to have increased with processing speed suggesting that sufficient time was not available for it to transform into α-Ti. Using a direct comparison of the X-ray diffraction spectra the ratio of retained β-Ti to α-Ti were determined [18]. These values were plotted as a function of processing speed in Fig. 2. The retained β-Ti is harder, stronger and less ductile [17]. The alpha phase generally present in such a rapid quenching process is commonly referred to martensitic α [17]. The formation of this martensitic α is associated with distortion of the lattice resulting in a strained material. This α martensite is usually hard, tough and stronger and possesses better fatigue properties than α-Ti, which is relatively tough, soft and ductile [17]. Thus in the present experiments the distribution of martensitic α-Ti phase in β-Ti matrix (the ratio of retained β-Ti to α-Ti) is expected to result in a material that is hard and tough with improved mechanical properties compared to the untreated surface. This observation is in line with the observations made by the authors in their earlier work on Ti-alloys where laser induced microstructures seemed to have exhibited enhanced physical (tribological) and chemical (corrosion) properties in

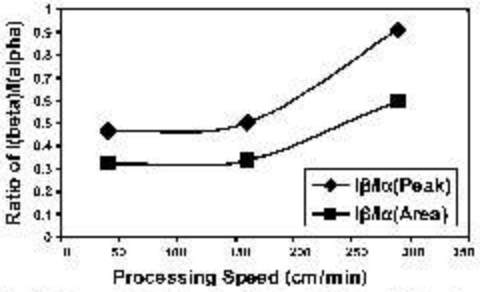

Fig. 2 Figure showing the ratio of retained β-Ti to α-Ti at various laser-processing speeds.

simulated bio-environment [19, 20]. Such manipulation for type and amount of phase within the coating for improved wear and corrosion properties is extremely important in tailoring the properties for bio applications such as hard tissue implants.

It appeared that for samples processed at 40 cm/min there were multiple sub peaks corresponding to {101} class of reflections in the XRD spectrum (Fig. 1b). This could be the effect of cyclic thermal heating and cooling due to successive passes that in turn set up varying thermal gradients in previously melted tracks. Since β-Ti to α-Ti transformation is mono-variant in nature, the phases precipitated at different cooling rates are expected to have different morphologies which may result in different levels of residual stresses leading to the formation of α-Ti phases with different 'c' and the same 'a' lattice parameters [16]. On the contrary, when the laser processing speed increases sufficient time is not available for formation such different α-Ti phases which is evident from a few corresponding well defined multiple peaks in XRD spectra (Fig. 2b).

3.2. Morphological evaluation of textured coating

The chemical phase transformations induced during laser processing have been shown to influence the topographical modifications [21]. The following section deals with characterization of surface topography and its correlation with processing conditions. The surface morphology was influenced by the processing speed (at constant pulse frequency of 10 kHz) as can be seen from the scanning electron micrographs in Fig. 3. The processing speed influences the laser beam interaction time (total heat input) with the substrate and also the distance between the subsequent laser pulses (an overlap of 95%, 80 and 70% for processing at 40 cm/min, 160 cm/min and 290 cm/min respectively). These parameters together greatly influence the surface morphology. As seen in Fig. 3, each pulse produces a crater of solidified material with trough around the edge and relatively flat region inside

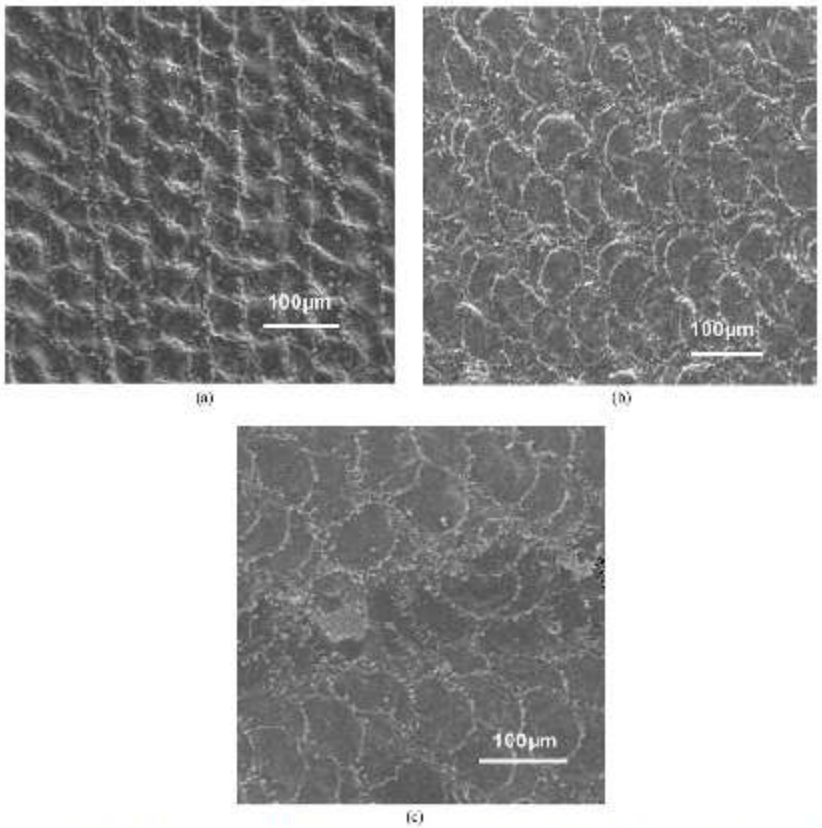

Fig. 3 Low magnification images of textured Ti-6Al-4V coupons processed at the speed of (a) 40 cm/min (b) 160 cm/min (c) 290 cm/min.

of the crater. The decrease in processing speed increases the overlap between subsequent pulses (craters), which further increases the trough region (Fig. 3a) and affects roughness of the processed surface region. However, repeated pulses in a linear track followed by several such linear tracks in overlapped manner (for coverage of the entire surface) change thermal gradients in the molten material which in turn can affect the nature and amount of trough and flat regions after solidification. Such situation can provide complex relationship between processing parameters and roughness of the surface.

Furthermore, the textures when closely observed at higher magnifications showed multi-scaled features. Fig. 4 included the image at higher magnification of the surface of sample processed at 40 cm/min that revealed a multi-scale texture. Similar observations were recorded for samples processed at other speeds (160 cm/min and 290 cm/min). The speed of laser processing coupled with number of pulses per unit area seems to have influenced the outcome of the process. In order to interpret these features and quantitatively explain them, profilometer based roughness characterization was carried out. Although the profilometric measurements do not provide any idea about multi-scale nature of morphological features on the surface, they are very helpful in quantifying the roughness due to such features at a given single scale.

The variation in calculated roughness values for the three different speeds of operation is presented in Fig. 5. It can be observed that processing at 160 cm/min provides higher roughness parameters compared to the other conditions. The two processing parameters that influence the nature of the surface produced are the number of pulses per unit area and the repeated linear passes during the laser processing operation. The low roughness values for the sample processed at 40 cm/min can be explained based on the softening of the

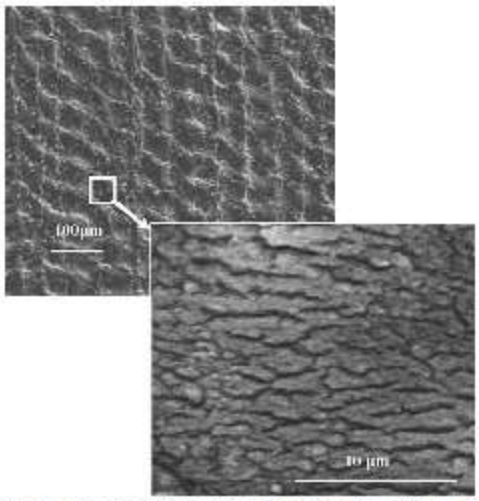

Fig. 4 Multi-scale features delineated with scanning electron microscopy observation for the sample processed at 40 cm/min.

peaks due to repeated passes of the laser source as shown in Fig. 6a. Apart from this the number of pulses per unit area increases as the speed of processing decreases due to which the temperature of the peaks is repeatedly maintained at higher level resulting in re-melting of the solidified peaks that lead to a smoothening effect on the surface. The smoothening effect decreases and roughness increases as the processing speed increases. However, at highest processing speed corresponding to 290 cm/min lower roughness can be attributed to the fact that the numbers of pulses per unit area are few and their degree of overlap is small due to which the topography consisted of alternate smooth and rough areas as presented in Fig. 6b.

As described in earlier sections the laser processing resulted in multi-scale structures (Fig. 4) and thus conven-

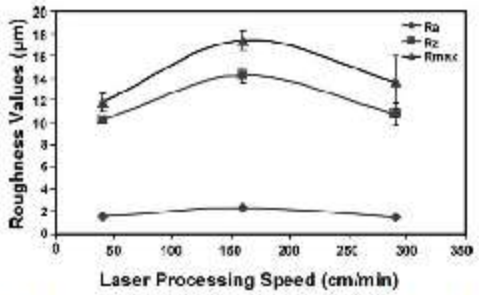

Fig. 5 Roughness parameter (with standard deviations) as function of laser processing speed.

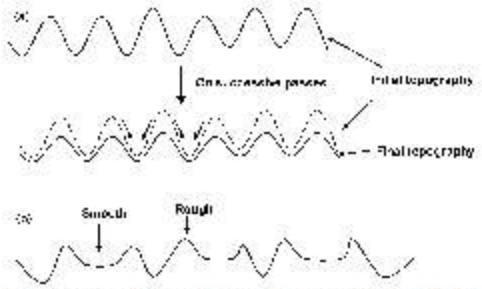

Fig. 6 (a) Schematic showing a possible smoothening effect at low processing speed of 40 cm/min. (b) Alternate smooth and rough surface produce due to past laser processing at 290 cm/min.

tional surface characterization parameters like Ra, Rz limit the range of observations to a single scale. In order to realize the multi-scale level of the features, a fractal-based approach was adopted. The fractal dimensions were determined from the SEM images processed using the macros based on the box counting technique in the software called ImageJ. The series of operations carried out to determine the fractal dimension is schematically shown in Fig. 7.

One of the most common methods for calculating the fractal dimension of a self-similar fractal is the box counting method. This process involves covering a structure with boxes of length 'l' and counting the number of boxes 'N(l)' required to cover the structure. The fractal dimension 'D' is given by

$$D = -\lim[\log_{10} N(l)]/\log_{10}(l)] \text{ as } l \to 0$$

where N(l) is number of boxes needed to completely cover the structure. D corresponds to the slope of the plot $\log_{10}$ N(l) versus $\log_{10}$ (l). The next most important parameter to be studied is the range of scales over which the micro features continue to show fractal nature. In order to predict this, the fractal dimensions were calculated from SEM images processed at different magnifications such as presented in Figs. 3 and 4. Since all the images were obtained under similar operating conditions and all had the same digital resolution the length per pixel was calculated for each magnification and this forms the basis for comparing the fractal dimensions at different magnifications as shown in Fig. 8. From this graph it can be concluded that all the three processing conditions show fractal properties at certain length scales. While processing at 40 cm/min resulted in structures that are fractal across a large number of length scales, faster processing conditions seems to have resulted in fractal nature over fewer length scales with fractality at two different length scales for the processing speed of 160 cm/min within the range of magnification employed for image observations/processing

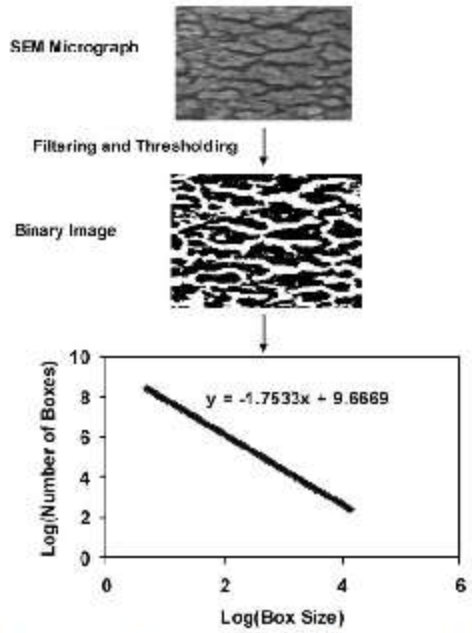

Fig. 7 Sequence of various image processing operations involved in fractal dimension determination. The slope of the log –log plot in the schematic shown corresponds to the fractal dimension (box counting technique).

in the present work. The upper limit of such magnification was 2 μm/pixel and it was dictated by the radius of the stylus tip (2 μm) on the profilometer used in roughness measurements.

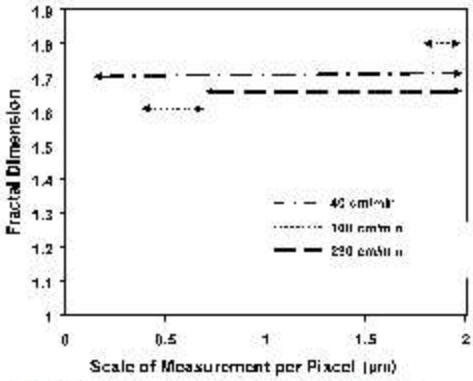

Fig. 8 Variation in fractal dimension at various length scales.

Table 1 Fractal dimension at different processing speeds

Speed of Laser Processing	Fractal Dimension at Length Scale of 2 μm Per Pixel
40 cm/min	1.7427
160 cm/min	1.8566
290 cm/min	1.6831

In light of the above findings, exploration of the relationship between fractal dimensions and roughness was considered important. Hence the fractal dimensions obtained at length scales of 2 μm (comparable to that of stylus tip dimension used in roughness measurements) are shown in Table 1. As can be seen, the variation in fractal dimensions is analogous to their roughness variation establishing the fact that fractal dimension can be correlated with general nature of roughness measurements and the fractal based predictions are reliable for different length scales. Although in the present case, such correlation was possible only at one length scale (2 μm), it is expected to follow appropriate trend at other length scales if and when roughness measurements are conducted at those scales. Roughness measurements at much finer length scales (< 2 μm) and determination of their relationship with fractal dimensions is the goal of future efforts. Such a fractal based description is useful in modeling the outcome laser processing to tailor multi-scaled structures at predetermined processing conditions.

The thickness of these laser induced coatings was about 40 pμm and based on initial scratch testing these coatings appeared fairly adherent. However, the authors wish to determine the adhesive strength of coatings using a technique similar to that described by Nowotny *et al.*, who investigated the fused oxide ceramics on metallic substrates using a high power CO_2 laser [4]. In addition to evaluation of coating adhesion, the authors intend to evaluate the response of coating in bio-environment for protein, cell, and tissue integration along with corrosion response. These results will be presented in due course of time. Since the physical structure of a biomaterial is now considered a key factor in determining cellular responses and further adhesion and integration into bioenvironment, laser based processing can be experimented with to tailor organized structures for direct biomedical applications

4. Conclusions

In the present work it has been successfully shown that lasers can be used to coat and texture simultaneously to produce surfaces that are hierarchically integrated and organized at multiple scales. The amount of ziconia retained as coating and the kinetics of phase transformations within the matrix of

coating area are influenced by the speed of laser processing. The retained β-Ti phase increased and retained Zirconia decreased with the speed of processing. The number of pulses and successive laser passes seemed to influence the roughness of the final surface. A fractal-based approach was used to interpret the multi-scaled surfaces and has been successfully correlated with the surface roughness values. Processing at 40 cm/min resulted in coating rich in zirconia and surface being fractal over wider range of length scales compared to other processing speeds.

Acknowledgments The authors acknowledge the assistance from Fred Schwartz and Doug Warnberg of the Center for Laser Applications at the University of Tennessee Space Institute in laser processing the samples.

References

1. G. HASAN and Ç. HÜSEYIN, *Biomaterials* **25** (2004) 3325.
2. H. GULERYUZ and H. CIMENOGLU, *Surf. Coat. Technol.* **192** (2005) 164.
3. Y. YANG, J. L. ONG and J. TIAN, *Biomaterials* **24** (2003) 619.
4. S. NOWOTNY, A. RICHTER and K. TANGERMANN, *J. Thermal Spray Technol.* **8** (1999) 258
5. J. TAN and W. M. SALTZMAN, *Biomaterials* **25** (2004) 3593.
6. A. KURELLA A and N. B. DAHOTRE, *J. Biomat. Appli.* (2005) Accepted.
7. A. C. DUNCAN, F. WEISBUCH, F. ROUAIS, S. LAZARE and CH. BAQUEY, *Biosensors and Bioelectronics* **1** (2002) 413.
8. P. F CHAUVY, C. MADORE C and G. LANDOLT, *Surf. Coat. Technol.* **110** (1998) 48.
9. C. Q. YUAN, J. LI, X. P. YAN and Z. PENG, Wear **255** (2003) 315–326
10. P. KADOLKAR, H. WANG, T. R. WATKINS and N. B. DAHOTRE, *International J. of Adv. Manuf. Technol* **23** (2003) 350.
11. S. NAYAK, H. WANG, and N. B. DAHOTRE, *Materi. Sci. Technol.* **20** (2004) 1609.
12. N. B. DAHOTRE, P. KADOLKAR and S. SHAH, *Surf. Interface Analysis* **31** (2001) 659.
13. A. SINGH and N. B. DAHOTRE, *Metall. Mater. Transact. A* **36** (2005) 1.
14. A. AGARWAL and N. B. DAHOTRE, *Metall. Mater. Transact. A* **31** (2000) 401.
15. L. R. KATEPELLI, A. AGARWAL and N. B. DAHOTRE, *Appl\ied. Surf. Sci.* **153** (1999) 65.
16. S. MALINOV, W. SHA, Z. GUO, C. C. TANG and A. E. LONG, *Materials Characterization*, **48** (2002) 279.
17. S. ABKOWITZ, J. J. BURKE and R. H. HILTZ JR., in "Titanium in Industry" (D. Van Nostrand Company, Inc. New York, 1955) p. 50.
18. B. D. CULLITY, in "Elements of X-Ray diffraction" (Addison-Wesley Publishing Company, Inc. Philippines, 1978) p. 397.
19. R. SINGH, M. MARTIN and N. B. DAHOTRE, *Surface Engineering*, (2005), Accepted for publication.
20. R. SINGH, A. KURELLA and N. B. DAHOTRE, *J. Biomat. App.*, (2005), Accepted for publication.
21. F. GUILLEMOT, F. PRIMA, V. N. TOKAREV, C. BELIN, M. C. PORTE-DURRIEU l, T. GLORIANT, CH. BAQUEY and S. LAZARE, *Appl. Phys.* **A 77** (2003) 899.

Available online at www.sciencedirect.com
ScienceDirect
Acta Biomaterialia 2 (2006) 677–683
Acta BIOMATERIALIA
www.actamat-journals.com

Laser induced hierarchical calcium phosphate structures

Anil Kurella [a], Narendra B. Dahotre [a,b,*]

[a] Department of Materials Science and Engineering, The University Tennessee, Knoxville, TN-37996, United States
[b] Metals and Ceramics Division, Oak Ridge National Lab, Oak Ridge, TN- 37831, United States

Received 6 December 2005; received in revised form 17 April 2006; accepted 4 May 2006

Abstract

The surface properties of biomedical implant materials control the dynamic interactions at tissue–implant interfaces. At such interfaces, if the nanoscale features influence protein interactions, those of the microscale and mesoscale aid cell orientation and provide tissue integration, respectively. It seems imperative that the synthetic materials expected to replace natural hard tissues are engineered to mimic the complexity of their hierarchical assembly. However, the current surface engineering approaches are single scaled. It is demonstrated that using laser surface engineering a controlled multiscale surface can be synthesized for bioactive functions. A systematic organization of bioactive calcium phosphate coating with multiphase composition on Ti-alloy substrate ranging from nano- to mesoscale has been achieved by effectively controlling the thermo physical interactions during laser processing. The morphology of the coating consisted of a periodic arrangement of Ti-rich and Ca-P-deficient star-like phases uniformly distributed inside a Ca-P-rich self-assembled cellular structure with the presence of CaO, α-tricalcium phosphate, $CaTiO_3$, TiO_2 and Ti phase in the coating matrix. The cellular structures ranged in diameter from 2.5 μm to 10 μm as an assembly of cuboid shaped particles of dimensions of ~200 nm × 1 μm. The multiscale texture also included nanoscale particles that are the precursors for many of these phases. The rapid cooling associated with the laser processing resulted in formation, organization and controlling dimensions of the Ca-P-rich glassy phase into a micron scale cellular morphology and submicron scale clusters of $CaTiO_3$ phase inside the cellular structures. The self-assembly of the coating into multiscale structure was influenced by chemical and physical interactions among the multiphases that evolved during laser processing.
© 2006 Acta Materialia Inc. Published by Elsevier Ltd. All rights reserved.

Keywords: Titanium alloy; Calcium phosphate; Multi-scale; Self-assembly

1. Introduction

Calcium phosphate (Ca-P) compositions are materials with excellent biocompatibility. In their bulk form, however, due to their inferior mechanical properties they are unsuitable candidates for applications involving direct replacement of hard tissues. However, Ca-P compositions deposited as coatings on a mechanically strong and biocompatible Ti-alloy substrate hold tremendous promise for exploitation in the bioenvironment. Typically, Food and Drug Administration (USA) approved plasma spray techniques are adopted for coating implants with biocompatible materials. But the poor process control, irregular morphology, poor control of coating properties, and low adherence of the coatings often result in loosening of the implants in due course [1]. Based on this premise, laser assisted surface engineering is evolving as a alternative to the conventional plasma coating process and its suitability and potential as a tool in modifying implant surfaces have been already described in detail in Ref. [1]. Usually materials like hydroxyapatite (HA), zirconia or other bioglasses are coated on substrates like Ti alloys forming new chemical species, which would improve the biocompatibility [1]. On the other hand laser surface texturing to achieve three-dimensional structures at the micrometer and submicrometer scale has also been used for improving the biocompatibility of surfaces [1]. Moreover, with the

* Corresponding author. Address: Department of Materials Science and Engineering, The University Tennessee, Knoxville, TN-37996, United States. Tel.: +1 865 974 3609; fax: +1 865 974 4115.
E-mail address: ndahotre@utk.edu (N.B. Dahotre).

1742-7061/$ - see front matter © 2006 Acta Materialia Inc. Published by Elsevier Ltd. All rights reserved.
doi:10.1016/j.actbio.2006.05.001

advancement in characterization techniques and active collaborations between material scientists and biologists across the world, it has recently been realized that the surfaces of natural biomaterials are organized at multiscale levels and therefore synthetic replacement implants should also bear a close relationship with them, apart from just mimicking their chemistry. This stems from the fact that protein scale interactions are influenced at the nanoscale, the cell level orientation is involved with features at the microscale while the tissues interact with features at higher length scales [1]. In the present work, a concept involving simultaneous integration of coating and texturing operations was implemented to produce a textured coating using laser processing. Through modulation of the laser beam shaping optics and processing parameters (beam fluence and traverse speed), suitable thermal conditions were generated for the creation of a multiscale coating via melting and solidification of the precursor deposit.

2. Experimental work

Coupons (50 mm × 100 mm × 3 mm) of Ti-6Al-4 V alloy were cut from a large plate using Techcut 10™ Allied High Tech Products Inc. The coupons were polished for a roughness of 0.5 μm. The starting powder of calcium phosphate tribasic, $Ca_3(PO_4)_2$ was obtained from Fisher Scientific. The coupons were washed in water and rinsed with acetone. Using an air spray gun the starting powder was mixed with a water based organic solvent and was sprayed onto these coupons to achieve a uniform thickness of 40 μm. A continuous wave Nd:YAG laser operating at a wavelength of 1064 nm was employed. In ambient air the samples were processed with 850 W power and processing speeds ranging from 0.021 m/s to 0.041 m/s. The laser beam at the focus was elliptical in cross section, being 5 mm × 1.5 mm in size. The processing was conducted by operating the laser beam in continuous mode such that with the given processing speed and beam size, it provided the beam residence (interaction) time of 45 ms at any given location on the sample. In order to examine the precipitation of HA as an indirect indication of biocompatibility of the modified surface, the laser surface modified samples were immersed in conventional simulated body fluid (SBF) for 14 days before being removed from the solution for scanning electron microscopy (SEM) and X-ray diffraction (XRD) analyses. SBF was prepared as per standard procedures reported in the literature [2]. The sample was placed in SBF maintained at a constant ph of 7.4 at 37 °C and refreshed every day for 14 days.

Using a Philips Norelco X-ray diffractometer, the starting powders as well as the coatings were characterized with Cu Kα radiation operated at 30 kV and 20 mA. The diffraction range was from 20° to 60° with a step increment of 0.02° and a count time of 1 s. Surface morphology was evaluated using a JEOL scanning electron microscope. Energy dispersive spectroscopy (EDS) for chemical microanalysis was performed in conjunction with SEM.

3. Results and discussion

3.1. Multiscale and multiphase microstructure

Calcium phosphate tribasic powder, a precursor, was pre-deposited at ambient temperature as a suspension in a water based organic solvent; therefore, as expected, it did not undergo any physical and chemical changes, which was verified using XRD and SEM analyses. It is, therefore, considered not necessary to include the corresponding XRD pattern and SEM image of the pre-deposited calcium phosphate coating prior to laser treatment. After laser processing, however, the samples were thoroughly observed by SEM to understand the surface characteristics. The morphology of the laser processed coating consisted of a periodic arrangement of star-like phases (A) uniformly distributed inside a self-assembled cellular structure (B) (Fig. 1a). The elemental analysis based on EDS data revealed that the star-like structure 'A' is Ti rich and Ca-P deficient (Fig. 1b) whereas 'B' is a Ca-P-rich region (Fig. 1c). Furthermore, XRD analysis (Fig. 1d) predicted the presence of CaO, α-tricalcium phosphate (TCP), $CaTiO_3$, TiO_2, along with Ti phase in the coating. The cellular structures ranged in diameter from 2.5 μm to 10 μm and they were an assembly of cuboid shaped particles of dimensions of ~200 nm × 1 μm. The assembly of these multiple phases into multiscale texture is more vividly realized in Fig. 2. It is worth noting that the multiscale texture also included nanoscale particles, labeled as 'C'. These particles can be the precursors for many other phases formed later. Although extensive efforts were made to assign the known phases (from JCPD files data base) to all peaks in the XRD pattern (Fig. 1d), a few peaks remain unidentified. Such a situation is very common, especially in material systems that involve several metallic and ceramic components with a possibility of formation of complex phases that are totally new and not referenced in the open literature. Furthermore, the evolution of such complex and previously unknown phases is highly likely to happen in a process such as laser processing that is often associated with near non-equilibrium or non-equilibrium thermodynamic conditions. Identification of such unknown phases could be a major effort and it was not the focus of this study. However, identification of such unknown phases could be considered if they are substantial in quantity and have a significant bearing on the end properties.

3.2. Morphological and chemical evolution

During laser interaction (laser fluence of 4.25×10^8 W s/m^2) both the precursor calcium phosphate (melting point of TCP is 1550 °C) and part of the underlying substrate Ti-6Al-4V (melting point 1600 °C) were melted. As the laser processing was conducted in ambient atmosphere several oxide phases evolved, such as TiO_2 (melting point 1850 °C), CaO (melting point 2572 °C), $CaTiO_3$ (melting point 1992 °C), and P_2O_5 as indicated by the XRD

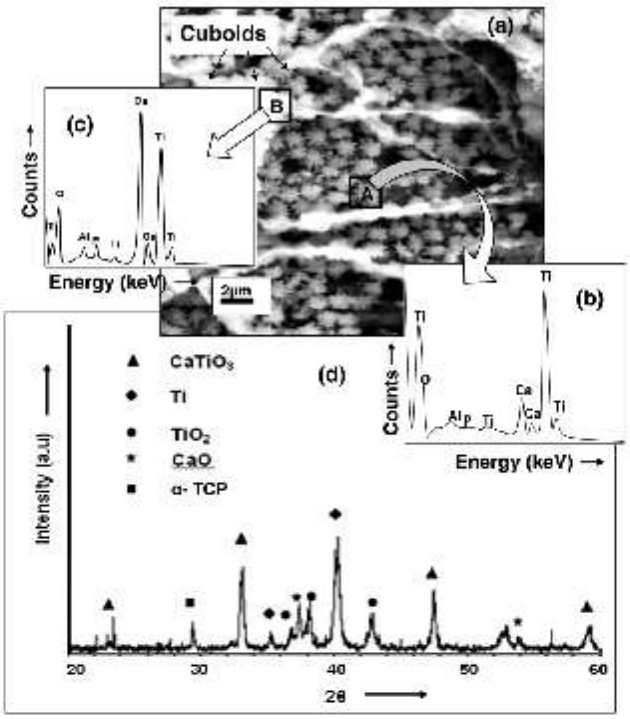

Fig. 1. (a) Scanning electron image of a sample of laser processed surface showing multiscale features; (b) EDS spectra taken of region A; (c) EDS taken of region B; (d) XRD spectrum of the surface.

spectrum in Fig. 1d. Evolution of these phases was the result of direct oxidation of the elements and/or secondary product of the chemical reactions among various compounds. The dehydration of calcium phosphate during laser processing led to formation of α-TCP and this in turn partially decomposed into CaO and P_2O_5. The presence of $CaTiO_3$ can be attributed to an interaction between Ca-rich phases with TiO_2 as per Eq. (1) [3] and as also observed during laser surface cladding of HA on Ti6Al4V alloy [4]. The SEM observations coupled with EDS analysis indicated that Ca- and Ti-rich star-like features represented by 'A' in Fig. 1 consisted of $CaTiO_3$ with its evolution through the chemical reaction represented by Eq. (1). Whereas the multicomponent (Ca, P and Ti) ring-like structures may represent Ca-P-TiO_2 phases. Such an evolution through segregation of phases was expected because of the difference in the wettabilities of Ca-P-rich phases floating in liquid Ti.

$$\text{Calcium phosphate}_{(l)} + TiO_2 \rightarrow CaTiO_3 + \alpha - TCP + H_2O_{(g)} \uparrow \quad (1)$$

It is known that rapid solidification during laser processing aids freezing of the Ca-P-rich ring structure into a glassy phase [5]. It is possible that during high temperature exposure dehydration is followed by decomposition of calcium phosphate into a mixture of CaO, α-TCP, P_2O_5 which float in a TiO_2 environment. The presence of these phases is congenial for glass formation and, therefore, it is hypothesized that under favorable thermal gradients from the periphery to the center, the CaO-P_2O_5 system with limited amounts of TiO_2 constituents was likely to form a glass network. Since the glass phase is interspersed in a matrix of $CaTiO_3$ the existence is not clearly revealed by XRD (Fig. 1d). However, detection and thorough characterization of such a glassy phase is possible through techniques such as transmission electron microscopy, which will form part of our future efforts. Furthermore, though the presence of P_2O_5 is not evident in the final coating (Fig. 1d) it can be an intermediate product of dissociation of calcium phosphate and it has the capability to act as a network former. In addition, TiO_2 is a network modifier in providing extra oxygen atoms in bridging the network and finally the CaO molecules act as modifiers in completing the glass network [6]. Thus the final microstructure consisted of Ca-P-rich glassy phase along with submicron scale $CaTiO_3$ phases organized in a periodic fashion.

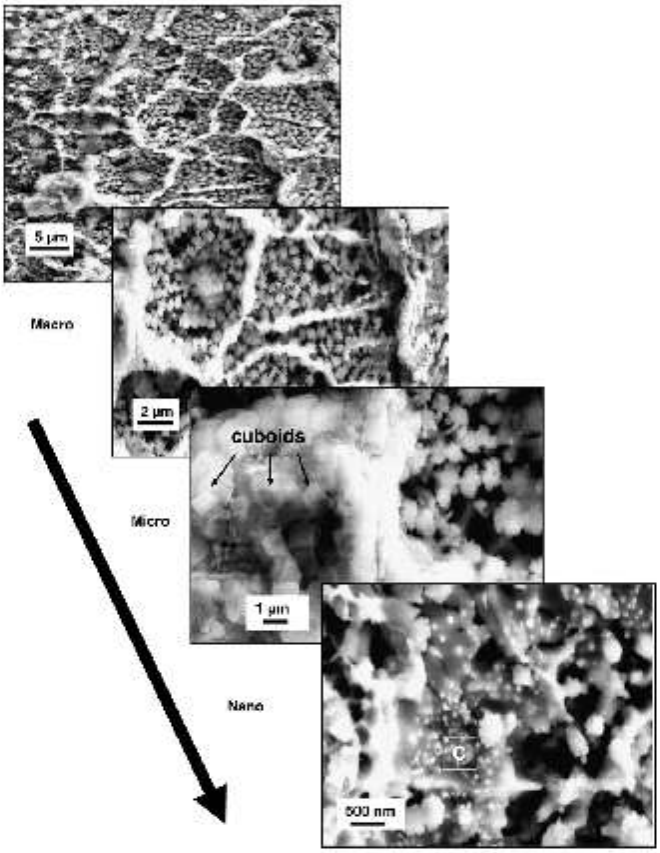

Fig. 2. Scanning electron microstructures revealing multiscale texture evolved in the coating. The micrographs were recorded at increasing magnifications.

In the process of multiscale organization the above referenced phases evolved sequentially with self-assembly dominant from the nano- to mesoscales. Even though the rules for self-assembly at these scales are similar they are not identical. In general, attractive interactions due to capillary forces between the drops of liquid with high interfacial energy provide self-assembly of particles leading to the minimization of the interfacial free energy of the surfaces [7]. The following description explains the various steps involved in this multiscale morphological evolution based on self-assembly concepts.

Initially within the molten pool the Ca-P-rich clusters tend to coagulate into nanoscale particles since similar particles floating at a liquid interface attract each other. Each of the faces of these nanoparticles upon subsequent interactions with TiO_2 tends to become hydrophilic. After which the particles exhibit dipole-like interactions, as illustrated schematically in Fig. 3a. Since initially the particle size is small, the capillary interaction force is more influenced by wettability than particle weight and submicron scale assembly of CaP-TiO_2-rich particles continues through formation of these dipoles with a tendency to organize into a periodic arrangement resulting in a faceted structure. Furthermore, as mentioned earlier, due to the presence of suitable glass forming phases in the surrounding region (P_2O_5, a glass network former and TiO_2 and CaO, glass modifiers), along with the rapid solidification rate associated with laser processing, these CaP-TiO_2 particles when they collide stick together irreversibly; this results in the formation of a glass rather than a crystal, as illustrated schematically in Fig. 3b [8]. However, in the later stage when these glassy particles increase in size, the microscale self-assembly of CaP-TiO_2 in cellular network is primarily influenced by the components involving hydrodynamic drag force (F_d) and normal capillary force (F_n). Kralchevsky and Denkov have reported that in systems which contain particles float-

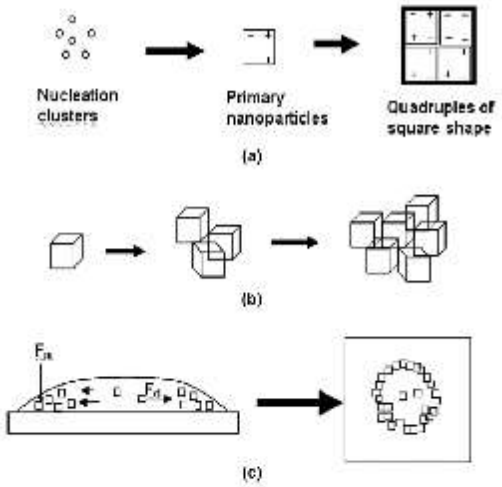

Fig. 3. (a) Cubic shaped (sub micron) structure evolution from sub-nanoscale nuclei clusters; (b) random irreversible attachment of colloid particles results in glassy material; (c) capillary (F_n) and hydrodynamic forces (F_d) acting on CaP particles result in self assembling ring-like structure shown on right.

ing in molten liquid during solidification, F_d and F_n play an important role in segregation of the particles [9]. Under normal capillary forces, few particles got stuck along the contact line and the process proceeded at a fixed contact radius, as illustrated schematically in Fig. 3c. The liquid solidification from the edge drew the particles from the interior towards the edge under the influence of hydrodynamic drag force. This action would result in the depletion of Ca-P concentration at the center and accumulation of Ca-P-rich glassy structure at the periphery. Assembly of Ca-P-rich phase particles into irreversible glassy clusters may continue at the periphery. The Ca-P depleted central region primarily consisting of high melting CaO would in turn react with TiO_2 from the substrate to nucleate $CaTiO_3$ particles. This resulted in a glassy CaP-TiO_2 cellular structure surrounding the $CaTiO_3$ (Ca-P deficient) star-like features (Figs. 1a and 2). The sequence of steps during the evolution of this multiscale structure from segregation of Ca-P-rich and deficient regions to final solidification during laser processing is schematically presented in Fig. 4. Formation of cellular and star-like morphologies and their dimensions depend upon the thermodynamic conditions generated by a set of laser processing parameters.

For each of the chemical species that are produced as a result of the high temperature interaction and solidification it is important to acknowledge their biocompatibility. Nanoscale Ca-P is shown to have good biocompatibility. Lima et al. have shown that osteoblast proliferation was significant on nanostructured and nanophase materials [10]. The current surface also exhibited the presence of microscale $CaTiO_3$ and Webster et al. have revealed that there was increased osteoblast adhesion on materials that contained $CaTiO_3$ compared to those containing both pure hydroxyapatite and uncoated titanium [11]. At much higher length scale corresponding to the glassy CaP-TiO_2 the literature states that by modifying the composition of glass ceramics, specifically incorporating metallic oxides like TiO_2 the degradation rate in a bio-environment can be controlled for desired dissolution [12,13]. Thus the material systems containing phases such as CaO, P_2O_5, and TiO_2 remain bioactive and improve ostecompatibility. On the whole the multiple phases produced in the current processing are biocompatible and when coupled with their multiscale nature they are expected to improve their osteoconductivity. Thus the emphasis of the present work was to show the feasibility of laser based technique to produce multiphase and multiscale coating and possible physical phenomena behind the evolution of these multifaceted structures. However, the effect of evolution of these multiphases and multiscale structures on biocompatibility of the coatings is ongoing work that involves various test approaches and will be a major subject of subsequent

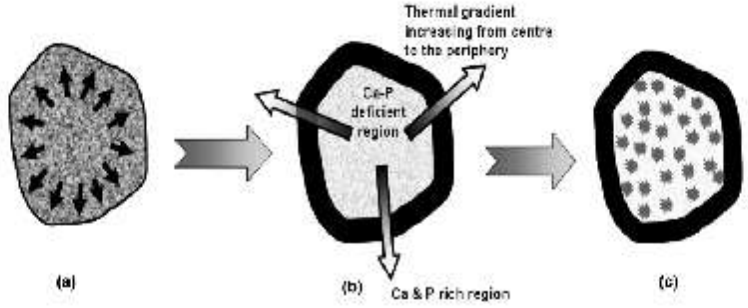

Fig. 4. Dynamic evolution of microstructure in the molten pool at high temperatures: (a) Mineral calcium phosphate (dark) phases floating in Ti metallic (light) environment. The arrows indicate the direction of migration of Ca-P-rich phases; (b) segregation into Ca-P-rich and deficient regions; (c) reaction and nucleation of $CaTiO_3$.

reports. The formation of CaO in trace amounts appeared to be associated with the specific laser processing conditions (speed, power, cover gas) employed in the present work. Traces of this CaO can be substantially reduced by introducing a post laser process step such as mild rinsing in water that dissolves the CaO as indicated by XRD spec-

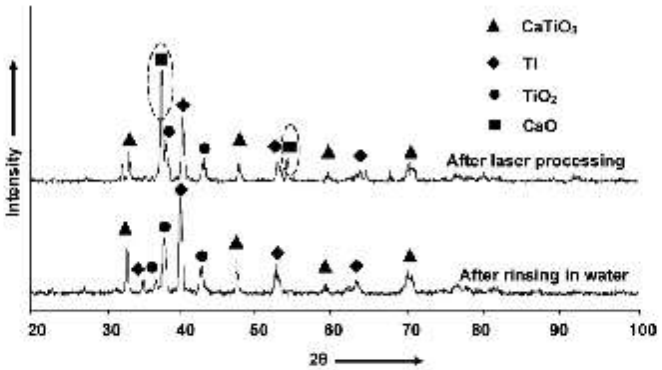

Fig. 5. XRD patterns showing the influence of water rinsing in reducing the CaO content on the laser processed surfaces.

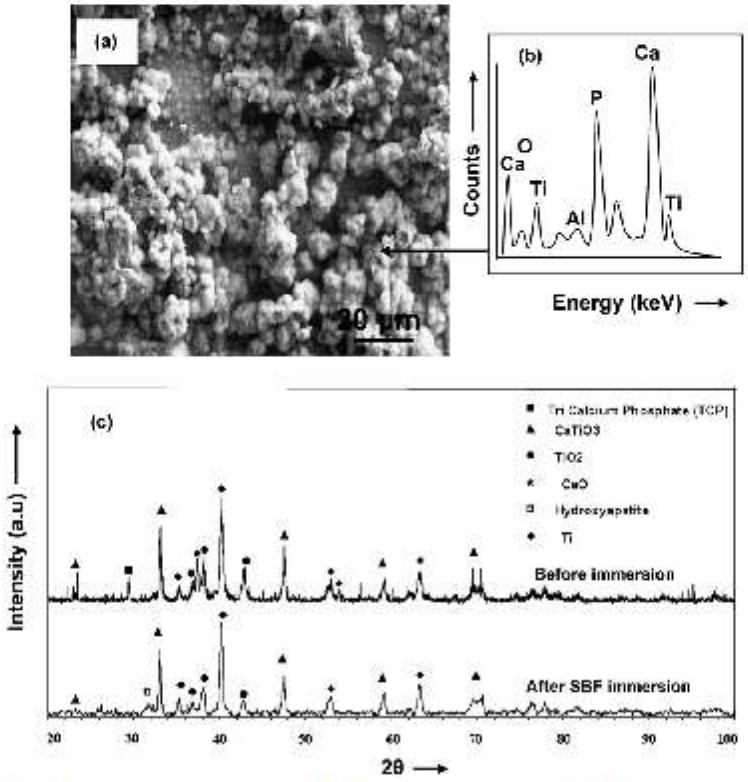

Fig. 6. (a) Surface morphology after 14 days immersion in SBF; (b) EDS of the globular shaped particles precipitated after immersion in SBF indicating the formation of HA; (c) Comparison of XRD spectra from laser processed samples before and after immersion in SBF for 14 days.

tra corresponding to as-laser processed and water rinsed laser processed samples (Fig. 5). Furthermore, in ongoing efforts the authors have been able to identify a set of laser processing parameters complemented by an appropriate cover gas that has further reduced the presence of trace CaO. Fig. 6 provides the observations corresponding to examination of the precipitation of HA as an indirect indication of biocompatibility of laser modified surface immersed in SBF for 14 days. The morphology of the laser coated surface after immersion seems to have resulted in the formation of globular HA precipitates (Fig. 6a). EDS on the globular surfaces clearly indicated that the region is rich in Ca and P (Fig. 6b) providing a possibility of HA evolution. When the XRD patterns of the two surfaces before and after SBF immersion were compared (Fig. 6c), it was clearly seen that the evolution of HA started to take place with dissolution of phases like CaO Although the formation of such HA precipitates on laser modified surface is an indirect indication of biocompatibility of the surface, the authors are currently involved in translational research in collaboration with researchers in biomedical and medical fields to conduct in vitro studies on these samples and detailed results will be the subject of future publications.

4. Conclusions

A surface engineering approach using a laser was demonstrated to produce a textured coating of Ca-P on a Ti-alloy substrate. The coating was multiphase and multiscale ranging from the meso- to nanoscale. The evolution of these phases and features was attributed to the thermodynamic conditions prevailing during laser processing. The rapid cooling associated with the laser processing resulted in the formation, organization and controlling of the dimensions of the Ca-P-rich glassy phase into a micron scale cellular morphology and submicron scale clusters of $CaTiO_3$ phase inside these cells. Both of these have been reported in the literature to actively improve the osteoconductivity of the biomaterial surfaces. The authors hope that these findings will excite researchers in related biomaterials fields and will trigger further study of the cytocompatibility of these surfaces for improved tissue–surface interactions.

Acknowledgements

The authors wish to acknowledge the contributions of Gregory Jones of University of Tennessee, Knoxville in helping us with the SEM micrographs as well as Joey Edgemon of Oak Ridge National Lab, USA for laser processing of the samples.

References

[1] Kurella A, Dahotre NB. Surface modification for bioimplants: the role of laser surface engineering. J Biomater Appl 2005;20:5–50.
[2] Oyane A, Him HM, Furuya T, Kobuko T, Miyazaki T. Nakamura preparation and assessment of revised simulated body fluids. J Biomed Mater Res A 2003;65:188–95.
[3] Lusquinos F, De Carlos A, Pou J, Arias JL, Boutinguiza M, Leon B, et al. Calcium phosphate coatings obtained by Nd:YAG laser cladding: physicochemical and biologic properties. J Biomed Mater Res A 2003;64:630–7.
[4] Lusquinos F, Pou J, Boutinguiza M, Quintero F, Soto R, Leon B, et al. Main characteristics of calcium phosphate coatings obtained by laser cladding. Appl Surf Sci 2005;247:486–92.
[5] Lawrence A, United States Patent: 6,846,853. Calcium phosphate bone graft material, process for making same and osteoimplant fabricated from same.
[6] Chiang M, Birnie III DP, Kingery WD. Physical ceramics. In: Chaing M, Birnie III DP, Kingery WD, editors. Principles for ceramics science and engineering. New York, NY: John Wiley & Sons; 1997. p. 1–95.
[7] Bowden N, Terfort A, Carbeck J, Whitesides GM. Self-assembly of mesoscale objects into ordered two-dimensional arrays. Science 1997;276:233–5.
[8] Whitesides GM, Grzybowski B. Self-assembly at all scales. Science 2002;295:2418–21.
[9] Kralchevsky PA, Denkov ND. Capillary forces and structuring in layers of colloid particles. Curr Opin Colloid Interf Sci 2001;6:383–401.
[10] Lima RS, Khor KA, Li H, Cheang P, Marple BR. HVOF spraying of nanostructured hydroxyapatite for biomedical applications. Mater Sci Eng A 2005;396:181–7.
[11] Webster TJ, Ergun C, Doremus RH, Lanford WA. Increased osteoblast adhesion on titanium-coated hydroxylapatite that forms CaTiO3. J Biomed Mater Res A 2003;67:975–80.
[12] Vallet-Regi M. Ceramics for medical applications. J Chem Soc Dalton Trans 2001:97–108.
[13] Diasa AG, Skaklec JMS, Gibsond IR, Lopesa MA, Santo JD. In situ thermal and structural characterization of bioactive calcium phosphate glass ceramics containing TiO_2 and MgO oxides High temperature – XRD studies. J Non-Cryst Solids 2005:810–7.

Author's personal copy

Materials Science and Engineering C 28 (2008) 1560–1564

Contents lists available at ScienceDirect

Materials Science and Engineering C

journal homepage: www.elsevier.com/locate/msec

Effect of microstructural evolution on wettability of laser coated calcium phosphate on titanium alloy

Anil K. Kurella [a,1], Michael Z. Hu [b], Narendra B. Dahotre [a,c,*]

[a] Department of Materials Science and Engineering, University of Tennessee, Knoxville, Tennessee 37996, United States
[b] Separations and Materials Research, Nuclear Science and Technology Division, Oak Ridge National Laboratory, Oak Ridge, Tennessee 37831, United States
[c] Materials Processing, Materials Science and Technology Division, Oak Ridge National Laboratory, Oak Ridge, Tennessee 37831, United States

ARTICLE INFO

Article history:
Received 14 August 2007
Received in revised form 25 March 2008
Accepted 28 April 2008
Available online 6 May 2008

Keywords:
Laser
Wettability
Biocompatibility
Calcium phosphate
Titanium alloy
Biomaterial

ABSTRACT

Surface engineering of synthetic implant materials provides an exciting opportunity to mimic natural biomaterials. Surface that are bioactive and textured at multi-scale have the potential for easier osseointegration. Ti alloy surfaces known for their biocompatibility are coated with bioactive calcium phosphate using a laser source at multiple processing speeds. The resulting surface has multi-scale morphology and multi-phase chemical nature. Faster processing speeds showed improved wettability to water along with higher degree of crystallinity in the phases present. Furthermore, decreased laser processing speeds induced formation of increased amount of glassy phases that are expected to provide increased biocompatibility. The combination of these opposing effects suggested that optimum crystallinity leading to optimum wettability can be produced at intermediate speeds for improved biocompatibility.

© 2008 Elsevier B.V. All rights reserved.

1. Introduction

Ti and its alloys are known to be biocompatible and are used for load bearing applications in the artificial implants world. However in many clinical studies it has been shown that a good bond between tissue and metallic implant is not achieved. To overcome this problem various Ca, P based coatings have been suggested [1–3]. It has been established that the chemical nature of the surface plays a key role in osteointegration [1–3]. In addition to this recently it has been shown that surfaces that are hierarchically textured tend to aid biocompatibility [4]. Surfaces with multi-scale features ranging from nano to microscale and bioactive at the same time are expected to provide improved biocompatibility.

On account of its ability to control and specifically modify the surface of materials for desired applications at a rapid pace lasers are currently being explored as a surface engineering tool for biomaterial application [5]. The present work describes a simultaneous coating and texturing operation performed using this laser energy source. A study of the chemical nature of the surfaces produced, the factors that are responsible for the chemical nature and the wetting properties of these surfaces are presented here. As with all implant materials their integration into bio-environments is of prime importance. Therefore, study of wettability of engineered surface, one of the important factors for such integration [6], is essential.

2. Experimental work

Coupons (50 mm × 100 mm × 3 mm) of Ti–6Al–4V alloy were cut and polished for a roughness of 0.5 μm. The couponswere then washed with water followed by acetone. Commercially available hydroxyapatite [$Ca_5(OH)(PO_4)_3$] powder obtained from Fisher Scientific was taken as the precursor. The powder morphology was spherical with unimodal distribution in the range of 10–30 μm for diameter. The powder of was mixed with water based proprietary inorganic solvent and uniformly sprayed onto the surfaces of these coupons using an air spray gun. A consistent thickness of 40 μm was achieved. The thickness was determined by the difference between the micrometer readings on the optical microscope focused on the surface of sprayed pre-coating and the substrate surface at the bottom of the scratch in the sprayed pre-coating. The average of the 10 readings at various locations on the samples was reported. These pre-coated samples were dried for about 15 min to remove the moisture. Using a continuous wave Nd:YAG laser operating at 1064 nm wavelength the samples were processed with 850 W power at processing speeds ranging from 100 cm/min to 225 cm/min that yielded the input energy in the corresponding range of 8500 J/cm^2 to 3780 J/cm^2.

The purpose of present study was to evaluate the effects of overall surface texture (morphology) and chemical (phase) and microstructural (grain) nature on wettability. Therefore, stylus based profilometry was employed for roughness measurements whereas XRD technique was adopted for phase identification and crystallite size evaluation. These effects can also be evaluated in much more details using the

* Corresponding author. Tel.: +1 865 974 3609; fax: +1 865 974 4451.
E-mail address: ndahotre@utk.edu (N.B. Dahotre).
[1] Currently at: Intel Corporation, Hillsboro, Oregon 97124, United States.

0928-4931/$ – see front matter © 2008 Elsevier B.V. All rights reserved.
doi:10.1016/j.msec.2008.04.015

Author's personal copy

techniques such as atomic force microscopy (AFM) and transmission electron microscopy (TEM) than that can be obtained from the present techniques. The future efforts following to the present work will include such detailed study.

Philips Norelco X-ray diffractometer with Cu Kα radiation operated at 30 kV and 20 mA was used to characterize the coatings. The samples were scanned for 2θ from 20° to 100° with a step increment of 0.02° and a count time of 1 s. Surface morphologies were studied using a JEOL 6400 scanning electron microscope (SEM). Chemical microanalysis with energy dispersive spectroscopy (EDS) was performed in conjunction with SEM.

Roughness analysis was done using a profilometer based instrument from Mahr Federal. 5 scans were taken for each surface and the average values are reported here. As mentioned earlier, the roughness measurements were intended for measuring overall surface morphology produced during laser treatment through melting followed by solidification. Such morphological features were appeared to be at micron level hence, profilometry based measurements considered appropriate and sufficient in the present study. Contact angle measurements were made using Tantec half angle™ technique. Based on this concept contact angle measurements of a water drop on laser treated surfaces were carried out. Contact angle measurements were carried out by dropping a 5 μL droplet of water and measuring the angles of the shadows using the Tantec, Cam-Plus contact angle meter. Measurements were taken after the droplets settled and reached an equilibrium shape. The time taken for droplets to reach equilibrium was typically 4–5 s, after dropping onto the surface. Parameters like: flow rate, height of dropping, base line determination, optics adjustment and time of measurements were optimized prior to experiments. Care was taken to ensure accurate and repeatable data collection following optimization. Multiple readings (10) were taken on each sample and average was reported.

A finite element approach based on FEMLAB heat transfer transient mode was utilized to determine the temperature–time cooling curves. The methodology was similar to what Harimkar et al., have reported in their work on laser processing of alumina ceramics [6,7]. Fourier's second law presented in Eq. (1) was the basis of temperature determinations [6]. A time stepping of 1 ms was used for the whole process.

$$\frac{\partial T(x,t)}{\partial t} = \alpha \frac{d^2T(x,t)}{\partial x^2} \quad \text{where,} \quad \alpha = k/\rho C_p \tag{1}$$

The thermal diffusivity, α was determined for calcium phosphate and the values of thermal conductivity (k), density (ρ) and specific heat (C_p) were obtained from available literature [8].

3. Results and discussions

The laser processed samples seem to have a complex hierarchical evolution of multiple phases and morphological features, the details of which will be discussed at a later stage in this paper. Two images of samples processed at 150 cm/min and 200 cm/min are presented here in Fig. 1. The primary interest in this paper was to study how such morphologically and chemically varying surfaces can influence the wettability when contacted with water (liquid). The final shape taken by a liquid droplet when brought in contact with a flat surface is expressed in terms of the contact angle θ. Young's equation relates this contact angle to solid surface energy, γ_{sv}; the liquid surface energy, γ_{lv}; and the solid–liquid interfacial energy, γ_{sl}, through the principal of virtual work as presented below [5]:

$$\cos\theta = \frac{\gamma_{sv} - \gamma_{sl}}{\gamma_{lv}} \tag{2}$$

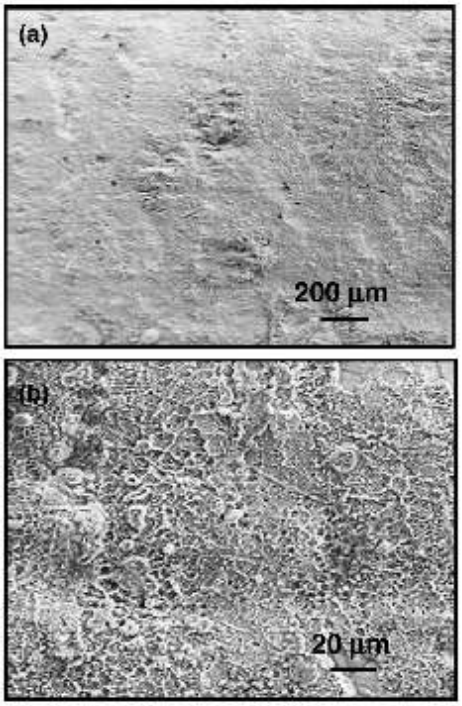

Fig. 1. Scanning electron micrographs of laser processed surfaces. (a) Low magnification image of sample processed at 150 cm/min. (b) Higher magnification image of sample scanned at 200 cm/min showing hierarchically organized structures.

The surface energies and hence the contact angle are also influenced by the factors such as surface roughness and surface chemistry or surface phases. In the present work, the effect of variation of laser scanning speed on surface roughness and contact angle (wetting angle) of coated samples is presented in Fig. 2. The surface roughness decreased with increased scanning speed indicating generation of smoother surface at higher speeds as observed and explained in earlier work by the authors [9]. Similarly, the contact angle decreased with increase in scanning speed indicating increased wettability of the surface for higher scanning speeds. Wenzel suggested that the roughness factor, r_s is related to the contact angle θ by the following equation [5].

$$r_s.(\gamma_{sv} - \gamma_{sl}) = \gamma_{lv}.\cos\theta \tag{3}$$

The equation indicates an inversely proportional relationship between roughness factor and contact angle. If r_s is large the solid surface is rough and corresponding cosθ is large which means θ is small for improved wettability. On the contrary, in the present study the contact angle and roughness follow a direct proportionality (Fig. 2). The surface energy components of the equation are, therefore, expected to have greater influence on the contact angle (θ). However, defining the surface energy of the laser processed surface is quite complex because it involves several important factors such as oxygen content, chemical in-homogeneity due to multiple phases, and crystal sizes and shapes. The effect of surface phases on wettability is expressed by Cassie's equation which is an analogue of Wenzel equation of rough surfaces

Author's personal copy

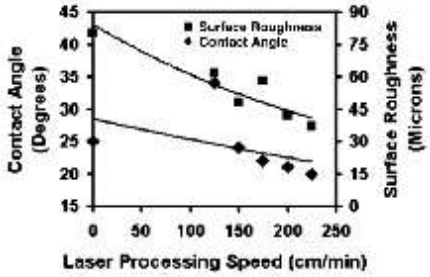

Fig. 2. Contact angle and roughness measurements on samples processed at different laser processing speeds.

and gives the stable equilibrium contact angle for chemically heterogeneous surface [10].

$$\cos\theta = f_1 \cos\theta_1 + f_2 \cos\theta_2 \quad (4)$$

In the above equation θ is the contact angle for a liquid on a composite surface whereby θ_1 is the contact angle for component (phase) 1 with area fraction f_1 and θ_2 is the contact angle for component (phase) 2 with area fraction f_2 present in the composite material. In the present work, as explained in the following section the final surface constitutes multiple phases and thus provides a complex scenario for effect of surface roughness and chemical composition on wetting behavior.

It is obvious that the phases and their surface area distribution play an important role in the final macroscopic contact angle. Hence X-ray diffraction (XRD) analysis was employed for identification and quantification of surface phases. XRD pattern of the laser processed surfaces are presented in Fig. 3. Based on number, locations, intensities, and integrated area of the peaks in these patterns it is obvious that laser processing conditions have major influence on the phase composition of surface. The characteristic phases in laser coated samples are several phases such as $CaTiO_3$, TiO_2, and CaO along with α-Ti and β-Tri Calcium Phosphate (TCP). It appeared that at high temperature the precursor Calcium Phosphate Tribasic compound dissociated to form compounds through interactions with the substrate titanium and surrounding air [11,12]. Earlier, it has been shown that the presence of oxygen in surface composition increases the surface wettability; therefore, in the present case oxides and other phases are expected to influence wetting characteristics of the surface [5]. The peak intensities of the major peaks in the XRD patterns were measured by the JADE software attached to the Philips Noreloco XRD system. These values were then normalized by dividing their peak intensities with that of Ti. The ratios are then plotted as shown in Fig. 4. For simplicity, the figure presents relative distribution of the phases after processing with various laser scanning speeds. From Figs. 3 and 4 it can be seen that with increasing speeds the amounts of $CaTiO_3$, CaO and TiO_2 increase. β-TCP was also observed to be present on surfaces at higher processing speeds.

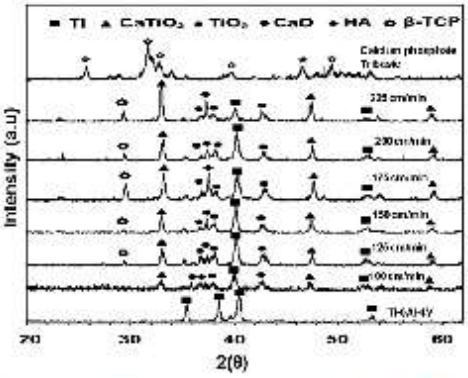

Fig. 3. XRD patterns from samples processed at different laser processing speeds.

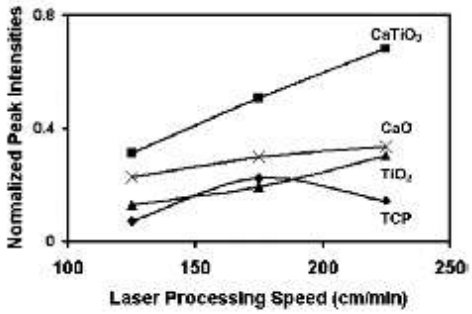

Fig. 4. Graph showing the relative amounts of various phases (normalized to Ti) at different laser processing speeds.

The variation in processing speed for fixed laser power varies the laser beam residence time which in turn incorporates variable amount of energy into the sample surface. Computed surface temperature profiles as function of time during laser treatment are presented in Fig. 5a. The final microstructure is largely influenced by cooling effects. The cooling rates, calculated from the peak temperatures to 1500bsp;°C for

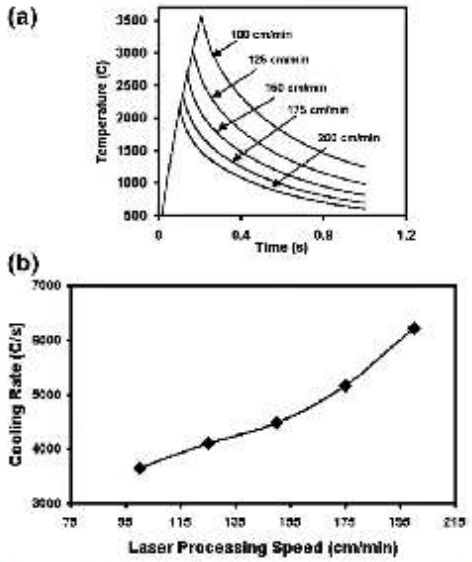

Fig. 5. Computed temperature data for various laser processing speeds. (a) Temperature distribution as function of time. (b) Cooling rates at different laser processing speeds.

Author's personal copy

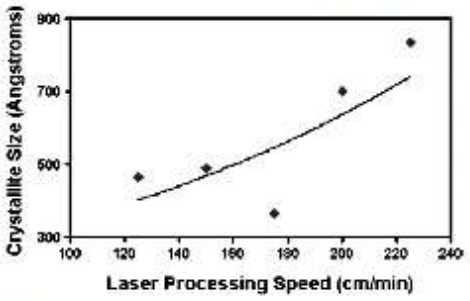

Fig. 6. Variation of crystallite size of β-TCP with laser processing speed.

various processing speeds are presented in Fig. 5h. Under such favorable conditions of high thermal gradient (cooling rates> 10^3bsp;°C/s) the co-existence of Ca and P rich Calcium Phosphate along with TiO_2 particles can lead to glassy materials [13]. For a Ca–O based system P_2O_5 from Calcium Phosphate acts as a network former while TiO_2 from surrounding molten pool plays the role of network modifier in providing extra oxygen atoms for bridging the network [8,10]. Given the high thermal gradients associated with laser processing it is not uncommon to expect glassy material formation [9,11,14]. This can also be observed from the XRD data in Fig. 3. Several peaks appeared to have a broad background indicating some kind of glassy phase constitution. Moreover, for lower speeds the overall intensity of the peaks decreased and the peak broadening became more obvious. The varying degree of broadening in the XRD patterns is specifically evident for peaks corresponding to TiO_2, $CaTiO_3$ and β-TCP. Analysis of broadening for β-TCP using the pseudo-Voigt technique showed finer crystallite sizes for slower processing speeds as illustrated in Fig. 6. Similar analysis for TiO_2 and $CaTiO_3$ also indicated the same trend although at marginal level.

From Fig. 5a and b it can be seen that at lower speeds the surfaces are exposed to higher laser input energy and hence higher temperatures for a longer duration of residence time. During the initial phase of laser processing the pre-coat dehydroxylates and the extent of dehydroxylation depends on temperature and time of exposure to high temperatures. According to L. Sun et al. such a dehydroxylation creates a barrier to nucleation of crystalline phases from hydroxyapatite and instead promotes amorphous evolution [15]. In their work on plasma sprayed hydroxyapatite on mild steel they have observed that as the particles were exposed to higher temperatures for a longer duration of time the coatings resulted in less crystallinity. Similar observations were made in the present case indicating that slower processing speeds exposed the particles to higher temperatures for longer period of time resulting in lower crystallinity and finer crystallite sizes (Figs. 3 and 6). This in turn seems to have influenced the contact angle with improved wettability found on samples that were more crystallinity at faster processing speeds. Furthermore, as indicated by Agathopoulus et al. in their work on binary oxide ceramics glassy phase containing oxides tend to improve wettability [16]. In the present work from Fig. 4 it can be seen that the proportion of oxide phases (CaO, TiO_2, $CaTiO_3$) increase with processing speeds. Although these phases are capable of glass formation in the presence of β-TCP at higher speeds, as mentioned earlier the reduction in dehydroxylation seems to limit the extent of amorphization when compared to slower processing speeds. In general, however, the proportions of oxide compounds capable of glass formation in the final surface increase and these have a tendency to improve the wettability of the surfaces [5]. In addition, the presence of biocompatible materials like TiO_2, $CaTiO_3$, β-TCP at such finer scale is expected to promote osteointegration [17–20]. A process step like water rinsing results in reducing the extent of CaO present in the final surface [11]. Further bioactivity related studies on the samples produced in the present study will be carried out in near future and observations will be reported in subsequent publication.

Surface wettability is considered to be an indicator of cell adhesion in biological environments. Hence current and future research needs to concentrate on strategies to improve wettability. Among the known factors that usually influence surface wetting, surface morphology and chemistry are considered the key contributors. From our previous studies we have recognized multi-scale nature and hierarchical evolution assisting hydroxyapatite growth when placed in simulated bio fluids [11]. In the present study, the role played by multi-phase structure on wettability has shown promise. However not clear resolution has been reached on the role played by multi-scale features on the wettability. This could probably form the basis for future research. Since conventional contact angle based wettability analysis measurements involve large liquid droplets compared to the size of the features that are to be studied it poses significant challenges in terms of methodologies that need to be adopted. One solution to this challenge seems to be in developing mathematical models based on fluid dynamics at micron and nanoscale. The future efforts, therefore, will include both experimental design and theoretical modeling for studying the effects of micro to nanoscale morphological and chemical (phases) features on wettability.

4. Conclusions

Based on the observations and discussions presented here it is clear that the laser processing speeds induced complex and variable morphological features, microstructure, and chemical phases in Calcium Phosphate coated Ti6Al4V alloy. In the present case, contact angle measurements showed that with increased crystallinity of the surfaces wettability of surfaces with aqueous medium increased whereas decreased laser processing speeds induced formation of increased amount of glassy phases for expected increased biocompatibility. This indicated that optimum crystallinity leading to optimum wettability and hence biocompatibility may be produced at intermediate speeds. The present understanding has discussed the nature of wettability predominantly from a surface chemistry perspective. The chemical species their orientation and distribution at various lengths scales seem to play an important role in wettability and this is likely to be the focus for future research.

Acknowledgements

This work is partially supported by the Division of Materials Science (KC 02 03 01 0), Office of Science, the U.S. Department of Energy at Oak Ridge National Laboratory managed by UT-Battelle, LLC, for the U.S. Department of Energy under contract DE-AC05-00OR22725.

References

[1] N. Moritz, E. Vedel, H. Yli-Urpo, M. Jokinen, M. Hupa, A. Yli-Urpo, J. Mater. Sci. Mater. Med. 15 (2004) 787.
[2] Y.S. Tian, C.Z. Chen, S.T. Li, Q.H. Huo, Appl. Surf. Sci. 242 (2005) 177.
[3] K.A. Khor, Y.W. Gu, D. Pan, P. Cheang, Biomaterials 25 (2004) 4009.
[4] J. Tan, W.M. Saltzman, Biomaterials 25 (2004) 3593.
[5] L. Hao, J. Lawrence, Mater. Sci. Eng., C 23 (2003) 627.
[6] S.P. Harimkar, A.N. Samant, N.B. Dahotre, J. Appl. Phys. 101 (2007) 054911.
[7] S.P. Harimkar, A.N. Samant, A.A. Khanga, N.B. Dahotre, J. phys., D, Appl. phys. 39 (2006) 1642.
[8] A.C. Bruno, D.P. Almond, S. Brown, I. Turner, J. Appl. Phys. 79 (1996) 6848.
[9] A. Kurella, N.B. Dahotre, J. Mater. Sci., Mater. Med. 17 (2006) 565.
[10] Eastathopoulos, M.G. Nicholas, B. Derviz, Wettability at High Temperatures, Pergamon, New York, 1999, pp. 36–39.
[11] A. Kurella, N. Dahotre, Actabiomaterialia, 2, 2006, p. 777.
[12] C.-J. Liao, F.-H. Lin, K.-S. Chen, J.-S. Sun, Biomaterials 20 (1999) 1807.
[13] M. Chiang, D.P. Birnie III, W.D. Kingery, in: M. Chiang, D.P. Birnie III, W.D. Kingery (Eds.), Physical Ceramics, Principles for Ceramics Science and Engineering, John Wiley & Sons, New York, 1997, p. 1.

Author's personal copy

[14] F. Luquinos, A. De Carlos, J. Pou, J.L. Arias, M. Boutinguiza, B. Leon, J. Biomed. Mater. Res. A 64 (2003) 630.
[15] L. Sun, C.C. Berndt, C.P. Grey, Mater. Sci. Eng., A 360 (2003) 70.
[16] S. Agathopoulos, P. Nikolopoulos, A. Salomoni, A. Tucci, I. Stamenkovic, J. Mater. Sci., Mater. Med. 7 (1996) 629.
[17] C. Cui, L. Hua, L. Yanchun, S. Jinbin, W. Ru, L. Shuangjin, G. Lindsay, Mater. Lett. 59 (2005) 3144.
[18] T.J. Webster, C. Ergun, R.H. Doremus, W.A. Lanford, J. Biomed. Mater. Res. A 67 (2003) 975.
[19] M. Vallet-Regí, J. Chem. Soc. Dalton Trans. (2001) 97.
[20] A.G. Dias, J.M.S. Skakle, I.R. Gibson, M.A. Lopes, J.D. Santo, J. Non-Cryst. Solids (2005) 810.

Phase and Morphological Evolution in Laser Textured Zirconia Coating on Ti alloy

Anil Kurella and Narendra B. Dahotre
Department of Materials Science & Engineering
The University of Tennessee, Knoxville, TN 37996

Abstract

Natural biomaterials are organized at various length scales ranging from nano to micro level. In bio-environment, while protein signaling dominates at nanoscale, contact guidance assisted by cells and tissues influence the attachment to a biomaterial at micro and macro scale respectively. Another important nature that influences the response of a biomaterial to its environment is the surface chemical activity. Currently there exist very few techniques to successfully produce controlled hierarchically integrated bioactive surface structures. In this present effort, using a laser source synthetically multi-scaled structure is produced by simultaneously coating and texturing a Ti-6Al-4V alloy with zirconia. Since the textured coatings showed multi-scaled morphological features a fractal based approach was conceptualized to reveal their complexity. The results of the fractal parameter dimensions determined from image processing techniques were correlated with stylus based roughness measurements. Furthermore, along with morphological changes, phase changes both in the coating and substrate due to laser-based thermal processing were studied using x-ray diffractometry. Such laser-based processing for morphological and phase changes in ZrO_2/Ti-6Al-4V system is envisioned for bio-implant application.

Page 1 of the “TMS outstanding graduate student paper award” paper.

Laser Surface Modification of Ti–6Al–4V: Wear and Corrosion Characterization in Simulated Biofluid

RAGHUVIR SINGH,[1] A. KURELLA[1] AND NARENDRA B. DAHOTRE[1,2,*]
[1]*Department of Materials Science and Engineering*
The University of Tennessee, Knoxville, TN 37996, USA
[2]*Materials Processing Group, Metals and Ceramics Division*
Oak Ridge National Laboratory, Oak Ridge, TN 37831, USA

ABSTRACT: Laser surface melting (LSM) of Ti–6Al–4V is performed in argon to improve its properties, such as microstructure, corrosion, and wear for biomedical applications. Corrosion behavior is investigated by conducting electrochemical polarization experiments in simulated body fluid (Ringer's solution) at 37°C. Wear properties are evaluated in Ringer's solution using pin-on-disc apparatus at a slow speed.

Untreated Ti–6Al–4V contains $\alpha+\beta$ phase. After laser surface melting, it transforms to acicular α embedded prior in the β matrix. Grain growth in the range of 65–89 μm with increase in laser power from 800 to 1500 W due to increase in associated temperature is observed. The hardness of as-laser-processed Ti–6Al–4V alloy is more (275–297 HV) than that of the untreated alloy (254 HV). Passivation currents are significantly reduced to $<4.3\,\mu A/cm^2$ after laser treatment compared to untreated Ti–6Al–4V ($\approx 12\,\mu A/cm^2$). The wear resistance of laser-treated Ti–6Al–4V in simulated body fluid is enhanced compared to that of the untreated one. It is the highest for the one that is processed at a laser power of 800 W. Typical micro-cutting features of abrasive wear is the prominent mechanism of wear in both untreated and as-laser-treated Ti–6Al–4V. Fragmentation of wear debris assisted by microcracking was responsible for mass loss during the wear of untreated Ti–6Al–4V in Ringer's solution.

*Author to whom correspondence should be addressed. E-mail: ndahotre@utk.edu

0885-3282/07/00 0001–25 $10.00/0 DOI: 10.1177/0885328207055998
© 200? Sage Publications

FIRST PROOF

The Application of Laser-Induced Multi-Scale Surface Texturing

P. Gregory Engleman, Anil Kurella, Anoop Samant, Craig A. Blue, and Narendra B. Dahotre

Recently, there has been interest in controlling microstructure and surface texture on smaller and smaller scales. However, in nature, materials are organized on length scales varying from the nano- to the micro- and larger. In order to realize hierarchical structuring for use in biomedical and mechanical systems, two methods for producing multi-scale surface microstructures and physical textures are explained. The first investigates the use of a marking laser to produce multi-scale texturing of zirconia coatings on Ti-6Al-4V substrates and the second method discusses the design and challenges associated with laser interference surface texturing along with process and material factors controlling surface structures.

INTRODUCTION

The hierarchical structure of biological systems is known to influence strength and fracture toughness. When a similar structure is present on the surface of a biomaterial (metal, ceramic, and polymer), it is recognized as the surface texture of the material. This physical texture plays a significant part in cell response and in how these materials are accepted into natural and biological systems.[1] Surfaces designed with physical texture also provide improved lubrication in sliding contact and substantially improved performance in static contacts.[2-5] Therefore, materials with multi-scale order should have greater advantage in biological[6] and mechanical[3] applications. Indeed, much work has already been performed on this topic, including work using lasers,[1,7,8] electron beams,[9] microfabrication,[6] and modeling work.[10]

It is important to note that the effect of the laser on the substrate can lie anywhere in the spectrum from mechanical to thermo-mechanical to thermal, depending upon the operating parameters. For instance, a pulse of <1 ns duration from a short wavelength (266 nm) laser is likely to have purely mechanical (ablative) effects on the surface, while a pulse of longer duration, say >20 µs, from a longer wavelength laser (1,064 nm) is likely to have predominantly thermal effects (melting and vaporization). The post-processed surface microstructure is the driving factor in determining the processing parameters of the laser.

In this work, the authors investigate the use of a writing laser and the development of laser interference surface treatment (LIST) to produce hierarchical surface microstructures and physical textures for use in biological and mechanical systems. Of primary interest will be the effect of the operating parameters on the formation of the multi-scale surface structures.

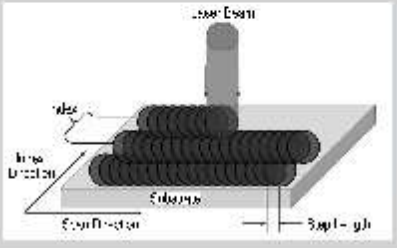

Figure 1. A schematic representation of the laser writing technique detailing some of the processing parameters.

Surface texturing using a writing laser was performed with a 25 W pulsed neodymium-doped yttrium aluminum garnet (Nd:YAG) laser by Trumpf and a VectorMark workstation. The interferometer design was carried out primarily for use with a GSI Lumonics JK701 Nd:YAG laser using optical components from CVI Laser. These two techniques are fundamentally different, relying on the adjustment of different parameters to produce the desired results.

COMPARISON OF DIRECT WRITING AND LIST TECHNIQUES

Perhaps the most immediately apparent difference between the writing technique and the interference technique is the equipment required. While the writing technique requires only the laser and control equipment, the interference technique requires the construction of an interferometer. However, the most significant difference lies in the means by which the multi-scale pattern is realized. The writing technique relies upon the overlap of the pulses, both in the direction of the scan and in the index direction and on the beam diameter at the surface (Figure 1). The relative depth/roughness of the texture is then determined by the laser power used, the scan rate setting, and the number of passes employed (Figure 2). In comparison to this, the interference technique produces a pattern that is dependent upon the wavelength of the laser being used and the degree of overlap of the interfering beams. The depth/roughness of the texture is then determined, not by the laser power, but by the resultant intensity incident on the surface due to the superposition of the interfering beams.

A significant difference between the two methods lies in the way they interact

with the substrate material. The writing technique depends on the heat capacity of the material to produce a thermally affected region, whereas the interference technique is reliant upon the thermal conductivity of the material. This arises from two factors. First, during laser writing the substrate has substantial time to cool between pulses, while an interference pattern is established in a single pulse and thus requires that the intensity peaks have great enough spatial and temporal definition so that the intervening material remains relatively unaffected. The second factor is primarily one of scale; the overall scale of the writing technique, as mentioned previously, relies on the beam size at the surface and the degree of overlap between pulses, while the scale of the interference technique depends upon the chosen wavelength and the interference angle between the beams.

DIRECT LASER WRITING FOR SURFACE-TEXTURED ZrO_2 COATING

The writing technique was demonstrated for producing a multi-scaled zirconia (ZrO_2) coating on a Ti-6Al-4V alloy substrate. ZrO_2 powder mixed with a water-based organic solvent was sprayed onto Ti-6Al-4V substrates and fused with a pulsed Nd:YAG laser operated at 10 kHz and at a constant power of 25 W. The writing process was conducted with traverse speeds of 40 cm/min., 160 cm/min., and 290 cm/min. As a result of writing under these conditions with repeated passes and alternate melting/re-melting cycles, the coating evolved into the multi-scale textured surface at all three processing speeds (Figure 2). The morphological texture of the coating was highly influenced by the laser processing speeds as indicated by R_a, R_z, and R_{max}, corresponding to the arithmetic mean deviation, mean peak-to-valley height, and maximum roughness depth of the roughness profiles, respectively (Figure 3). The writing at the intermediate speed (160 cm/min.) generated the highest roughness while softening of the roughness peaks due to repeated laser passes with larger overlap during processing at lower speed (40 cm/min.) led to formation of lower roughness values. Thus, a multi-scale textured surface evolves during the laser writing operation.[1]

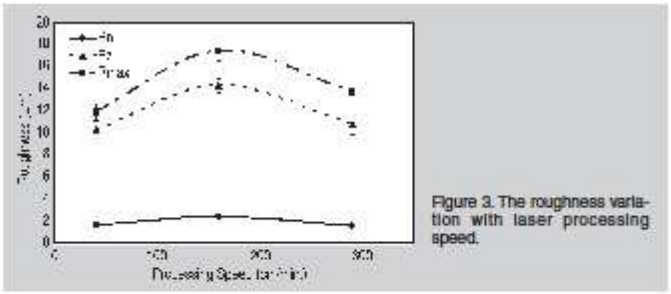

Figure 3. The roughness variation with laser processing speed.

INTERFEROMETER FOR MULTI-SCALE LASER PROCESSING

Currently, several methods exist for producing multi-scale textures on materials' surfaces via microfabrication[6,8,11] based on, but not limited to lasers,[7,8] electron beams,[9] and lithography. A relatively new method for producing these multi-scale textures utilizes the coherent property of lasers, coupled with other important factors (pulse duration and high power densities), in order to create a highly reproducible surface texture across different length scales.[7,12–14] The interference method takes advantage of the superposition of interfering beams of light to create a pattern of lines or dots, with significant long-range order, on the surface of a material. In order to accomplish this, properties of both the material being processed and the laser being used must be taken into account.

Coherence

Coherence is the most important factor when designing an interferometer, because, without coherence, the beams would not interfere to produce a series of bright and dark fringes. Coherence is of two types, temporal and spatial (Figure 4), both of which must be preserved for an interference pattern to be realized.[14] A complete knowledge of coherence is not required to design and build an interferometer, but an understanding of some specifics pertaining to coherence will help to ensure a working design.

Briefly, a measure of spatial coherence relates the correlation between two points on the same wave front, while temporal coherence relates the correlation of similar points on different wave fronts.[15] Spatial coherence is typically responsible for the speckle patterns produced by lasers and is related to the size of the source. Loss of spatial coherence occurs through volume interaction and can be limited or prevented by using high-quality optics in a clean environment. For multi-mode systems, a loss of spatial coherence occurs both as the number of modes increases and as the contribution from the secondary modes is increased.[15] Finally, spatial coherence increases with distance from the source

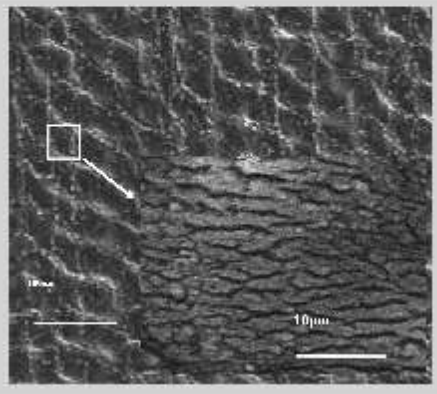

Figure 2. A scanning-electron micrograph showing the multi-scale nature of the surface processed at 40 cm/min.

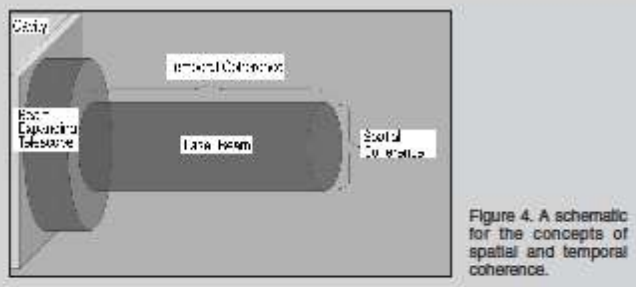

Figure 4. A schematic for the concepts of spatial and temporal coherence.

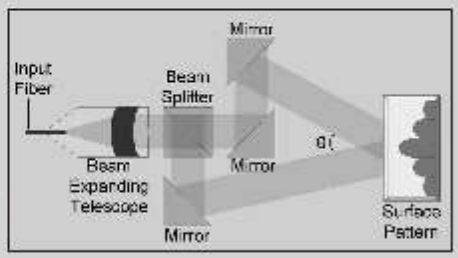

Figure 5. The basic operational schematic of an interferometer for two-beam LIST.

(as the source becomes more point-like) and can be improved by using a spatial filter consisting of a condensing lens and an aperture.

Temporal coherence, on the other hand, is relatively easier to control. Temporal coherence is related to the spectral bandwidth of the source with narrower bands resulting in longer coherence times. Perfect coherence would occur if light were emitted at a single frequency, essentially a delta function, but since no source is able to produce such pure light, the light produced in narrow bands is said to be quasi-monochromatic.[15] Maintaining temporal coherence only really becomes a problem when the optical path difference (OPD) of the two interfering beams becomes large (greater than the coherence length). The coherence length is related to the coherence time by Equation 1, where Δx_c is the coherence length, c is the wave speed, and Δt_c is the coherence time. (All equations are presented on page 49.) For perspective, a stabilized HeNe laser has a coherence length of >5 m, while a light bulb has a coherence length of <1 μm.

INTERFEROMETER DESIGN

A schematic of a typical laser interferometry set-up is shown in Figure 5. The basic design can be broken down into different elements, each with its own set of characteristics that must be considered. The first element is the laser, which, as mentioned previously, must be coherent to start with, but other properties also need to be considered, such as wavelength, pulse capabilities (time and repetition rate), and power. The second element is the interferometer itself, including the beam expanding telescope (BET), the interferometer optics, and the focusing optics. The final element is the imaging surface—the sample. In terms of interference processing, the properties of the laser and the properties of the sample are very closely related and will be treated as such.

Laser and Material

The choice of laser has a large influence over the type of surface structure that is produced. First, the fringe spac-

Table I. The Amount of Energy Required to Produce a Surface Feature of Size (d_f) Equal to Interference Fringe Size (d_i) Using Various Lasers with Suitable Operating Parameters

			Q-Switched Nd:YAG, λ = 355 nm 10 ns pulse			Pulsed Nd:YAG λ = 1.064 μm 0.5 ms pulse			Pulsed CO_2 λ = 10.6 μm 10 μs pulse		
			Interference Angle, θ								
			5°	10°	30°	5°	10°	30°	5°	10°	30°
			Interference Fringe Spacing (μm)								
Material	Thermal Conductivity k (W/mK)	Melting Point (°C)	4.07	2.04	0.69	12.21	6.11	2.06	121.51	60.97	20.48
			Energy Required to Produce Surface Feature of Size Equal to Interference Fringe Size (J/cm²)								
Al	222	660	22.68	0.72	0.25	30.81	30.37	30.08	439.79	19.85	6.21
Ag	398	962	6.87	0.84	0.36	61.09	60.43	60.00	162.16	24.38	11.22
Cu	419	1,084	27.91	1.59	0.54	86.09	84.99	84.28	590.11	45.18	16.69
AISI1020	50.2	1,538	—	666.54	0.73	44.07	42.42	41.39	—	9.4×10^3	20.53
Ni	67	1,444	—	43.39	0.51	43.70	42.41	41.59	—	819.87	14.79
Si	170	1,410	23.81	1.00	0.31	47.84	47.19	46.77	481.09	27.96	9.47
SS304	16.2	1,427	—	—	2.78	24.88	23.20	22.19	—	—	62.96
Sn	67	232	20×10^3	0.63	0.05	5.16	5.04	4.97	19.8×10^3	14.701	1.33
Ti-6A-4V	7.3	1,688	—	—	61.00	15.09	13.50	12.60	—	—	905.77
Zn	105	420	43.9×10^3	1.64	0.12	14.43	14.12	13.92	43.6×10^3	38.7	3.69
Al_2O_3	33	2,050	—	23.2×10^3	1.20	47.0	44.9	43.5	—	22.7×10^4	32.2
HA	1.2	1,100	—	—	—	9.13	6.45	5.32	—	—	—
PVC	0.159	200	—	—	—	0.68	0.33	0.23	—	—	—
PMMA	0.199	140	—	—	—	0.54	0.27	0.19	—	—	—

ing is related to the wavelength of the laser and the angle at which the beams interfere by the relation shown in Equation 2, where d_i is the interference fringe spacing, λ is the wavelength being used, and θ_i is the angle between the interfering beams.[12–14] Figure 6 shows how d_i varies with the interference angle for some common laser wavelengths employed in materials processing. Fringe spacing has tremendous bearing on the spatial resolution of surface features/effects (chemical, metallurgical, and physical texture) that can be produced. In general, for a given wavelength of laser, the smaller angles between the interfering beams produce larger fringe spacings. It is also worth noting from Figure 6 that lasers of shorter wavelength (266 nm, 355 nm, 532 nm, and 1,064 nm) produce fringe spacing that is proportionally smaller than that produced by the lasers of longer wavelength (10.6 μm).

Next, the power and the pulse length, as well as the irradiated area, then determine the fluence of the laser. A more complete simulation of the temperature field in such a process can be determined analytically using the heat transfer Equation 3 based on Fourier's law of heat conduction, where T = T(x, z, t) is the temperature at position (x, z) at time t, ρ is the density of the material, C_p is the specific heat, and q_a, q_m, and q_v are the heat added, the heat of melting, and the heat of vaporization, respectively. This is further complicated by the fact that, according to Mucklich et al.,[14] q_a takes into account the absorption coefficient, the pulse time and duration, and the reflectivity of the surface. The solution of this equation gives the rise in temperature as a function of the energy density

Equations

$$\Delta x_s = c\Delta t_s \quad (1)$$

$$d_i = \frac{\lambda}{2\sin(\theta_i/2)} \quad (2)$$

$$\rho C_p \frac{\delta T}{\delta t} = q_a - q_m - q_v + \nabla\cdot(k\nabla T) \quad (3)$$

$$E = \frac{kT_m t_p 10^{-4}}{2\sqrt{\chi t_p}\,\text{ierfc}\left[\frac{z}{2\sqrt{\chi t_p}}\right]} \quad (4)$$

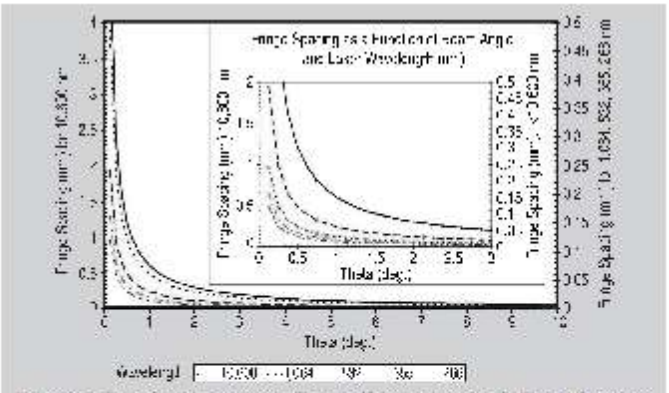

Figure 6. The theoretical fringe spacing with respect to source wavelength (λ) and interference angle (θi).

(fluence of the laser) and the material properties. The terms in this solution can be rearranged to estimate the energy required to produce a single fringe of a particular surface feature size using the expression shown in Equation 4, where E is the energy (fluence) in J/cm², k is the thermal conductivity in W/mK, T_m is the melting temperature in degrees Celsius, t_p is the pulse time in seconds, χ is the thermal diffusivity in m²/s, and z is the surface feature size that is assumed (as a rough estimate, the fringe width goes to zero) equal to the melt depth in meters. The function ierfc(x) is the inverse complimentary error function.

Equation 4 is based on the one-dimensional heat flow model and it is assumed that the material properties are constant, and the effects of convection and radiation are not considered. Using Equation 4, the values of fluence (for each feature) required to produce surface feature size (d_f) equal to interference fringe spacing for selected materials (metals, ceramics, and polymers) can be estimated. Table I reflects the values of these fluences for several lasers (different wavelengths) operated at suitable pulse durations and interference angles settings.[16–22] The predictions of fluence are based on the assumptions that treatments were conducted with only one laser pulse and the maximum temperature reached by the volume of material during interaction time with laser is the melting temperature of the material being treated. The level of the required fluence at one location can be further reduced by delivering subsequent multiple laser pulses. Furthermore, the level of fluence in the original laser beam prior to interference is related to the fluence at each interference fringe. Also, the ratio of beam diameter to fringe spacing represents the number of fringes (nodes) produced for the given angle of interference (θ_i).

To realize a surface feature of distinct characteristic both in terms of microstructure and physical nature from its surrounding volume of material, the surface feature size (d_f) should be equal to or less than the interference fringe spacing (d_i) (Figure 7). However, surface feature size larger than interference fringe size ($d_f > d_i$) is likely to produce an array of surface features with partial overlap, and therefore, no multi-scale texture will be generated, as depicted in Figure 7. Table I thus provides a tool for selection of appropriate laser processing parameters for generation of surface features on various materials. A few values of fluence missing in the table indicate that the selected combinations of laser processing parameters are not suitable for generation of required surface features due to the tremendously large fluences associated with them. It can be observed from this table that the required surface feature can be generated by selection of the appropriate combination of parameters for the same laser or by selection of another type of laser (wavelength). Thus, the resulting nature of the array of surface features is influenced not only by the angle (θ_i) between interfering beams, but also by the thermal conductivity, k of the material, for a given wavelength of laser (Equation 2, Figures 6 and 7, and

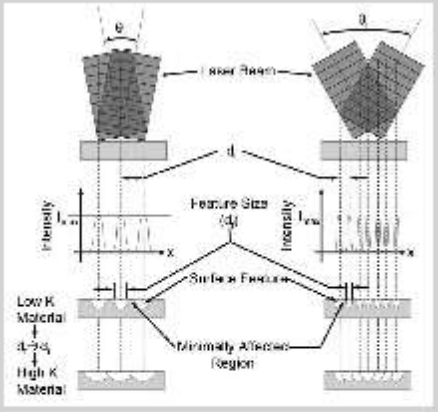

Figure 7. A schematic of the surface feature produced by the LIST technique, showing the effects of interference angle (θ) and thermal conductivity (k) of the material.

Table I).

As with all systems, there are limiting factors that determine an envelope within which the system will function. The envelope that encloses the functionality of the interferometer is defined by the beam size, thermal conductivity, as described previously, the diffraction limit, and the atomic limit. Excluding thermal conductivity effects, the beam size and the atomic limit determine the upper and lower feature size limits as the maximum feature size will not exceed the size of the beam and the minimum feature size can never be smaller than an atom. The diffraction limit, on the other hand, is related to the coherence of the source and the quality of the optics. This results in a limit to the resolution of the system.

Interferometer

The basic interferometer design, as shown schematically in Figure 5, may include a BET, which may itself include a spatial filter, a beam splitter, a set of mirrors, and focusing optics. The BET essentially sets the size of the beam through the interferometer and can thus be used to help determine the fluence at the sample. The beam splitter splits the beam (symmetrically or asymmetrically), which then progresses to the mirrors and then to the sample. The contrast between the bright and dark lines is determined by the difference of intensity between the arms of the interferometer. The difference in length of the interferometer arms determines the OPD which must be less than Δx_c.

The OPD also determines how well defined the pattern, and ultimately the surface features, are. If one arm of the interferometer is shorter than the other, the beam from the shorter arm will arrive at the sample surface first, at which time the surface modification will begin and the interaction time between the beams will decrease accordingly. The interferometer can be designed such that any interference angle can be achieved by moving the mirrors and with minor adjustments to the incidence angle. Finally, a set of focusing optics may be added to refine the fluence at the material surface.

CONCLUSION

While several techniques are available for refining surface topography to create hierarchical surface structures, laser writing and laser interference surface treatment offer the advantage, as direct application techniques, of requiring fewer steps. The writing technique has been used to process zirconia coatings on Ti-6Al-4V substrates and in the future will be expanded for use on other systems. The interferometer technique can be applied to a variety of materials; however, the material and the laser must be carefully chosen to achieve the desired results. While this article covered the construction of a two-beam interferometer, similar principals may be applied for interferometers with greater numbers of beams to develop patterns of dots or refined fringe patterns. Unlike laser direct writing, the LIST technique is suited to produce a variety of multi-scale features at substantially finer scales at rapid speeds.

ACKNOWLEDGEMENTS

The authors would like to recognize Dr. Claus Daniel of Oak Ridge National Laboratory for many helpful conversations regarding the set-up and use of interferometers.

References

1. A. Kurella and N.B. Dahotre, *J. Mat. Sci: Mat. in Med.*, in press.
2. G. Dumitru et al., *Appl. Phys. A*, 70 (4) (2000), pp. 485–487.
3. A. Blatter et al., *Wear*, 232 (2) (1999), pp. 226–230.
4. M. Wakuda et al., *Wear*, 254 (3-4) (2003), pp. 356–363.
5. U. Pattersen and S. Jacobson, *Tribo. Int.*, 36 (11) (2003), pp. 857–864.
6. J. Tan and W.M. Saltzman, *Biomaterials*, 25 (2004), pp. 3593–3601.
7. P.L. Li et al., *IEEE Trans. On Nanobioscience*, 2 (3) (2003), pp. 138–145.
8. A. Kurella and N.B. Dahotre, *J. Biomed. App.*, 20 (1) (2005), pp. 5–50.
9. C.D.W. Wilkinson et al., *Mat. Sci. & Eng. C*, 19 (2002), pp. 263–269.
10. I. Jager and P. Fratzl, *Biophys. J.*, 79 (October 2000), pp. 1737–1746.
11. M.S. Madou, *Fundamentals of Microfabrication: The Science of Miniaturization*, 2nd ed. (Boca Raton, FL: CRC Press, 2002).
12. C. Daniel and F. Mucklich, *App. Surf. Sci.*, 242 (2005), pp. 140–146.
13. C. Daniel, F. Mucklich, and Z. Liu, *App. Surf. Sci.*, 208-209 (2003), pp. 317–321.
14. F. Mucklich, A. Lasagni, and C. Daniel, *Intermetallics*, 13 (2005), pp. 437–442.
15. B.L. Anderson and L.J. Pelz, *App. Optics*, 34 (32) (1995), pp. 7443–7450.
16. W.J. Parker et al., *J. App. Phys.*, 32 (9) (1961), pp. 1679–1684.
17. E.O. Ezugwu and Z.M. Wang, *J. of Mat. Process. Tech.*, 68 (1997), pp. 262–274.
18. Y.-G. Jung, S.-C. Choi, and C.-S. Oh, *J. Mat. Sci.*, 32 (1997), pp. 3841–3850.
19. K.S. Ravichandran et al., *J. Amer. Ceram. Soc.*, 82 (3) (1999), pp. 673–682.
20. A.C. Bento et al., *J. App. Phys.*, 79 (9) (1996), pp. 6848–6852.
21. K. Elermann and K.-H. Hellwege, *J. Polymer Sci.*, 57 (1962), pp. 99–106.
22. A.A. Minakov, Y.V. Bugoslavsky, and C. Schick, *Thermochimica Acta*, 317 (1998), pp. 117–131.

P. Gregory Engleman and Narendra B. Dahotre are with the Department of Materials Science and Engineering at the University of Tennessee at Knoxville and the Materials Processing Group in the Metals and Ceramics Division at Oak Ridge National Laboratory. Anil Kurella and Anoop Samant are with the Department of Materials Science and Engineering at the University of Tennessee in Knoxville. Craig A. Blue is with the Materials Processing Group in the Metals and Ceramics Division at Oak Ridge National Laboratory.

For more information, contact N.B. Dahotre, University of Tennessee, Department of Materials Science and Engineering, Knoxville, TN 37996; (865) 974-3609; fax (865) 974-4115; e-mail ndahotre@utk.edu

Vita

Anil Kumar Kurella did his Bachelors in Metallurgical Engineering from Andhra University, India in 2002. He received the University Gold Medal for achieving top rank in the Undergraduate program. Anil later worked as a research fellow at International Advanced Research Center (ARCI) on magnesium alloy development for automotive applications. He then came to University of Tennessee, Knoxville for graduate program in Materials Science and Engineering. He received his Master Degree from the University of Tennessee in fall 2005. Anil is currently employed with Intel Corporation in Hillsboro, Oregon as a Material Scientist working in the area of failure analysis and semiconductor reliability. Anil has published 10 papers in the area of materials science and engineering in peer reviewed journals and presented at 2 international conferences. He has reviewed papers for the journal *Actabiomaterialia*. In 2006 Anil was awarded "TMS Outstanding Graduate Student Paper" for his paper titled "Phase and Morphological Evolution in Laser Textured Zirconia Coating on Ti alloy". He is an active member of ASM, TMS, SMTA and EDFAS. Anil's research interests include laser materials processing and semiconductor reliability.